Coherent atom-light interactions in multi-level systems

MARK GEORGE BASON

Coherent atom-light interactions in multi-level systems

Mark G. Bason

A thesis submitted in partial fulfilment
of the requirements for the degree of
Doctor of Philosophy

Department of Physics
Durham University

October 20, 2009

Coherent atom-light interactions in multi-level systems

Mark G. Bason

Abstract

This thesis presents work on experiments performed using electromagnetically induced transparency (EIT) in Rubidium vapour cells. Starting with a simple three-level Λ-system, extra complexity is introduced by adding an additional control beam. This makes the switching from narrow transmitting resonances to absorbing resonances possible. Rydberg EIT is then introduced and is used to shown how the switching of such resonances using external electric fields in possible. The work then progresses towards the use of thin vapour cells to overcome the limitations of conventional systems. In the transition to thin vapour cells, the role of dipole interactions in Rydberg atoms motivates the idea of an atomic quantum dot. The Kerr effect is then characterised and used to perform phase modulation in a gas. The Rydberg state itself is then phase modulated and this is shown to give rise to frequency sidebands which offer a promising way of determining dc electric fields.

Declaration

I confirm that no part of the material offered has previously been submitted by myself for a degree in this or any other University. Where material has been generated through joint work, the work of others has been indicated.

Mark Bason
Durham, October 20, 2009

Dedicated to the memory of generations of Basons and Mitchells,
especially Rosaleen and in thanks of the continued support of my father, Tom.

Acknowledgements

Praise must be given to my supervisor Charles Adams, his continued support, approach to doing science, leadership and musings on cricket have made the whole of my studies very enjoyable. Thanks must also go to the two post-doctoral researchers, Ashok Mohapatra and Kevin Weatherill who have helped guide me through the research process, hopefully some of their flair for science has rubbed off on me. Ifan Hughes must also be recognised for his clear thinking and thorough explanations. In fact the whole of AtMol deserve credit for nurturing a friendly atmosphere in which to do science, in particular the football skills of Antoine Gusdorf and Steven Wrathmall, computing prowess of Tom Billam, Mark Saunders, Paul Halkyard and Mr Matlab: Jon Pritchard and 'wit' of al the Strontium boys James Millen, Graham Lochead and Matt Jones. To my German friends and associates, Björn Butscher and Ulrich Raitzsch I say thanks for the help and your good humour.
To all my old housemates and friends in Durham, you have made the last 3 years memorable and fun, I couldn't have done it without your support. Neither could I have survived without the presence and love of my family.

Contents

List of Figures

Chapter 1

Introduction

'Coherent atom-light interactions' is a very broad term for a wide range of physics. As a subset of atomic physics, coherent processes constitute a large body of work, and any summary of this field would need to be sizeable. The observation that light can be coherent is a familiar concept in physics; atomic coherences are less widely appreciated. Understanding atomic coherences depends on recognising that quantum mechanics involves not just population, but probability amplitudes. The products of these probability amplitudes gives rise to either the probability of an atom being in a certain state, or an atomic coherence. These atomic coherences reply upon a spectrally pure, coherent driving field to create them; thus the use of lasers is necessary when working in the optical region.

To indicate just how prevalent the effects of atomic coherence can be, one just has to look at the different experiments in which they have been exploited. For example, coherent population trapping (CPT) [1] makes use of laser-induced coherences to generate a 'dark state,' formed from the superposition of two atomic states. After being pumped into this dark state, the atoms cannot be excited by either laser field, the population is said to be 'trapped.' This technique has been used to circumvent both the Doppler limit and single photon recoil limit in laser cooling using ^{4}He [2] and many other atoms, and also in precision spectroscopy to generate very narrow features, less than 50 Hz wide [3].

Stimulated Raman adiabatic passage (STIRAP) [4, 5], involves using a counter-intuitive sequence of beam pulses to transfer population between different states. The process relies upon coupling three states: initial, intermediate and final, using

two laser fields. Crucially, the population is never transferred to the intermediate state. This 'bypasses' the problem of spontaneous decay. Using this technique, experiments have successfully allowed the transfer of molecules to their ro-vibrational ground states [6], an important step towards achieving a molecular Bose-Einstein condensate. Lasing without inversion (LWI) relies upon suppressing absorption of photons so that it is possible to produce gain, even when there is limited population in the excited state [7, 8]. Interest in this field is motivated by the possibility of creating sources of short-wavelength light such as x-rays.

The term electromagnetically induced absorption (EIA) refers to the enhanced absorption of light around resonance [9, 10]. This technique has been used to manipulate the group velocity of light: making it negative and producing superluminal light pulses [11, 12]. Superluminal light propagation is measured by comparing the arrival time of pulses of light which have passed through either the vacuum or a specially prepared medium. In the superluminal case, the peak of the vacuum-pulse arrives after that the pulse from the modified medium. This effect results from classical interference and does not violate special relativity [13]. Large group indices are also possible using a process known as electromagnetically induced transparency (EIT), giving rise to slow-light [14]. This is just one of the motivating reasons for studying EIT and in fact this work concentrates almost exclusively on applying the phenomenon in different ways.

1.1 Electromagnetically induced transparency

EIT is a technique for making what would otherwise be an optically thick medium transparent [15]. This change in transmission arises through the coupling together of three atomic levels using two laser fields. Three classic examples for the configuration of energy levels are Λ, V and Ladder/Cascade [16]. Before presenting the physical origins of EIT, which follow in chapter 2, a few of the notable uses of the effect are discussed.

1.1.1 Slowing and storage of light

The ability to manipulate the group velocity, v_g, has been demonstrated by researchers using different systems. Experiments on self-induced transparency [17] and off-resonant optical systems using Doppler-broadened absorption resonances [18] have been used to slow light by up to a factor of 1000.

The observation of extremely small group velocities was first seen by Hau *et al.* in a Bose Einstein condensate of sodium atoms [14]. In this work a group velocity of $v_g = 17$ ms^{-1} was achieved. It is also possible to observe drastic slowing of light in room temperature rubidium vapour, down to velocities as low as 8 ms^{-1} [19].

The stopping of light was first seen in a cloud of sodium atoms [20]; this work was also carried out by the group of Hau. In this experiment it was possible to compress the laser pulse and store it in the medium for around 1 ms. Yet again, the same stopping of light has been shown to be possible in rubidium vapour [21] heated to around 90 °C to increase the number density. Recent developments in this field have shown storage times of 240 ms [22] using a Mott insulator state.

1.1.2 Precision measurements

The ability to perform precision measurements using this technique makes EIT interesting to the metrology community. Increased sensitivity of Sagnac interferometry using slow light has been shown [23]. Such an improvement benefits from the transfer of momentum from the light to the atoms, causing the creation of coherent matter waves which enhance the rotation signal.

Improvements in optical interferometry have also had an impact in magnetometry [24]. Optical-interferometric magnetometers with detection limits of around 4 pT/$\sqrt{\text{Hz}}$ have been developed; these devices are competitive with leading technology based on superconducting quantum interference.

1.2 Rydberg states

Throughout the course of this work, it will become apparent that by incorporating Rydberg states into an EIT system one has added control over light propagation.

Rydberg states are atomic states with a high principal quantum number, n, as expressed in the Rydberg formula, which relates the wavelength of emitted light, λ, corresponding to the transition between an initial state, i, and final state, j,

$$\frac{1}{\lambda} = R\left(\frac{1}{n_i} - \frac{1}{n_j}\right), \tag{1.1}$$

where R is the Rydberg constant. Various scaling relations characterise Rydberg atoms, for example, the classical radius of an electron's orbit increases as n^2 and the binding energy scales as n^{-2}. Thus electrons in Rydberg states have large, loosely bound orbits. More of these scaling relations are summarised in chapter 4.

Much of the interest in Rydberg atoms stems from the fact that they have a very large polarisability, i.e., exaggerated responses to electric fields. This is tied into the fact that the separation between atoms decreases as n increases. This also means that Rydberg atoms can possess large dipole moments. The interaction of these dipole moments, and in particular the associated shifts in energy, have given rise to a new generation of experiments aimed at demonstrating and exploiting this effect.

1.2.1 Collective effects

Historically the study of Rydberg atoms has benefited from the development of the laser, prior to this invention the excitation of atoms to a well-defined Rydberg state was difficult [25]. With the increasing availability of laser light sources, experiments were able to resolve fine structure using Doppler free spectoscopy [26]. Further developments led to the detection of van der Waals interactions in a dense Rydberg gas [27]. This experiment hinted at one way that Rydberg physics was to progress: studying collective effects.

As Rydberg atoms give rise to strong interactions, two different effects arise. The first, dipole blockade, means that within a certain length scale, the 'blockade radius', only one atom is allowed to be promoted to the Rydberg state. This then gives rise to collective effects, such as the increase in Rabi frequency of atoms flopping between the ground and Rydberg state [28]. Such an experiment is dependent on the availability of cold atoms; indeed many investigations into interactions have exploited the high density and low temperature of such sources [29–33].

1.2.2 Quantum information

Rydberg atoms are potential candidates for quantum computing, benefiting from the use of dipolar interactions as a basis for a quantum gate [34]. Due to the strength of these interactions the entanglement between two atoms would be fast, with gate times in the microsecond range [35]. Theoretical work has also been extended to manipulating quantum information in collective states [36].

The potential for arranging large arrays of single atoms trapped in a three-dimensional optical lattice [37] may pave the way for many particle entanglement. This would fulfil one of Divincenzo's criteria for the scalability of a quantum computer [38]. Recently the demonstration of dipole blockade using single atoms trapped in far off resonance dipole traps has been demonstrated [39, 40]. These experiments are an important milestone towards a two-atom quantum gate.

This interest in quantum information is not limited to entangling atoms. Photons also make good qubits, and techniques for entangling photons [41] have been developed in the last decade. To this end, EIT was once thought of as a candidate for photon entanglement, with the effect used to perform a phase gate. However EIT has insufficient non-linearity to achieve such a goal [42]. Even using the ac Kerr effect [43] has problems with pulse distortion [44].

Interactions of slow light pulses due to long-range dipole-dipole interactions benefit from the fact that since the interaction is not short range, the two photons do not have to interact with the same atom [45]. Thus the effect of interactions on pulse propagation is well worth pursuing. Using so-called 'dark-state' polaritons [46], superpositions of light and matter, there would also be a way of storing such qubits [47].

1.3 Rydberg EIT

EIT systems under a ladder or cascade setup have previously only extended up to relatively low lying n states, the highest being $n = 8$ in the group of van Wijngaarden [48]. With much interest in the slowing and storing of light, the extension to include higher states in the ladder had not been undertaken; it is more difficult to generate narrow EIT features in the cascade system than the Λ-system. With the

growth in interest in Rydberg atoms, especially with respect to their potential in quantum information systems, the need for a non-destructive means of detection became apparent. In many experiments detection is performed by field ionising the Rydberg atom and detecting the charged ions and electrons [49]. The advent of Rydberg EIT [50] offered a solution to this problem; it was no longer necessary to ionise the Rydberg atom, an all optical process was possible. Soon after this demonstration came another experiment in much the same manner, this time in a Strontium atomic beam, [51].

The number of experiments involving Rydberg EIT has grown significantly in the last two years. Three such experiments form the backbone of this thesis [52–54]. In these investigations Rydberg EIT has been used to control atom-light interactions through the use of an external electric field [53]. This sensitivity to electric fields has also been exploited to control the phase of a probe beam, and to measure the Kerr coefficient of a thermal ensemble of Rubidium atoms [52]. Phase modulation has also been extended to the Rydberg state itself, dressing the state and producing frequency sidebands, with possible implications in determining electric fields [54].

Cold Rydberg studies have also benefited from the ability to lock the 480 nm laser used in many experiments to excite atoms to the Rydberg state [55]. Using an electro-optic modulator (EOM) to modulate a probe beam and counter-propagating the 480 nm coupling light produces a Pound-Drever-Hall type signal, well suited to frequency stabilising the Rydberg laser. Using such a method, Rydberg EIT has been used as a probe for cold atoms, producing sub-MHz resonances [56]. Other experiments in cold atoms using Rydberg EIT have shown that the dominant mechanism for dephasing is due to interactions [57].

Recent work on the spectroscopy of Rydberg atoms has developed alternative routes to achieve and detect excitation to the Rydberg state [58, 59]. Although the scheme described in these papers is not EIT, but more of a shelving technique, it could easily be generalised and indeed this is part of the future work presented in chapter 5.

Perhaps most excitingly, such experimental advances have started to stimulate theoretical work into using Rydberg EIT in quantum information. The proposal by Müller and co-workers has focussed on the using Rydberg EIT in a mesoscopic

quantum gate [60]. The scheme combines the Λ-system and the Rydberg state into an inverted Y-system. Transfer of atoms between the two ground states of the Λ-system being conditional upon the presence of an atom in the Rydberg state.

1.4 Thesis Layout

This thesis explores various ways in which mechanisms for extra control over light propagation can be implemented using EIT. A range of experiments will demonstrate that expanding the three-level system to include extra states or including Rydberg states are two ways to control the absorption and dispersion of light.

The structure of this thesis is as follows:

- Chapter 2 begins by presenting EIT as a solution of the optical Bloch equations in a three-level system and uses the Λ-system to demonstrate experimentally this phenomenon.
- Chapter 3 extends the three-level formalism by including an additional level in an attempt to gain control over the system's coherences.
- Chapter 4 combines the properties of Rydberg atoms and EIT to show how the manipulation of electric fields has implications for the generation of atomic coherences.
- Chapter 5 aims to address the technical drawbacks of Rydberg EIT by using thin vapour cells.
- Chapter 6 explores the phase response of Rydberg EIT under application of an electric field. The measure of this response, the dc Kerr coefficient, is characterised for the thermal vapour.
- Chapter 7 uses the change in absorption associated with EIT to extract information about the electric field across a sample, a step towards using Rydberg EIT for electrometry.
- Chapter 8 concludes the thesis and looks towards possible future directions

1.5 Publications arising from this work

Narrow absorptive resonances in a four-level atomic system
M. G. Bason, A. K. Mohapatra, K. J. Weatherill and C. S. Adams
J. Phys. B **42**, 075503 (2009)

Electro-optic control of atom-light interactions using Rydberg dark-state polaritons
M. G. Bason, A. K. Mohapatra, K. J. Weatherill and C. S. Adams
Phys. Rev. A **77**, 032305 (2008)

A giant electro-optic effect using polarizable dark states
A. K. Mohapatra, M. G. Bason, B. Butscher, K. J. Weatherill and C. S. Adams
Nat. Physics **4**, 890 (2008)

Enhanced electric field sensitivity of rf-dressed Rydberg dark states
M. G. Bason, M. Tanasittokosol, A. Sargsyan, A. K. Mohapatra, D. Sarkisyan, R. M. Potvliege and C. S. Adams
arXiv:0906.4367v1

1.6 Related publications

Laser frequency stabilization to highly excited state transitions using electromagnetically induced transparency in a cascade system
R. P. Abel, A. K. Mohapatra, M. G. Bason, J. D. Pritchard, K. J. Weatherill, U. Raitzsch and C. S. Adams
Appl. Phys. Lett. **94**, 071107 (2009)

Electromagnetically induced transparency of an interacting cold Rydberg ensemble
K. J. Weatherill, J. D. Pritchard, R. P. Abel, M. G. Bason, A. K. Mohapatra, and C. S. Adams

J. Phys. B **41**, 201002 (2008)

Chapter 2

Electromagnetically Induced Transparency (EIT) Lambda system

The interaction between light and matter in a two-level system is the basis for describing many aspects of atomic physics, such as Rabi oscillations, atomic clocks and the radiation force used in laser cooling. Since the 1990s however, the quantum optics community have sought to develop their understanding of more complex dynamics in systems with more than two levels. For example, it was realised that three-level systems can display novel features not possible in the two-level system. One interesting example is electromagnetically induced transparency (EIT) [42]. This acronym attempts to describe the reduction in absorption of a probe laser field through an absorptive medium due to the presence of a second, 'coupling' field: one that couples to a third state. The absorptive resonances usually associated with a two-level system can be made partially transparent over some frequency width. As shown through the Kramers-Kronig relations, any change in the absorption of a medium also modifies the dispersion [61]. As the EIT features in transmission are narrower in frequency than that of the two level case, higher dispersion occurs.

This control of a medium's optical response is due to the ability to induce coherence using laser fields. More specifically, the evolution of the atom-light system depends upon the phase of the atomic-state amplitudes and not just on the population dynamics of the atomic levels.

The first experimental observation of EIT was made in 1990 by Harris [62] in a Strontium vapour. For that experiment the beams coupled to form a Λ-system,

so called because the shape made by the beams resembles the Greek letter, as in figure 2.1. There are two other configurations of states usually used for studying EIT, cascade (or ladder) and V. In the description that follows only the Λ-system will be presented, however the other two systems are easily described by appropriate changes in energies and couplings; the cascade system will be discussed in chapter 4. Common to all these configurations is that there is no coupling between two of the constituent states, $|1\rangle$ and $|3\rangle$ in figure 2.1.

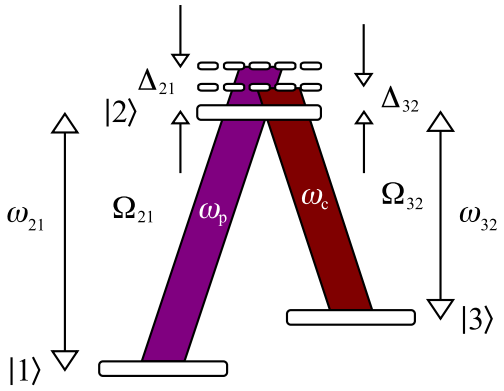

Figure 2.1: A three level atom, with frequency spacings ω_{21} and ω_{32}, interacts with a probe field ω_p and coupling field ω_c in a Λ configuration. The probe and coupling fields have associated Rabi frequencies Ω_{21} and Ω_{32} respectively.

2.1 Three level atom

The interaction between a three-level system and two light fields as shown in figure 2.1 is given by

$$\mathcal{H} = \mathcal{H}_a + \mathcal{H}_i \,, \tag{2.1}$$

where the total hamiltonian $\mathcal{H}$ is given by the sum of the atomic energy, $\mathcal{H}_a$ and the light field interaction $\mathcal{H}_i$. In the following approach, using the semi-classical treatment, the quantisation of the light field is ignored, instead the light is considered as a electric field, $\mathcal{E}$, which interacts with a dipole $\mathbf{d}$ to give

$$\mathcal{H}_i \;=\; -\mathbf{d}\cdot\mathcal{E}\,, \tag{2.2}$$

$$\tag{2.3}$$

where $\mathbf{r}$ is the vector of operators that project an initial to a final state and $\mathbf{d} = \mathrm{e}\mathbf{r}$. This approximation is valid when the wavelength of the light is much longer than the Bohr radius, thus the electric field variation can be neglected and is known as the dipole approximation. The electric field is now taken to be polarised so that is lies parallel to the vector $\hat{\mathrm{e}}$, varying with an angular frequency ω and magnitude $\mathcal{E}_0$.

$$\mathcal{E}(t) = \mathcal{E}_0 \hat{\mathrm{e}} \cos(\omega t) \,, \tag{2.4}$$

For the system under consideration, equation 2.3 yields

$$\mathcal{H}_\mathrm{a} = \hbar\omega_{21} |2\rangle\langle 2| + \hbar\omega_{32} |3\rangle\langle 3| \tag{2.5}$$

$$\mathcal{H}_\mathrm{i} = \frac{\hbar}{2}\left(\Omega_{21}\mathrm{e}^{i\omega_\mathrm{p}\mathrm{t}} |2\rangle\langle 1| + \Omega_{32}\mathrm{e}^{i\omega_\mathrm{c}\mathrm{t}} |3\rangle\langle 2| + \mathrm{h.c.}\right) . \tag{2.6}$$

Where Ω_{ij} is the Rabi frequency defined as,

$$\hbar\Omega_{ij} = -\mathrm{e}\mathcal{E}_0 \langle i| \mathbf{r} |j\rangle \,, \tag{2.7}$$

$\hbar\omega_{ij}$ is the energy separation between different atomic states and ω_p and ω_c are the frequencies of the probe field and coupling field respectively.

This pure-state approach is useful in many circumstances, however a more general procedure is necessary when two or more pure states combine to give a 'mixed' system. This is dealt with using the density matrix formalism, which considers the system as a statistical mixture of pure states. A mixed state can't be represented as just a ket vector, $|\psi_\mathrm{i}\rangle$, and as such, the density matrix ρ is defined:

$$\rho = \sum_i p_i |\psi_\mathrm{i}\rangle\langle\psi_\mathrm{i}| \,, \tag{2.8}$$

where p_i is the probability of being in the pure state ψ_i. In the case of the three level atom, this state is just

$$|\psi_\mathrm{i}\rangle = c_1 |1\rangle + c_2 |2\rangle + c_3 |3\rangle \,. \tag{2.9}$$

This results in,

$$\rho = \begin{pmatrix} |c_1|^2 & c_1 c_2^* & c_1 c_3^* \\ c_2 c_1^* & |c_2|^2 & c_2 c_3^* \\ c_3 c_1^* & c_3 c_2^* & |c_3|^2 \end{pmatrix} . \tag{2.10}$$

One can derive a density matrix equivalent of the Schrödinger equation, known as the quantum Liouville equation or Von Neumann equation, see appendix A,

$$\dot{\rho} = \frac{-\mathrm{i}}{\hbar}[\mathcal{H}, \rho] \,. \tag{2.11}$$

This governs the evolution of the density matrix. However loss out of this system has not been accounted for, namely decay due to spontaneous emission. This is included by adding a decay term, $\mathcal{D}$

$$\mathcal{D} = \sum_d \frac{\Gamma_d}{2}\left(\sigma_d\dagger\sigma_d\rho + \rho\sigma_d\dagger\sigma_d - 2\sigma_d\rho\sigma_d^\dagger\right) , \tag{2.12}$$

where $\sigma_d\dagger = |n\rangle\langle m|$ and Γ_d is the decay rate from state $n, m \in \{|1\rangle, |2\rangle, |3\rangle\}$. Thus a more complete description of the system is,.

$$\dot{\rho} = \frac{-\mathrm{i}}{\hbar}[\mathcal{H}, \rho] - \mathcal{D} , \tag{2.13}$$

so called the Linblad master equation.

2.2 Optical-Bloch equations

The optical-Bloch equations are used to calculate the evolution of both the populations and coherences in multi-level systems. They are analogous to the Bloch equations used in nuclear magnetic resonance [63]. Extracting the diagonal elements ρ_{ii} terms from the density matrix, provides information about the population of state i. However of greater interest to this work are the coherence terms, ρ_{ij}, the off-diagonal elements of the density matrix and associated with the change in transmission and phase. Before arriving at these equations, a transformation into a frame that rotates with the laser frequencies is made:

$$\begin{aligned}
\sigma_{11} &= \rho_{11} & \sigma_{12} &= \rho_{12}\mathrm{e}^{-\mathrm{i}\omega_p t} \\
\sigma_{22} &= \rho_{22} & \sigma_{21} &= \rho_{21}\mathrm{e}^{\mathrm{i}\omega_p t} \\
\sigma_{33} &= \rho_{33} & \sigma_{31} &= \rho_{31}\mathrm{e}^{\mathrm{i}(\omega_p-\omega_c)t} \\
& & \sigma_{13} &= \rho_{13}\mathrm{e}^{-\mathrm{i}(\omega_p-\omega_c)t} .
\end{aligned} \tag{2.14}$$

Using equation 2.13 and solving for these coherences under the new transformation gives,

$$\dot{\sigma}_{21} = -(\gamma_{21} - \mathrm{i}\Delta_{21})\sigma_{21} + \frac{\mathrm{i}\Omega_{32}}{2}(\sigma_{22} - \sigma_{11}) + \frac{\mathrm{i}\Omega_{21}}{2}\sigma_{31} \tag{2.15}$$

$$\dot{\sigma}_{31} = -(\gamma_{31} - \mathrm{i}(\Delta_{32} + \Delta_{21}))\sigma_{31} - \frac{\mathrm{i}\Omega_{32}}{2}\sigma_{21} + \frac{\mathrm{i}\Omega_{21}}{2}\sigma_{32} \tag{2.16}$$

$$\dot{\sigma}_{32} = -(\gamma_{32} - \mathrm{i}\Delta_{32})\sigma_{32} + \frac{\mathrm{i}\Omega_{32}}{2}(\sigma_{33} - \sigma_{22}) - \frac{\mathrm{i}\Omega_{21}}{2}\sigma_{31} , \tag{2.17}$$

where $\Delta_{21} = \omega_p - \omega_{21}$ and $\Delta_{32} = \omega_c - \omega_{32}$. Of these solutions, σ_{21}, is the most useful as it permits the calculation of the absorption and dispersion coefficients for the probe field. Following the approach of Gea-Banacloche *et al.* [64], σ_{31} is solved for in the steady state by setting $\dot{\sigma}_{31} = 0$. Thus,

$$\sigma_{31} = -\frac{\mathrm{i}\Omega_{32}}{2(\gamma_{31} - \mathrm{i}(\Delta_{21} + \Delta_{32}))}\sigma_{21} + \frac{\mathrm{i}\Omega_{21}}{2(\gamma_{31} - \mathrm{i}(\Delta_{21} - \Delta_{32})}\sigma_{32} \,. \tag{2.18}$$

Since the probe field power is expected to be weak, as is the case in EIT, and the populations in states $|2\rangle$ and $|3\rangle$ will be but a small percentage of the total, thus σ_{32} and Ω_{21} will be small and the second term can be neglected. As such,

$$\sigma_{31} \simeq -\frac{\mathrm{i}\Omega_{32}}{2(\gamma_{31} - \mathrm{i}(\Delta_{21} - \Delta_{32}))} \,. \tag{2.19}$$

Now combining equations 2.15 and 2.18,

$$\sigma_{21} = \frac{\Omega_{21}/2(\sigma_{22} - \sigma_{11})}{\gamma_{21} - \mathrm{i}\Delta_{21} + \dfrac{\Omega_{32}^2}{4(\gamma_{31} - \mathrm{i}(\Delta_{32} - \Delta_{32}))}} \tag{2.20}$$

$$\sigma_{21} \simeq -\frac{\Omega_{21}/2}{\gamma_{21} - \mathrm{i}\Delta_{21} + \dfrac{\Omega_{32}^2}{4(\gamma_{31} - \mathrm{i}(\Delta_{32} - \Delta_{32}))}} \,, \tag{2.21}$$

where, again the population of state $|2\rangle$ is assumed to be small; the vast majority of the population remains in the ground state, $|1\rangle$.

2.3 Absorption and Dispersion

To extract a macroscopic observable which relates to a solution of the optical-Bloch equations 2.21, a comparison is made between the polarisation, $\mathcal{P}$ and electric susceptibility χ. Maxwell defined the displacement vector.

$$\mathcal{D} = \epsilon_0 \mathcal{E} + \mathcal{P} \,, \tag{2.22}$$

where ϵ_0 is the permittivity of free space. For an isotropic, linear medium, of permittivity ϵ, $\mathcal{D} = \epsilon\mathcal{E}$, thus

$$\mathcal{P} = (\epsilon - \epsilon_0)\mathcal{E} \tag{2.23}$$

$$= \epsilon_0 \chi \mathcal{E} \tag{2.24}$$

$$= \frac{\epsilon_0 \mathcal{E}_0}{2}[\chi(\omega_p)\mathrm{e}^{-\mathrm{i}\omega_p t} + \chi(\omega_p)\mathrm{e}^{\mathrm{i}\omega_p t}] \,, \tag{2.25}$$

where

$$\chi = \frac{\epsilon}{\epsilon_0} - 1 \, . \tag{2.26}$$

A useful feature of the density matrix approach is the ability to find the expectation value of an operator, $\langle \hat{A} \rangle$, using:

$$\langle \hat{A} \rangle = \mathrm{Tr}(\rho \hat{A}) \, . \tag{2.27}$$

To find the polarisation of an atomic ensemble, with number density N, it is necessary to realise that physically this is the net dipole moment per unit volume, i.e. the polarisation can be written as

$$\begin{aligned} \mathcal{P} &= N\langle \hat{d} \rangle & (2.28) \\ &= N\mathbf{d_{21}}(\sigma_{21} e^{i\omega_p t} + \sigma_{12} e^{-i\omega_p t}) \, . & (2.29) \end{aligned}$$

The $\mathbf{d_{32}}$ terms do not contribute to the polarisation due to the coupling field oscillating at a different frequency. Comparing this equation with 2.25, χ can be expressed as

$$\chi = -\frac{2N|\mathbf{d_{21}}|^2 \sigma_{21}}{\hbar \epsilon_0 \Omega_{21}} \, . \tag{2.30}$$

As χ is complex it can be written as $\chi = \chi_R + i\chi_I$. The absorption coefficient α, is then calculated using the imaginary part of the susceptibility, χ_I and dispersion coefficient, β is found via the real part of the susceptibility χ_R,

$$\begin{aligned} \alpha &= \chi_I \mathrm{k} & (2.31) \\ \beta &= \frac{\chi_R \mathrm{k}}{2} \, , & (2.32) \end{aligned}$$

where k is the magnitude of the probe beam wavevector. Using equation 2.18, both of these coefficients are plotted in figure 2.2.

2.4 Doppler Effect

So far the Doppler effect has been neglected. The light frequency 'seen' by a moving atom will differ from the frequency of the laser beam. With thermal ensembles, this results in a line-broadening as the atoms have a Maxwellian velocity distribution. For an atom moving along the z direction with velocity v_z, the shift is given by

$$\omega' \simeq \omega \left(1 + \frac{v_z}{c} \right) \, . \tag{2.33}$$

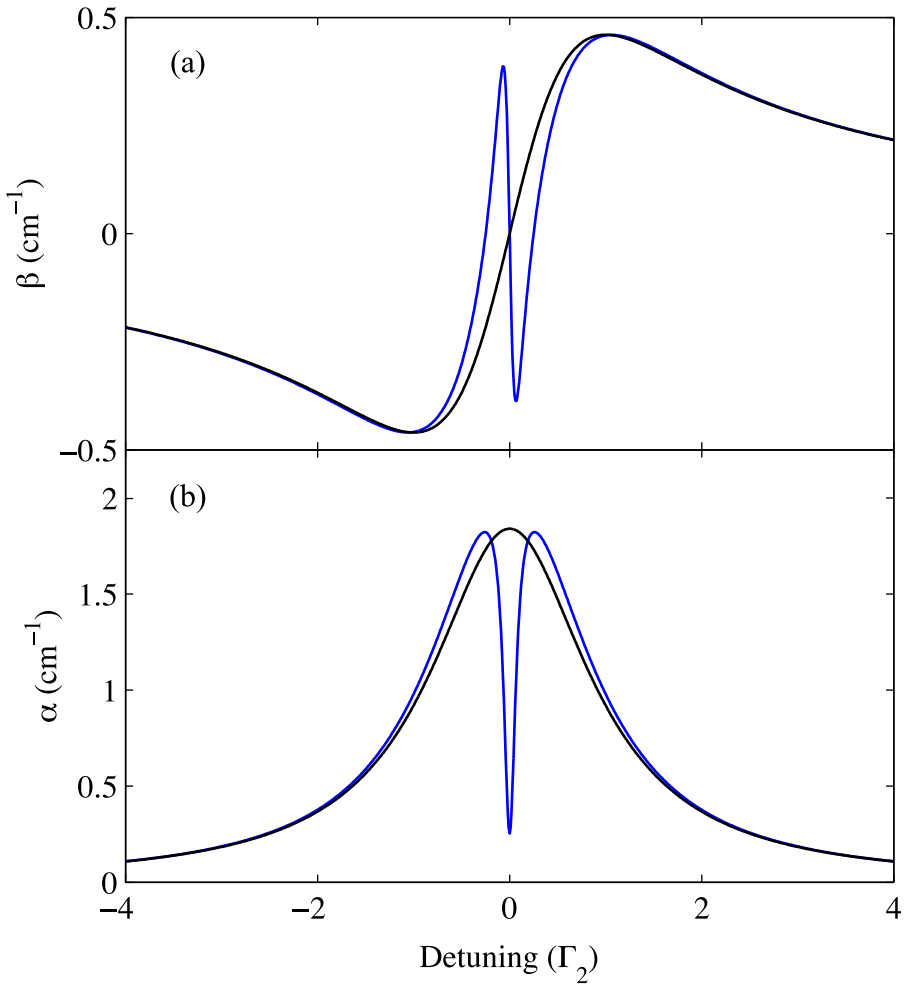

Figure 2.2: Absorption (a) and dispersion coefficients (b) as a function of probe field detuning in the presence of, no coupling field (black), and an on-resonance ($\Delta_c = 0$) coupling field of strength, $\Omega_{32} = \Gamma_2/2$, where Γ_2 is the natural decay rate of state $|2\rangle$ (blue). The decay term, $\gamma_{31} = \Gamma_2/100$, number density, $N = 2 \times 10^9$ cm^{-3} and $\mathbf{d_{21}}$=2 ea_0. Calculated using equations 2.21 and 2.30.

Thus the shift in frequency is,

$$\Delta_{\text{Doppler}} = k_z \upsilon_z \ . \tag{2.34}$$

As EIT requires two laser beams, the question of beam propagation direction becomes an issue. Ideally the beam geometry should be set so that the Doppler shifts for the probe and coupling beams cancel. With the Λ-configuration under consideration this is achieved by using co-propagating beams as shown in figure 2.3, as all velocity classes in the ensemble contribute to the EIT feature. Only for cold atoms is this not a problem as the shift is much less than the intermediate state decay rate, Γ_2.

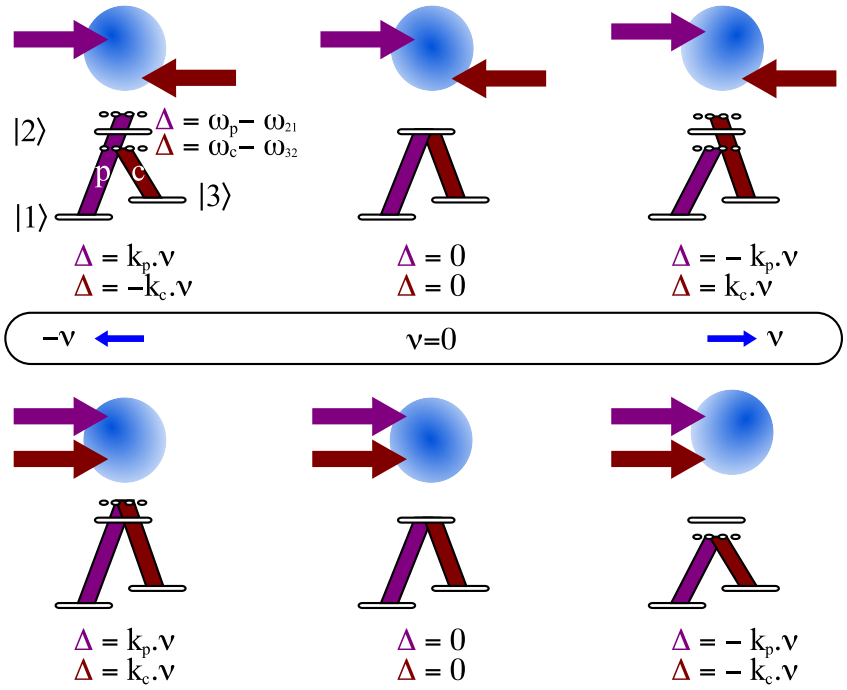

Figure 2.3: A counter-propagating beam configuration results in a mismatch of beam detunings relative to each other. Co-propagating beams however benefit from the cancellation of the Doppler shift, so all velocity classes contribute to the EIT process.

2.4.1 Transit-Time Broadening

Another consequence of using thermal atoms is that there is a limited interaction time as the atoms move through the laser beam. If the beam width is d_{beam}, and the velocity of atoms transverse to the beam is $\upsilon_\perp$ then this time is just $\tau = d_{\text{beam}}/\upsilon_\perp$. For a monochromatic laser beam of frequency ω_p and an oscillating electric field of duration τ, the frequency distribution associated with this electric field is sought by taking the Fourier transform.

$$\begin{aligned} F(\omega) &= \int_{-\infty}^{\infty} \mathcal{E}_0 \cos(\omega_p) \mathrm{e}^{-\mathrm{i}\omega t} \mathrm{d}t \\ &= \frac{\mathcal{E}_0}{2} \int_{-\tau/2}^{\tau/2} (\mathrm{e}^{\mathrm{i}\omega_p t} + \mathrm{e}^{-\mathrm{i}\omega_p t}) \mathrm{e}^{-\mathrm{i}\omega t} \mathrm{d}t \\ &\approx \mathcal{E}_0 \frac{\sin((\omega_p - \omega)\tau/2)}{(\omega_p - \omega)} \,. \end{aligned} \tag{2.35}$$

Which gives the normalised lineshape function [65],

$$g(\omega - \omega_p) = \frac{2}{\pi\tau} \frac{\sin^2((\omega - \omega_p)\tau/2)}{(\omega - \omega_p)^2} \,. \tag{2.36}$$

For a laser beam of width 2 mm and atoms moving at 200 ms^{-1}, τ is 1×10^{-5} s. The FWHM = $\Delta\nu_{1/2} = 0.886/\tau$ which gives a $\Delta\nu_{1/2}$ of $\sim$ 90 kHz. This provides a rough estimate for the expected width of the Λ-EIT feature.

2.5 Demonstration of Λ EIT

To observe the narrow resonance features expected in the EIT Λ-system, it is necessary to make phase coherent laser beams separated in frequency by the ground state hyperfine splitting [66]. For these investigations ^{87}Rb was used, the energy levels of which are shown in figure 2.4. The hyperfine ground state splitting, i.e. the frequency separation between states F = 1 and F = 2 in the ^{87}Rb isotope is $\sim$6.8 GHz. These two states are often suggested as possible qubits for quantum computation because transitions between them are electric dipole forbidden, hence they are long lived. Qubit rotations can then be realised using stimulated Raman transitions; for this reason the laser beams used are referred to as Raman beams. Such states are also a judicious choice for performing EIT due to this selection rule, providing the states $|1\rangle$ and $|3\rangle$ in the Λ-system.

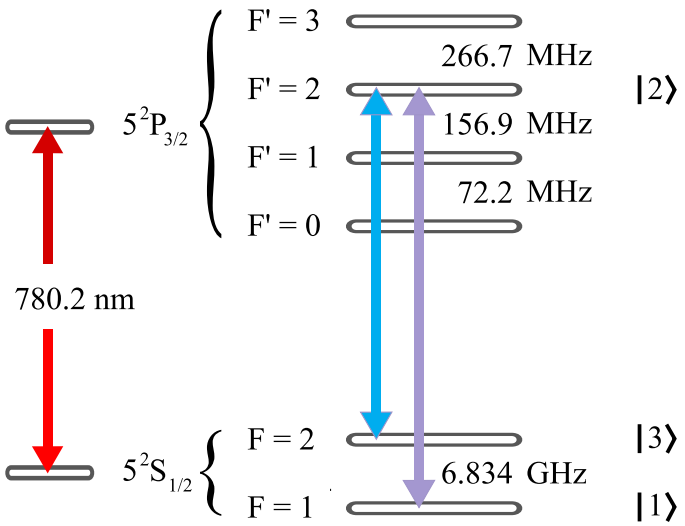

Figure 2.4: ^{87}Rb D_2 transition hyperfine structure, frequency splittings taken from reference [67]. The kets indicate the corresponding states in the Λ system.

2.5.1 Generation of Raman beams

Several different approaches have previously been adopted to achieve the generation of Raman beams. For instance, the injection locking of two diode lasers using the ± 1 diffraction orders from a high frequency acousto-optic modulator (AOM) [68], or injection locking of two diode lasers to the sidebands produced by current modulation of the master laser [69]. Another approach is to use electro-optic modulation to produce sidebands at the required frequency before injection locking a slave laser. A drawback to this approach is that typically the spectral purity of the emerging beam is poor and requires filtering of the carrier frequency using a stabilised cavity [70].

The required frequencies in this work are produced using electro-optic modulation followed by a double-injection locking technique [71]. Electro-optic crystals produce a phase retardation that is directly proportional to the applied voltage, by virtue of the linear electro-optic or Pockels effect. This is where the applied voltage, V, changes the refractive index of the crystal. The effect of such an external electric field is described in equation (2.37)

$$\Delta n_r(t) = \frac{1}{2} n_0^3 r_{33} \frac{V(t)}{d} \quad , \tag{2.37}$$

where $\Delta n_r(t)$ is the change in refractive index, n_0 is the unperturbed refraction index, r_{33} is the component of the electro-optic tensor in the direction of the applied field and d is the crystal thickness. This gives rise to a phase retardation ϕ, at a wavelength λ:

$$\phi(t) = \frac{2\pi L}{\lambda}\Delta n_r = \frac{2\pi L n_0^3 r_{33}\mathcal{E}(t)}{\lambda} \ . \tag{2.38}$$

Here L is the crystal length and $\mathcal{E}(t)$ is the electric field. Commonly crystals are characterised by a voltage V_π a 'half-wave' voltage at which a π phase shift is produced:

$$V_\pi = \frac{\lambda}{2n_0^3 r_{33}} \ . \tag{2.39}$$

The application of a such a time dependent voltage results in phase modulation as described in appendix C.

A schematic of the experimental setup is shown in figure 2.5. A commercial 780.24 nm extended cavity diode laser is stabilised to the 5s $^2S_{1/2}(F = 2) \rightarrow$ 5p $^2P_{3/2}(F' = 2)$ transition in ^{87}Rb ($|2\rangle \rightarrow |3\rangle$ in figure 2.4) using polarisation spectroscopy [72]. A part of this light is separated using a beamsplitter and is used as the coupling beam.

The remainder of the light propagates through an electro-optic modulator (EOM) (New Focus 4851). The light frequency spectrum at this point is composed of the carrier frequency and two sidebands at ±6.8 GHz. Each sideband has a relative intensity of 2% of the carrier beam. Around 200 μW of this light is then used to seed a free running diode laser which locks to the lower sideband [73, 74]. This laser consists of a collimated laser diode (Sharp GH0781JA2C) with temperature regulation via Peltier devices. The injection is obtained using a combination of current and temperature tuning, resulting in a purity of around -20 dB. To achieve a more robust lock and higher spectral purity a second slave laser is injected with the output of the first. The spectral output of this third laser, shown in figure 2.6 has carrier suppression to the level of at least -40 dB. This light is then resonant with the 5s $^2S_{1/2}(F = 1) \rightarrow$ 5p $^2P_{3/2}(F' = 2)$ transition ($|1\rangle \rightarrow |2\rangle$ in figure 2.4) and is used as the probe beam. The probe and coupling beams are combined on a polarisation beam splitting cube and coupled into a polarisation maintaining single mode fiber. The advantage of fibre coupling is that the angle between the probe and coupling fields is minimised. The closer this is to zero, the more effective the cancellation of the Doppler shifts becomes. The output of the fiber is collimated and propagates through a magnetically shielded, Rb cell of length, l = 75 mm as

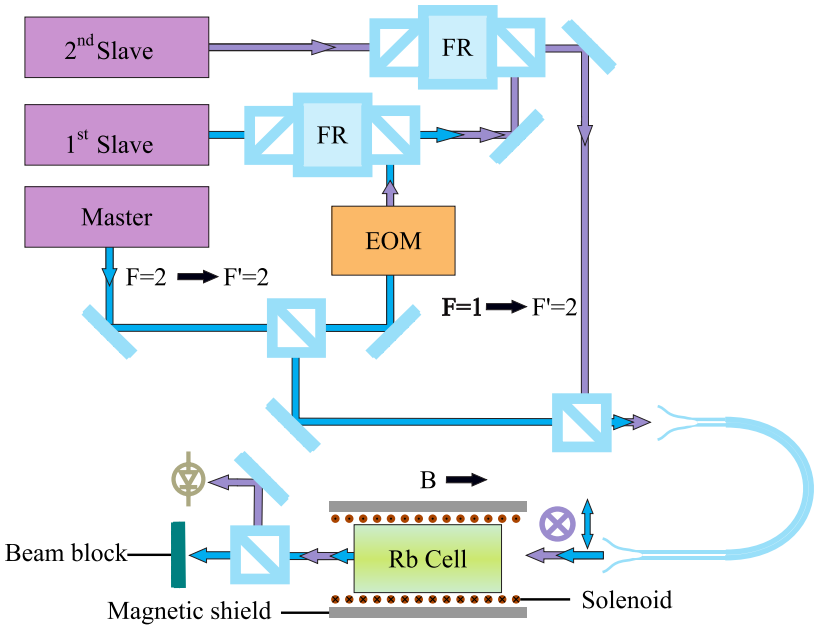

Figure 2.5: Schematic of the optical setup used to generate sidebands at 6.8 GHz. A master laser is locked on the F = 2 → F′ = 2 resonance and the beam passes through an electro-optic modulator (EOM) at 6.8 GHz. This light then passes through a Faraday Rotator (FR) and injection locks a slave laser to the lower sideband. The light from this laser then seeds a second slave laser; the output of which is combined with the master light on a polarising beam splitter cube and coupled into a fiber. The magnetic field direction is labelled B. The polarisation of each beam before the cell is indicated, with ⊗ being vertically polarised and ↕ horizontally.

shown in figure 2.5. The shielding is necessary to reduce broadening caused by external magnetic fields due to the Zeeman effect. The probe and coupling beams have a waist of 1.3 mm ($1/e^2$ radius) and have orthogonal linear polarisations. By changing the drive frequency of the EOM the probe beam can be scanned through the F = 1 → F′ = 2 resonance. A polarising beam splitting cube is used to pick off the coupling beam, allowing the probe transmission to be monitored as a function of detuning. An example of such resonance is shown in figure 2.7. The change in transmission, ΔT of the probe beam, which is calculated with $T = e^{-\alpha l}$ is monitored as a function of detuning. This change in transmission measured in the

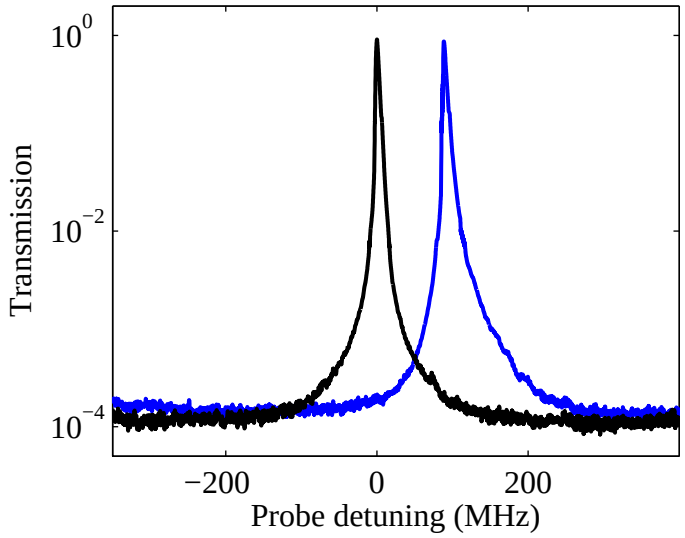

Figure 2.6: The spectral purity of the master (blue) and second slave laser (black) is observed by measuring the transmission through a scanning Fabry-Perot etalon with free spectral range ~ 750 MHz. No component of master light on the second slave laser frequency spectrum is detected down to the noise level; a suppression of at least -40 dB.

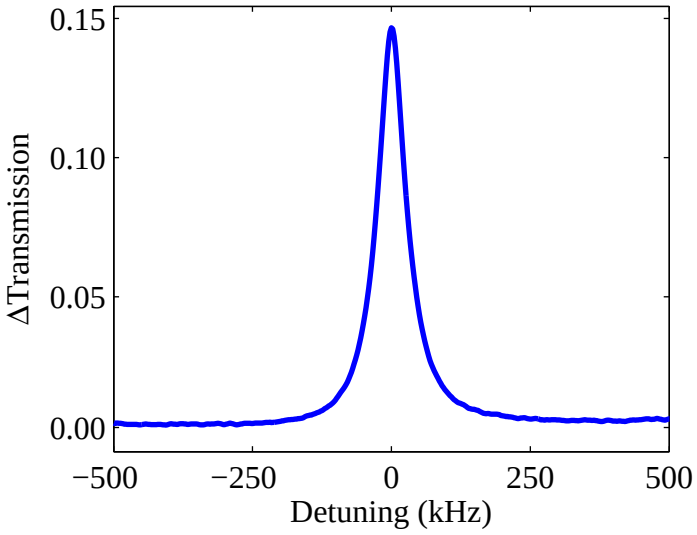

Figure 2.7: Measured EIT resonance under the Λ configuration. The change in transmission ΔT, explained in the text, is monitored as a function of probe detuning. Probe powers of 20 μW and coupling powers of 110 μW were used. The FWHM is $\simeq$ 70 kHz, which is consistent with the transit time estimate given in equation 2.36.

experiment is the deviation from the Doppler background with zero equating to no change in transmission and one corresponding to no absorption. Note that the the FWHM is around 70 kHz, and is primarily limited by transit time broadening as discussed in section 2.4.1. Moving away from the peak, the change in transmission reduces towards zero. This is in contrast to figure 2.2(b) where the EIT feature is imposed on a lorentzian background, and is due to all velocity classes in the thermal cell contributing to the signal, which is neglected in the original model for simplicity.

Chapter 3

N-system

Adding extra coupling fields to extend the 3-level system discussed in the previous chapter, can provide the means to control the dynamics associated with EIT. By coupling together the two metastable ground states in the Λ-system with a third field, the switching of light pulse propagation from sub- to super-luminal has been demonstrated [75, 76]. There is, however, no reason to confine investigations to 'just' three levels. By adding an extra ground state and coupling field to the Λ-system it is possible to enhance the Kerr non-linearity [77] of the medium. Also associated in this system is the emergence of a 'double dark' state, a splitting of the dark state resonance associated with EIT.

This double dark state is also seen in the $\mathcal{N}$-system. Such a system is formed by the addition of an excited state to the Λ-system [78, 79], and will be studied in this chapter. The two hyperfine ground states, $|1\rangle$ and $|3\rangle$, and two excited states $|2\rangle$ and $|4\rangle$ are shown in figure 3.1. The coupling fields, with Rabi frequencies, Ω_{21}, Ω_{32} and Ω_{43} correspond to the probe, coupling and 'control' laser fields respectively. The $\mathcal{N}$-system was the original candidate for achieving high Kerr non-linearities [43]. The system has also been used to study electromagnetically induced absorption (EIA) both theoretically [80] and experimentally [81].

3.1 Beam propagation directions in the $\mathcal{N}$-system

The relatively intuitive arguments regarding beam propagation presented in figure 2.3 are complicated by the inclusion of another coupling field, Ω_{43}. Practically

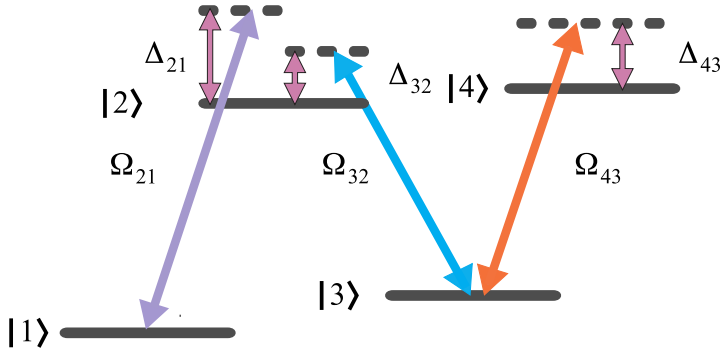

Figure 3.1: Energy level diagram for the $\mathcal{N}$-system. Three fields with Rabi frequency Ω_{ij} drive a 4-level system. The detunings from the excited states are given by Δ_{ij}. The laser beams resonant with transitions $|1\rangle \rightarrow |2\rangle$, $|2\rangle \rightarrow |3\rangle$, and $|3\rangle \rightarrow |4\rangle$ are referred to as the probe, coupling and control beams, respectively.

a choice between counter-propagating beams and co-propagating beams must be made. This problem is addressed in reference [82] by the use of dressed states [83]. The dressed state formalism involves a transformation from the bare eigenstates of the atom Hamiltonian to the combined eigenstates of the atom plus field Hamiltonian. By extracting the eigenvalues of this Hamiltonian the energies at which these states occur that is found. As detailed in appendix B, for a two-level system the total Hamiltonian is written as,

$$\mathcal{H}_{\text{two}} = \frac{\hbar}{2}\begin{pmatrix} 0 & \Omega_{21} \\ \Omega_{21} & -2\Delta_{21} \end{pmatrix}. \tag{3.1}$$

Diagonalising this results in:

$$\mathcal{H'}_{\text{two}} = -\frac{\hbar}{2}\begin{pmatrix} \Delta_{21} - \sqrt{\Omega_{21}^2 + \Delta_{21}^2} & 0 \\ 0 & \Delta_{21} + \sqrt{\Omega_{21}^2 + \Delta_{21}^2} \end{pmatrix}. \tag{3.2}$$

In the regime of $\Delta_{21} \gg \Omega_{21}$, then the shift in energies of the states are

$$\Delta E = \frac{\hbar\Omega_{21}^2}{4\Delta_{21}}. \tag{3.3}$$

As an example, figure 3.2 shows the dressed state energies of the two state system as a function of detuning, Δ_{21}. Here, zero energy corresponds to the unshifted

energy $\hbar\omega_0$ of the first excited state. The separation between the two states at zero detuning corresponds to $\hbar\Omega_{21}$ and is known as the Autler-Townes splitting.

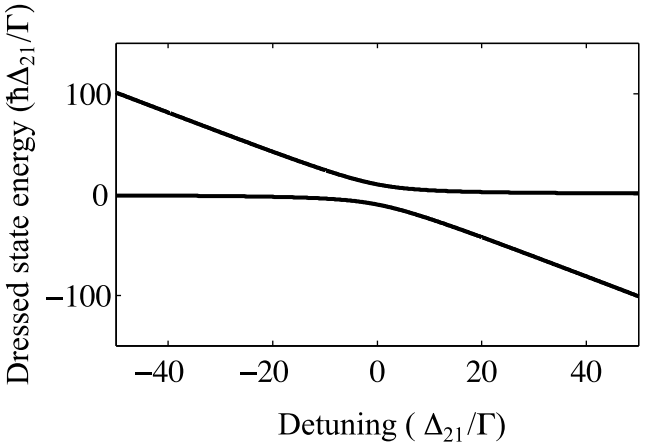

$$\mathcal{H}_{2\text{level}} = \frac{\hbar}{2}\begin{pmatrix} 0 & \Omega_{21} \\ \Omega_{21} & -2\Delta_{21} \end{pmatrix}$$

Figure 3.2: Dressed state energies in the two-level system for $\Omega_{21} = 5\Gamma$ and varied detuning parameter, Δ_{21}.

If the probe field is weak, it is possible to ignore its effects on perturbing the atomic energies in favour of concentrating on the effect of the stronger, coupling fields. This means that levels $|2\rangle - |4\rangle$ can be considered as a V-system; the action of the probe field is just to 'read' out where these energies lie. This simplification allows the Hamiltonians to be written as:

$$\mathcal{H}_{\text{co}} = \frac{\hbar}{2}\begin{pmatrix} -2(\Delta_{32} + \text{k}\upsilon) & \Omega_{32} & 0 \\ \Omega_{32} & 0 & \Omega_{43} \\ 0 & \Omega_{43} & -2(\Delta_{43} + \text{k}\upsilon) \end{pmatrix}, \tag{3.4}$$

where the wavevector magnitude k is the same for all fields. In the counter-propagating case,

$$\mathcal{H}_{\text{count}} = \frac{\hbar}{2}\begin{pmatrix} -2(\Delta_{32} + \text{k}\upsilon) & \Omega_{32} & 0 \\ \Omega_{32} & 0 & \Omega_{43} \\ 0 & \Omega_{43} & -2(\Delta_{43} - \text{k}\upsilon) \end{pmatrix}, \tag{3.5}$$

with the only difference being the change in sign of the detuning term in $\mathcal{H}(3,3)$. The analytical solutions for the counter-propagating case are far from simple. Instead it is easier to numerically calculate the new dressed state energies. This is shown in figure 3.3(a) and (b) which correspond to the counter-propagating and co-propagating case respectively for on resonance coupling beams, such that $\Delta_{32} = \Delta_{43} = 0$. To clarify the relevance to thermal ensembles, instead of varying

the probe detuning parameter, the shift in frequency due to the Doppler shift of different velocity classes is shown. In figure 3.3(a) there exists a dressed state energy which is stationary with respect to the velocity induced detuning, hence this resonance is Doppler free. In figure 3.3(b) however this is not the case, the dressed state energies are similar to that of the two level system in figure 3.2, with the addition of a third state. The fact that the co-propagating case is not Doppler free suggests that any resonances will not be detected once velocity averaging has been performed for each probe field detuning.

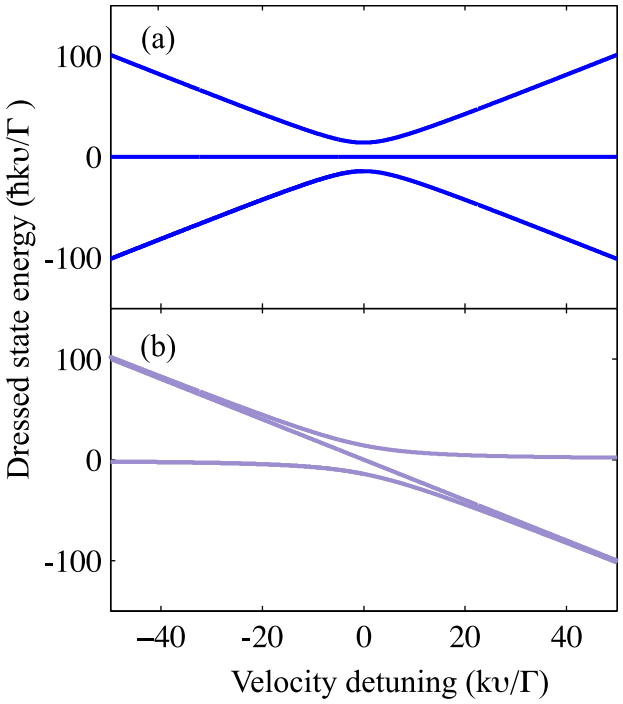

$$\mathcal{H}_{count} = \frac{\hbar}{2}\begin{pmatrix} -2k\upsilon & \Omega_{32} & 0 \\ \Omega_{32} & 0 & \Omega_{43} \\ 0 & \Omega_{43} & 2k\upsilon \end{pmatrix}$$

$$\mathcal{H}_{co} = \frac{\hbar}{2}\begin{pmatrix} -2k\upsilon & \Omega_{32} & 0 \\ \Omega_{32} & 0 & \Omega_{43} \\ 0 & \Omega_{43} & -2k\upsilon \end{pmatrix}$$

Figure 3.3: Dressed state energies in three-beam system for $\Delta_{32} = \Delta_{43} = 0$ and $\Omega_{32} = \Omega_{43} = 5\Gamma$. In (a), the blue line indicates the solution found by diagonalisation of the counter-propagation Hamiltonian. The co-propagating case is shown in (b), this solution is exact using both methods in this case. In (a) the counter-propagating case there is a stationary dressed state, while in (b) none exists.

Returning to the four-level system, the Hamiltonian is,

$$\mathcal{H}_N = \frac{\hbar}{2}\begin{pmatrix} 0 & \Omega_{21} & 0 & 0 \\ \Omega_{21} & -2\delta_{21} & \Omega_{32} & 0 \\ 0 & \Omega_{32} & -2(\delta_{21}-\delta_{32}) & \Omega_{43} \\ 0 & 0 & \Omega_{43} & -2(\delta_{21}-\delta_{32}+\delta_{43}) \end{pmatrix}, \tag{3.6}$$

where $\delta_{21} = \Delta_{21} + k\upsilon$, $\delta_{32} = \Delta_{32} + k\upsilon$ and $\delta_{43} = \Delta_{43} - k\upsilon$. Figure 3.4 shows

the absorption coefficients, α as a function of both probe laser detuning, Δ_{21} and velocity, υ, obtained by solving the master equation, 2.13 with the Hamiltonian from 3.6. While the difference between these two absorption profiles may be subtle, it is enough to change the subsequent transmission spectra obtained by summing over the velocity classes. The behaviour near to the zeroth velocity class is the key. While in 3.4(a), corresponding to the counter-propagating case, the 'island' formed around 0 ms^{-1} has a weak dependence on velocity class, the same isn't true for the co-propagating case. In 3.4(b) there is no such formation; rather a continuous line of weak absorption and two lines of a hyperbola similar to that seen in figure 3.1(c).

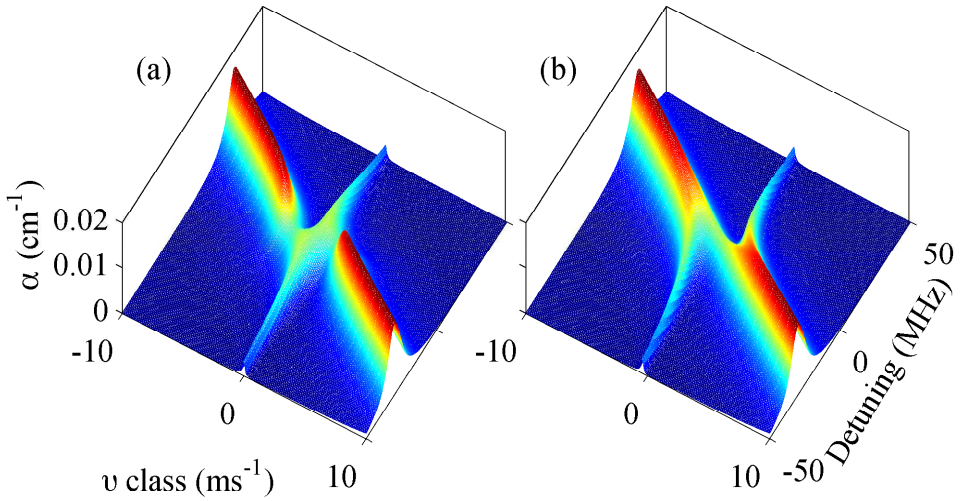

Figure 3.4: Absorption coefficients as a function of probe field detuning for the case of a counter-propagating, (a), and co-propagating, (b), Ω_{43} field. In both cases $\Delta_{32} = \Delta_{43} = 0$, $\Omega_{21} = (2\pi \times)$ 200 kHz and the coupling field have strengths, $\Omega_{43} = \Omega_{32} = (2\pi \times)$ 3 MHz. $\Gamma_{21} = (2\pi \times)$ 6 MHz is the natural decay rate of state $|2\rangle$ and $|4\rangle$. The number density, $N = 1.8 \times 10^9$ cm^{-3} and $\mathbf{d_{21}}$=2 ea_0.

Following a similar approach to [64], assuming that the population remains in the ground state $|1\rangle$, which is a good approximation in the weak probe limit, the coherence, σ_{21} is approximated [84] as

$$\sigma_{21} \simeq -\frac{i\Omega_{21}/2}{\gamma_{21} - i\delta_{21} + \dfrac{\Omega_{32}^2/4}{\gamma_{31} - i(\delta_{21} - \delta_{32}) + \dfrac{\Omega_{43}^2/4}{\gamma_{41} - i(\delta_{21} - \delta_{32} + \delta_{43})}}}. \tag{3.7}$$

Contrasting the contributions from different velocity classes, figure 3.5 illustrates the difference between the absorption properties of the Λ and $\mathcal{N}$-systems for the zero velocity class and a thermal ensemble. A thermal ensemble has a narrower EIT resonance due to the contribution from off-resonant velocity classes, as previously noted [79, 85–87]. This is shown in figure 3.5, where a zero velocity class in (a) has a broader resonance than the sum of the contributions from all velocity classes in (b).

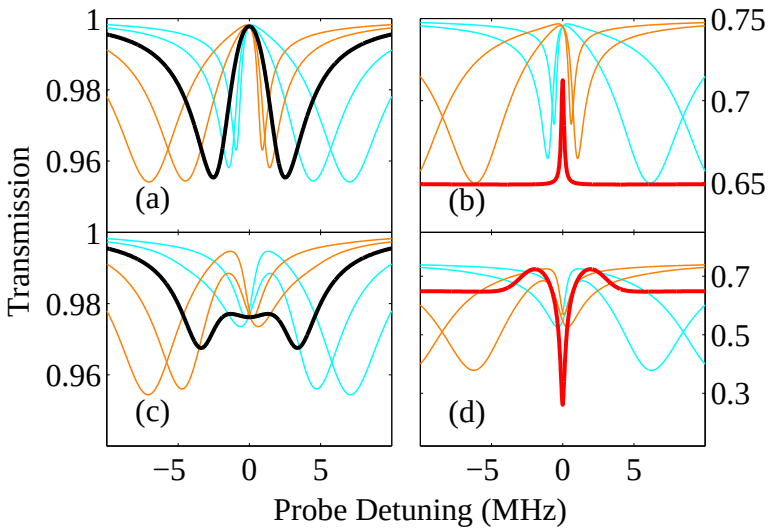

Figure 3.5: Probe transmission as a function of detuning for various velocity classes (a, c) and the sum of all contributions (b, d). The Λ-system is shown in (a) and (b), whilst the $\mathcal{N}$-system is shown in (c) and (d). In (a, c) the orange lines correspond to 6, 3 ms^{-1}, 0 ms^{-1} black and -3, -6 ms^{-1} in blue. In (b, d) the sum of all contributions is shown in red. The orange lines correspond to velocity classes of 10, 5 ms^{-1} and -5, -10 ms^{-1} classes in blue, for these four classes the absorption coefficient and offset have been rescaled to aid comparison. The calculation is for a 7.5 cm long Rb cell at room temperature with a Gaussian velocity distribution. In all cases Ω_{32}=$(2\pi\times)$ 5 MHz and states $|2\rangle$ and $|4\rangle$ have a decay of Γ=$(2\pi\times)$ 6 MHz, while γ_{31} = $(2\pi\times)$ 100 kHz to account for transit time broadening. In (c) and (d) Ω_{43}=$(2\pi\times)$ 5 MHz. The probe and coupling beams co-propagate while the control beam counter-propagates.

Interestingly the effect of adding a third laser field on the zero velocity class is to broaden and split the transmission peak, as in figure 3.5(c); for thermal atoms

the resonance switches from transmitting to absorbing, see figure 3.5(d)). This absorption is largest when the control and coupling Rabi frequencies are equal. The ~ 100 kHz width of this pronounced absorptive resonance remains both sub-Doppler and sub-natural, despite the coupling to an excited state [71]. Although similar absorptive resonances have been observed in previous work [82, 88], a width of over 20 MHz in the latter work means that the sub-natural character was not demonstrated. In this experiment the width is primarily limited by transit time broadening, whilst the extent of the resonance decreases for higher excited state decay rates. Analysing the contributions from various velocity classes, the evolution of the EIT resonance into an absorptive feature is dependent on the inclusion of velocity classes with velocities υ greater than Γ/k. The resulting transmission, corresponding to the sum of off-resonant velocity classes is depicted in figure 3.5(d). A narrow absorption feature would not be expected in a sample of cold atoms.

3.2 Experimental demonstration

The optical setup used to demonstrate the $\mathcal{N}$-system resonance is shown in figure 3.6 and is similar to that in section 2.5 with the addition of a extra 'control' beam to provide Ω_{43}. For near-resonant coupling to the $5^2S_{1/2}$(F' = 2) $\rightarrow$ $5^2P_{3/2}$(F = 3) ($|3\rangle \rightarrow |4\rangle$ in figure 3.1) transition, two AOMs shift a fraction of the master light, 267 MHz, to the blue. For larger detunings, namely those greater than the Doppler width, the strict frequency stability requirements can be relaxed. In this case, another external cavity diode laser (Sacher Lynx) is used, which is not stabilised relative to the other lasers. To detect a narrow EIT signal of width ~ 70 kHz, a probe power of 20 μW, coupling power of 110 μW was used; the resulting peak is shown in figure 3.7(a). By adding a control beam tuned to resonance as shown in figure 3.7(b), an absorptive resonance with sub-natural linewidth is seen, even though it is induced by coupling to a state with a natural decay width of 6 MHz. This resonance is in qualitative agreement with the predictions of the model shown in section 3.1, which indicated that off resonant velocity classes contribute to the effect. The enhanced absorption is however, smaller than that in figure 3.5. Primarily, this is due to the population in state $|3\rangle$ which is not included in the model depicted in figures 3.1 and 3.5. Implementing optical pumping would initialise

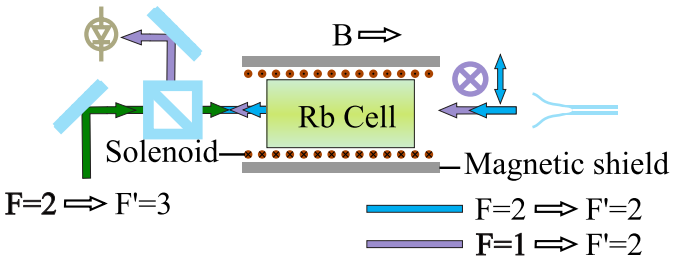

Figure 3.6: Optical schematic for observing narrow absorptive resonances. The probe and coupling beam co-propagate through a 7.5 cm Rb cell, while a 'control' beam counter-propagates to both these beams.

the population in state $|1\rangle$, closer to the situation modelled previously. The theory also assumes a closed 4-level system, which due to other hyperfine components in the excited state, is not true. The D1 line may also aid the observation of larger absorption; the larger hyperfine splitting in the excited state (362 MHz) means that the system would be closer to the ideal 4-levels.

Lifting the Zeeman degeneracy by applying ~1 G axial magnetic field results in similar, absorptive features, as seen in figure 3.7(c). Here, the three different EIT peaks correspond to EIT Λ systems composed of different m_F states. Figure 3.7(d) shows the couplings for σ^+ σ^+ transitions. No π transitions are expected in this Λ-system as the beam wavevectors are the same direction as the magnetic field. Resonances are expected at three frequencies, α, β and χ. Due to symmetry, σ^- σ^- couplings would be at the same frequencies, the same is true for mixed transitions, σ^+ σ^- and σ^- σ^+. As an example, $|2,-1\rangle \rightarrow |2,0\rangle \rightarrow |1,1\rangle$ occurs at the same probe frequency as the β system. The fact that the enhanced absorption happens in the presence of a weakly splitting magnetic field shows that the effect has a different origin to EIA that occurs in degenerate systems [80].

Transmission spectra for the $\mathcal{N}$-system for an off-resonant control beam are shown in figure 3.8(a). This control beam is tuned off resonance by approximately 5 GHz as shown in figure 3.8(b). The spectra show how the EIT feature shifts to lower frequency and broadens. The ground state, $|3\rangle$, is shifted via the ac Stark shift using equation 3.3. In figure 3.8(c) the predicted shift is compared to the measured shift and is in reasonable agreement. The broadening of the EIT peak can be explained as due to the spatially inhomogeneous intensity of the control laser field;

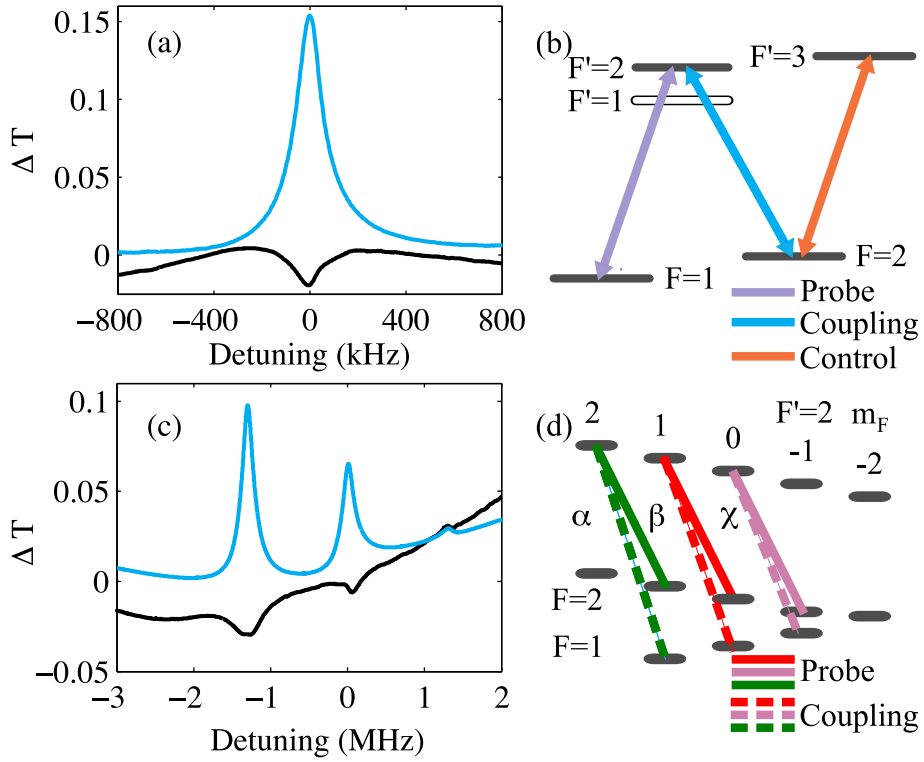

Figure 3.7: (a) Change in probe transmission as a function of detuning from the F = 1 → F' = 2 level, coupling beam on resonance, for no control beam (blue) and control beam on resonance (black). The level scheme for observation of sub-natural enhanced absorption is shown in (b). Both the coupling and control lasers are on resonance, and the probe laser is scanned through resonance. Despite the lifted Zeeman degeneracy using a ∼ 1 Gauss field, the absorptive resonance is still seen in (c). The relative peak heights are determined by optical pumping. The level scheme when only σ^+ transitions are present is shown in (d). EIT resonances are observed at energies α, β and χ due to the lifted Zeeman degeneracy. σ^- transitions are omitted for clarity.

each atom experiences a different shift due to its position in the laser field. By moving close to, but not on resonance, it is possible to Autler-Townes split the EIT peak [89] rather than just shift it. This effect is shown in figure 3.8(d) and (e). Again a weak magnetic field, is applied as well as a 110 μW control beam detuned by -5 MHz.

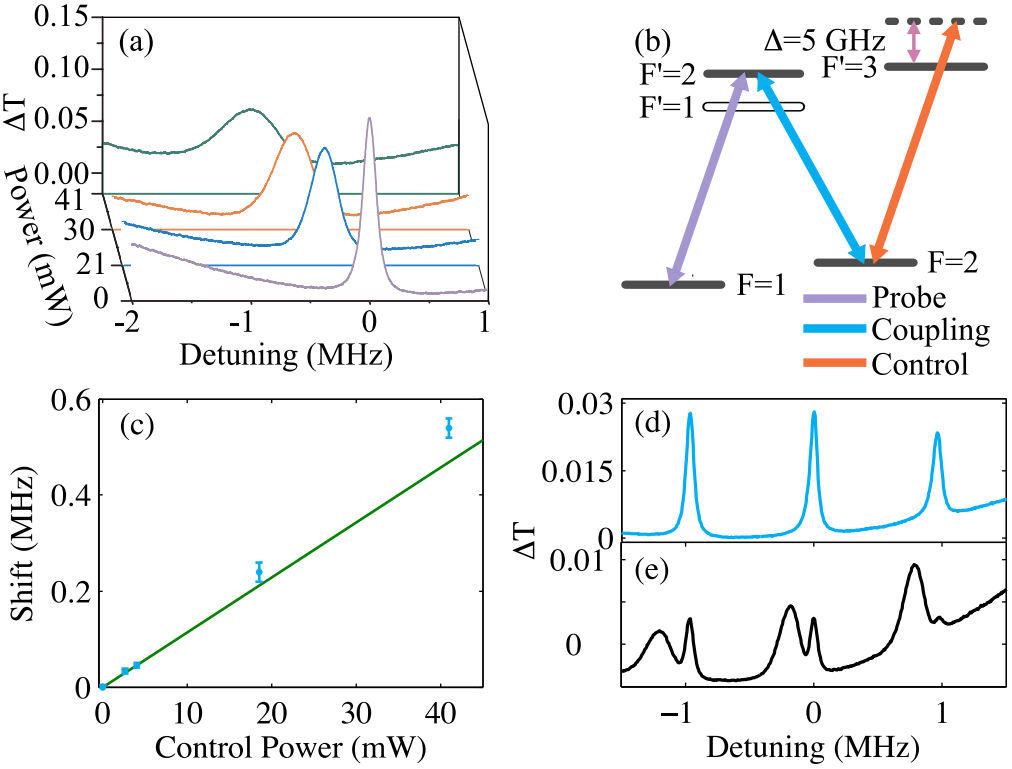

Figure 3.8: (a) Change in transmission as a function of detuning from the $5^2S_{1/2}(F = 1) \rightarrow 5^2P_{3/2}(F' = 2)$ level. (b) Level scheme for the $\mathcal{N}$-system with a far off-resonant control field is used to shift the F = 2 ground state. (c) Shift in frequency of EIT peak for various control beam powers. Data points are taken from (a), whilst the solid line is the calculated ac Stark shift. (d) Change in probe transmission as a function of detuning from the $F = 1 \rightarrow F' = 2$ level, with a small magnetic field of order 1 Gauss to lift the degeneracy in the F = 1 and F = 2 ground states. In (d) three peaks in transmission are seen for no control beam. A control beam with 110 μW, detuned by -5 MHz from the F' = 3 level, is applied to split the peak in (e).

3.3 Outlook

The ability to create narrow absorptive resonances could be employed to enhance the optical depth of an otherwise optically thin sample with potential applications in detecting weak absorption lines. Also through the change in refractive index associated with the Λ-system a reduction in group velocity also occurs; with the narrower features resulting in a greater slowing. The propagation of light pulses has thus been reduced using this effect [14, 19, 90]. Correspondingly the ability to switch between narrow transparent and absorptive resonances results in a switching between sub- and super-luminal propagation. It has been shown here how this switching from transmitting to absorbing can be achieved using a control beam. In the next chapter, a new mechanism for controlling this phenomenon using Rydberg states will be presented.

Chapter 4

Rydberg EIT

The addition of a 'control' beam is just one way of manipulating atomic coherences. By using an EIT system composed of Rydberg states, the electric field sensitivity of these highly excited states can be exploited. This is due to the high polarisabilities of Rydberg states, the propensity of a charge distribution to be distorted by an electric field. The frequencies at which light is resonant with Rydberg states is dependent on the magnitude of the external electric field. By exploiting the Stark shift it is possible to 'tune' these states into resonance, akin to altering the detuning of a near resonant laser field. Thus the inclusion of a Rydberg state in an extended $\mathcal{N}$-system will facilitate electric field dependent dynamics. This is not the only reason to study these systems, being able to perform Ryberg EIT opens up a number of interesting experiments, indeed the rest of this work will be dedicated to a few of these investigations.

To facilitate the step towards a Rydberg $\mathcal{N}$-system, this chapter will first address the relatively simpler three level cascade or ladder system. While it is possible to directly address the Rydberg state, the short wavelength of 297 nm neccesary to reach a Rydberg state is rather prohibitive due to the avaliability of laser sources. The extension of ladder EIT to Rydberg states was first performed in Durham, [50] where the fine structure splitting of the D state in Rb was measured. One useful feature of Rydberg EIT is the ability to detect Rydberg states in cold samples without losing the atoms. In most experiments using Rydberg atoms, the atom is first ionised and then the charged ions are detected using a micro channel plate (MCP). All-optical detection of Rydberg states was subsequently demonstrated

using cold atoms [56], again by the group of Adams in Durham.

4.1 Properties of Rydberg atoms

A Rydberg state is a state of an atom or molecule where one or more of the electrons have been excited to a high principal quantum number orbital. The use of 'high' is somewhat subjective, but usually accounts for atoms in states with principal quantum number, $n \geq 10$. Conceptually it is convenient to take Bohr's model of the atom and extract from it various parameters that dictate an atom's behaviour. It should be noted however that one can explain the properties of Rydberg atoms more accurately by using the Schrödinger equation.

4.1.1 Energy of Rydberg states

Employing Bohr's approach, the orbital radius, r_{B} of a Rydberg atom is large compared to the ground state, roughly 9 times larger for $n = 15$. At the centre of the atom lies the charge core with Z protons, this is mostly shielded by the other $Z-1$ electrons. However the remaining electron is further away from the nucleus and experiences a different Coulomb potential. Depending upon the angular momentum state of the electron, this can be close to the Hydrogen potential. The energy, E of a state is thus modified from that of Hydrogen,

$$E_n = -\frac{Rhc}{n^2} \quad \Rightarrow E = -\frac{Rhc}{(n-\delta(n))^2} \ , \tag{4.1}$$

where R and h are the Rydberg and Plank constants, c is the speed of light and $\delta(n)$ is the quantum defect. In fact, this quantum defect is a measure of the departure from the case of Hydrogen. Such is the precision at which these measurements are made, this defect is not a single number, but actually dependent on n, [25].

$$\delta(n) = \delta_0 + \frac{\delta_2}{(n-\delta_0)^2}. \tag{4.2}$$

Typical values for Rb are shown in table 4.1. Bohr's model of the atom also provides insight into the orbital radius of the electron,

$$r_B = \frac{4\pi\epsilon_0\hbar^2 n^2}{\mathrm{e}^2 m_{\mathrm{e}}} = a_0 n^2 \tag{4.3}$$

Angular momentum state	δ_0	δ_2
$S_{1/2}$	3.131804 (10)	0.1784(6)
$P_{1/2}$	2.6548849 (10)	0.2900(6)
$P_{3/2}$	2.6416737(10)	0.2950(7)
$D_{3/2}$	1.34809171(40)	-0.60286(26)
$D_{5/2}$	1.34646572(30)	-0.59600(18)
$F_{5/2}$	0.0165192(9)	-0.085(9)
$F_{7/2}$	0.0165437(7)	-0.086(7)

Table 4.1: Quantum defects for different states in Rubidium. All values taken from reference [91] apart from the F series, taken from [92].

where a_0 is the Bohr radius in terms of the permitivity of free space, ϵ_0, electron mass, m_e and electron charge e. In quantum mechanics expectation values are more appropriate, calculating the wavefunctions and consequently the expectation values yields [25],

$$\langle \hat{r} \rangle = \frac{3n^2 - \ell(\ell+1)}{2} \,. \tag{4.4}$$

4.1.2 Polarisability

Considering the atom's response to an electric field $\mathcal{E}$, using second order perturbation theory the atomic energy level energy is,

$$E_i = E_i^0 + \langle i^0 | V | i^0 \rangle + \sum_{i \neq k} \frac{|\langle k| V |i\rangle|^2}{E_k^0 - E_i^0} \,, \tag{4.5}$$

where E_i^0 and E_k^0 are the unshifted energies of states i and k, $V = -\mathrm{d} \cdot \mathcal{E}$ is the interaction energy due to the application of an external electric field. The second term equates to zero due to parity such that the change in energy is

$$\Delta E = \sum_i \frac{|\langle k| d |i\rangle|^2 \mathcal{E}^2}{E_k^0 - E_i^0}. \tag{4.6}$$

It shall be convenient to analyse the dependencies of these on the principal quantum number n. Addressing the numerator, the n dependence on the dipole matrix element d_{ik} is

$$d_{ik} = -\langle i| ez |k\rangle \tag{4.7}$$

$$= -\langle i| er\cos\theta |k\rangle \tag{4.8}$$

As shown in equation 4.3 and 4.4 the expectation of the radius scales as n^2. Calculating the separation between states is akin to asking how the density of states changes with n. As the energy of a state scales as n^{-2} as shown in 4.1, thus

$$\frac{dE_n}{dn} \propto n^{-3} \tag{4.9}$$

Using these scalings in equation 4.6 leads to the response to the external electric field

$$\Delta E \propto n^7 \mathcal{E}^2. \tag{4.10}$$

This restates the equation for the stark shift of a state,

$$\Delta E = \frac{1}{2}\alpha\mathcal{E}^2, \tag{4.11}$$

i.e. that the polarisability $\alpha \propto n^7$. It is possible to derive other properties of the atoms by similar means, in the interest of brevity they shall just be quoted here.

Property	n dependence
Binding energy	n^{-2}
Energy separation between states	n^{-3}
Orbital radius	n^2
Dipole moment	n^2
Polarisability	n^7
Radiative lifetime	n^3
Rabi frequency (constant laser power)	$n^{-3/2}$

Table 4.2: Scalings with principal quantum number in Rydberg atoms, taken from [25].

4.2 Experimental demonstration

The level scheme for Rydberg excitation is shown in figure 4.1, a probe laser is scanned over the $5S_{1/2} \rightarrow 5P_{3/2}$ resonance in Rb using a diode laser at 780.2 nm. The second stage is performed using a doubled diode laser system, Toptica SHG-TA aound 479-484 nm. With this laser it is possible to access a wide range of

Rydberg levels, from n = 18–124 [50], where the limit on n is set by the finite output power, around 200 mW. The wavelength of this laser is tuned using a High Finesse wavemeter, and the state energies are taken from reference [93]. Due to the n^{-3} dependence of the energy level separation, it is possible to tune the laser over a large number of states.

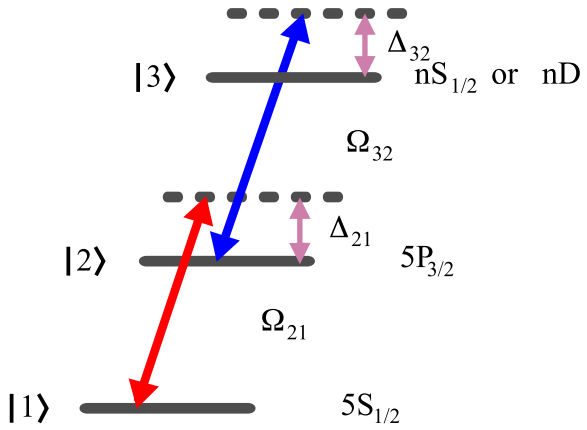

Figure 4.1: Level scheme for Rydberg EIT

Following a similar approach to that in section 2.3, beam propagation in the ladder system should aim to cancel the out the Doppler shift. A counter-propagating probe and coupling configuration is used in this case as the third state $|3\rangle$ has a higher energy in this system. This means that a probe laser tuned above the intermediate state $|2\rangle$ with detuning $k_p\upsilon$ requires a Doppler shift of $-k_c\upsilon$ to be resonant with the upper state.

4.3 Wavevector mismatch

The difference in wavevector magnitudes means that this cancellation of Doppler broadening is only partial. For multiple intermediate states, the detunings at which these are detected rescale according to the wavevector ratio, see figure 4.2.

(a)

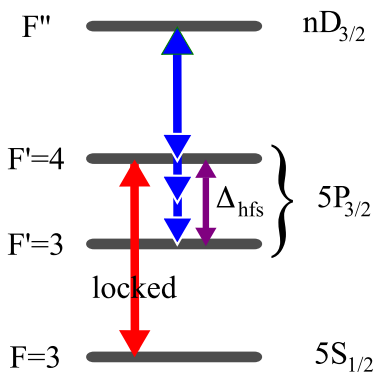

To be resonant with the probe laser there exists a velocity class which satisfies the condition.

$$\Delta_{\text{hfs}} = k_p \upsilon. \tag{4.12}$$

This is resonant with the $F' = 3$ transition. The necessary detuning of the coupling beam is thus

$$\Delta_c = -k_c \upsilon + \Delta_{\text{hfs}}. \tag{4.13}$$

Rearranging,

$$\begin{aligned} \Delta_c &= -k_c \frac{\Delta_{\text{hfs}}}{k_p} + \Delta_{\text{hfs}} \\ &= \Delta_{\text{hfs}} \left(1 - \frac{k_c}{k_p}\right) \\ &= \Delta_{\text{hfs}} \left(1 - \frac{\lambda_p}{\lambda_c}\right). \end{aligned} \tag{4.14}$$

(b)

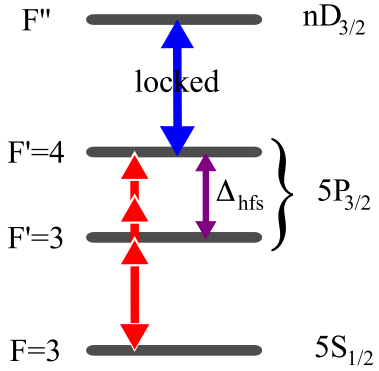

Similarly for the coupling beam being locked on resonance,

$$\Delta_{\text{hfs}} = k_c \upsilon \tag{4.15}$$

$$\Delta_p = -k_p \upsilon + \Delta_{\text{hfs}} \tag{4.16}$$

$$= \Delta_{\text{hfs}} \left(1 - \frac{\lambda_c}{\lambda_p}\right) \tag{4.17}$$

Figure 4.2: Wave-vector mismatch in the ladder system. In (a) the probe beam is locked on the F = 3 → F' = 4 transition and the coupling beam in scanned. The alternative situation is illustrated in (b), where the coupling beam is locked to the F' = 4 → F" transition and the probe beam is scanned.

This is in contrast to conventional hyperfine-pumping/saturation absorption spectroscopy where the probe and coupling beams have the same wavevector magnitude; under these conditions the separation of resonant peaks match the hyperfine splittings. As expected for $\lambda_p = \lambda_c$, equation 4.17 the detunings at which the resonances are detected are the same as the hyperfine splittings. Another consequence is that while Rydberg EIT resonances are sub-natural, they are limited to around 2 MHz because of this mismatch.

In many situations, such as due to phase modulation, the probe beam can acquire sidebands. In this case extra peaks arise in the EIT spectrum. Considering a modulation of a locked probe beam with sidebands at Δ_m, a velocity class,υ is resonant with a scanning coupling beam,

$$\Delta_m = k_p \upsilon. \tag{4.18}$$

Thus,

$$\Delta_c = -\frac{\lambda_p}{\lambda_c}\Delta_m. \tag{4.19}$$

Correspondingly when a frequency stabilised coupling beam is modulated and the probe beam is scanned.

$$\Delta_p = -\frac{\lambda_c}{\lambda_p}\Delta_m. \tag{4.20}$$

A typical absorption spectrum is show in figure 4.3. A probe laser is scanned across the D2 resonance in Rb. The Rydberg EIT resonance is seen on top of the Doppler background of the ^{87}Rb and ^{85}Rb; the former isotope giving rise to the absorption at larger negative detuning. One way to factor out the Doppler background, is by frequency stabilising the probe laser and scanning the coupling laser. Using polarisation spectroscopy [72] to lock to the $5S_{1/2}$(F=2) $\rightarrow$ $5P_{3/2}$(F' = 3) transition in ^{87}Rb, the change in probe transmission is monitored as a function of coupling laser detuning is shown in figure 4.4. The presence of three resonances in the spectrum is due to the contributions come from the intermediate state, $5P_{3/2}$. Using equation 4.17 to predict the location of the central peak, corresponding to the contribution from the F'=2 state. With λ_p = 780 nm and λ_c = 480 nm, the peak is expected around -167 MHz, which is in reasonable agreement with figure 4.4. Another interesting feature is the absorptive 'wings' either side of the transparency peak. These arise due to the off-resonant velocity classes, [50, 94]. For

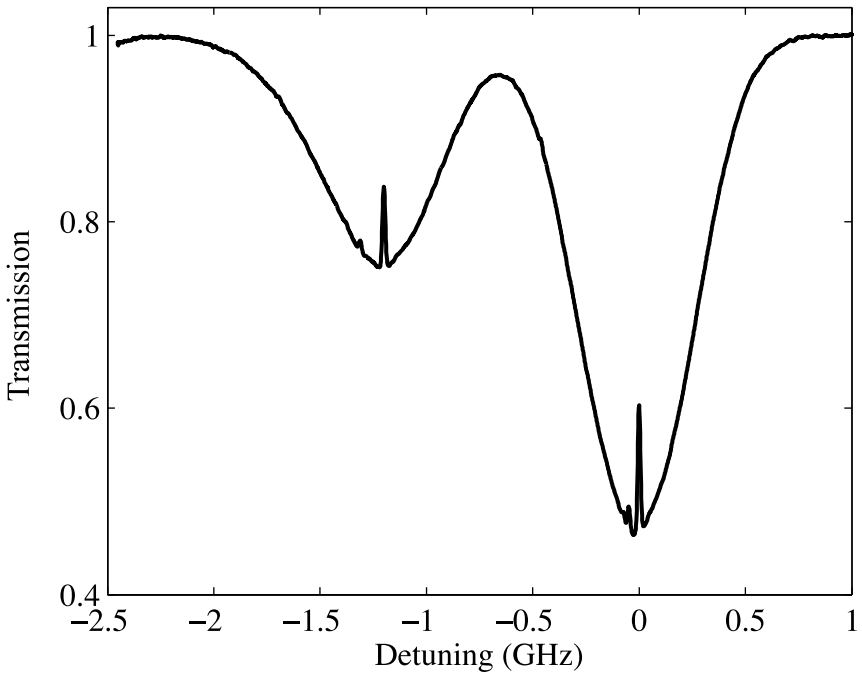

Figure 4.3: Rydberg EIT spectrum corresponding to the case of a probe laser around the D_2 transition in ^{87}Rb and ^{85}Rb. The coupling beam is resonant with the $27D_{5/2}$ state and has a power of 80 mW, while the probe beam has less then 1 μW.

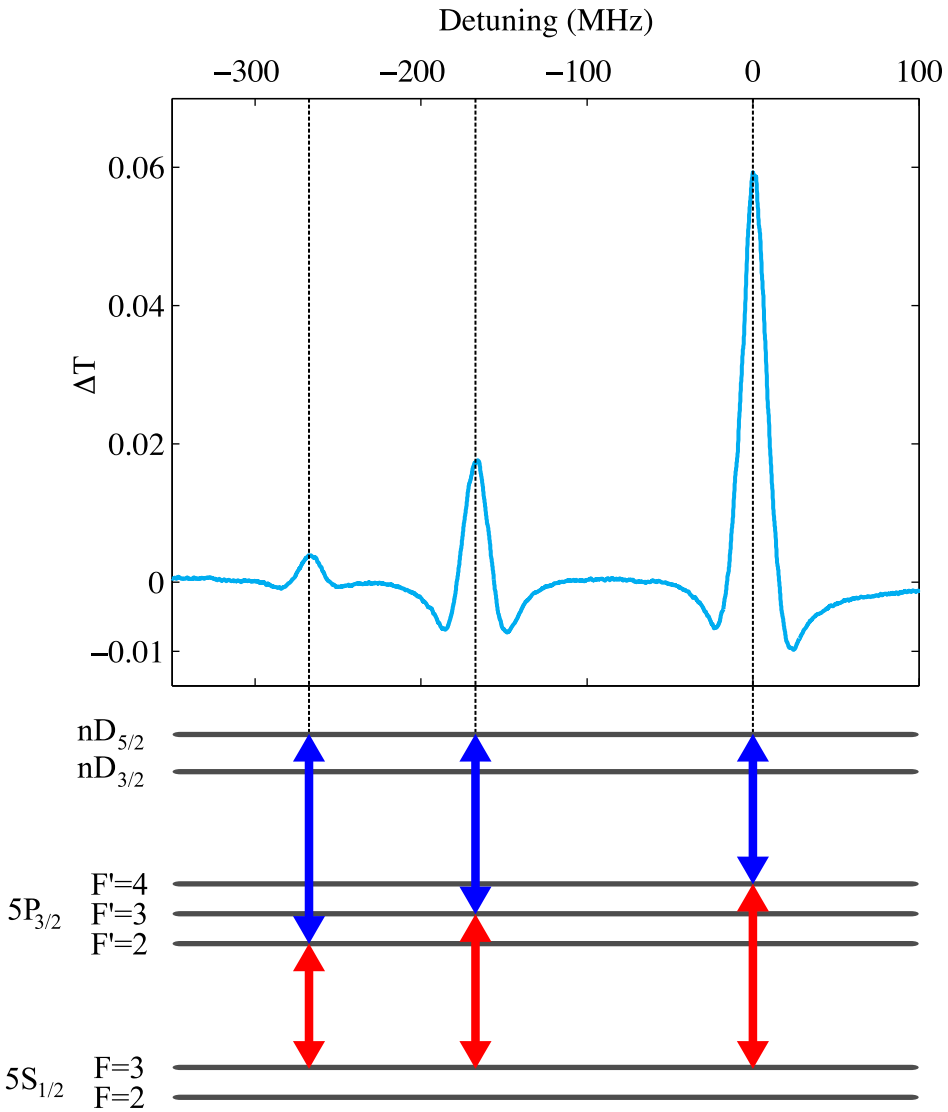

Figure 4.4: Typical Rydberg EIT spectrum corresponding to the case of a coupling laser and a probe laser locked to the $5S_{1/2}(F = 3) \rightarrow 5P_{3/2}(F' = 4)$ in ^{85}Rb and the coupling laser is scanned across the $27D_{5/2}$ resonance. The three EIT peaks in the spectrum corresponding to contributions that come from the intermediate $5P_{3/2}$ state as shown. Probe power 2 μW and coupling power 100 mW.

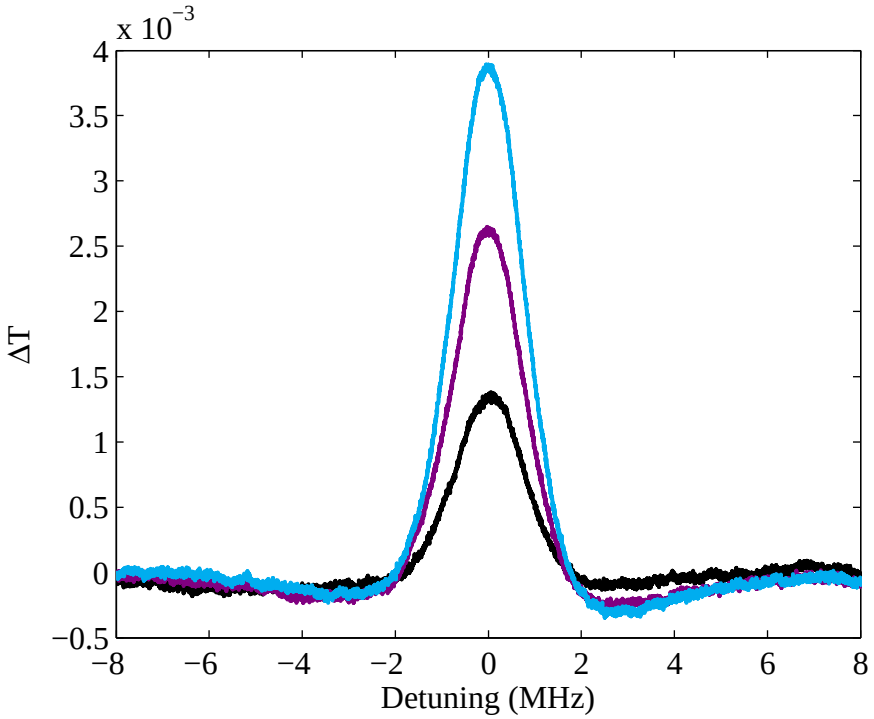

Figure 4.5: Using an acousto-optic modulator, the probe beam is scanned at 100 Hz around the $5S_{1/2}(F = 3) \rightarrow 5P_{3/2}(F' = 4)$ resonance in ^{85}Rb. The Rydberg coupling laser is resonant with the $5P_{3/2}(F = 4) \rightarrow 46S_{1/2}$ transition. Various powers of this blue laser are used, namely 20 mW black, 40 mW purple and 50 mW blue. The probe beam power is 390 nW.

a low probe power, the EIT peak width narrows to around 2 MHz as detailed in figure 4.5. This width is roughly the same for all different coupling powers, and is set by the wavevector mismatch. The probe power equates to an intensity of . The control laser is locked using a Rydberg EIT signal in another cell [55] and the probe laser using polarisation spectroscopy. The probe light is then scanned using an AOM. Using the empirical formula [25, 95]

$$\tau = \tau_0(n^{*2.94}) \,, \tag{4.21}$$

where τ is the expected lifetime of the $S_{1/2}$ state, τ_0 is 1.43 ns, for $n = 46$, the lifetime of the Rydberg state is around 90 μs. Thus it might be expected that a narrower feature would occur. However as previously indicated this fact that this doesn't occur is due to the wavevector mismatch.

4.4 Rydberg $\mathcal{N}$-system

The Rydberg $\mathcal{N}$-type level scheme combines the narrow features of the Λ-system with the sensitivity to electric field of the Rydberg state. The level scheme is shown in figure 4.6, where a 5 level system is formed from the addition of a Λ-system ($|1\rangle \rightarrow |2\rangle \rightarrow |3\rangle$) and a ladder EIT system ($|3\rangle \rightarrow |4\rangle \rightarrow |5\rangle$).

The Hamiltonian of this system is

$$\mathcal{H}_{\mathcal{RN}} = \frac{\hbar}{2}\begin{pmatrix} 0 & \Omega_{21} & 0 & 0 & 0 \\ \Omega_{21} & -2\delta_{21} & \Omega_{32} & 0 & 0 \\ 0 & \Omega_{32} & -2(\delta_{21}-\delta_{32}) & \Omega_{43} & 0 \\ 0 & 0 & \Omega_{43} & -2(\delta_{21}-\delta_{32}+\delta_{43}) & \Omega_{54} \\ 0 & 0 & 0 & \Omega_{54} & -2\delta_a \end{pmatrix}, \tag{4.22}$$

where $\delta_{21} = \Delta_{21} + \mathrm{k}_p\upsilon$, $\delta_{32} = \Delta_{32} + \mathrm{k}_p\upsilon$, $\delta_{43} = \Delta_{43} - \mathrm{k}_p\upsilon$, $\delta_{54} = \Delta_{54} - \mathrm{k}_c\upsilon$ and $\delta_a = \delta_{21} - \delta_{32} + \delta_{43} + \delta_{54}$. The terms k_p and k_c refer to the wavevectors of the 780 and 480 nm beams. Just as in chapter 3, the population and coherence of states decay at rates γ_i and $\gamma_i/2$ respectively. The hyperfine splitting of the $5P_{3/2}$ state is not included in this model; contributions from these states will alter the populations and thus coherences in the experiment.

In figure 4.7 the absorption coefficients are calculated for a weak probe beam passing through an ensemble at room temperature. Doppler averaging has been

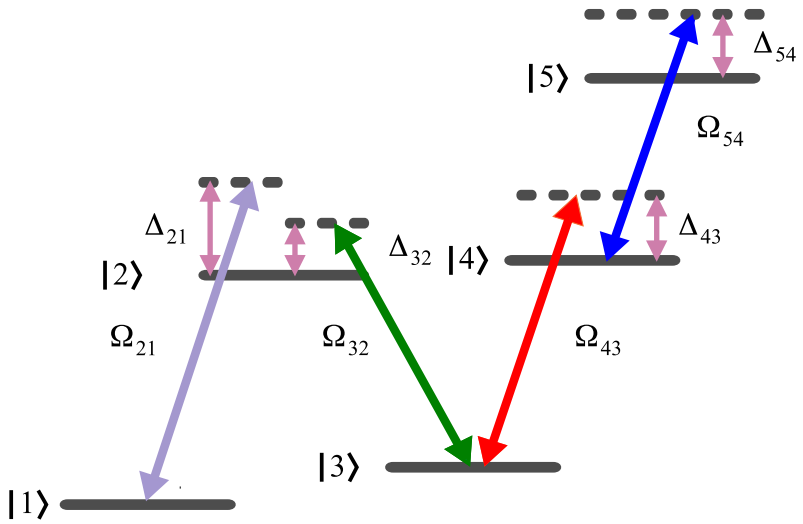

Figure 4.6: The Λ-system ($|1\rangle \rightarrow |2\rangle \rightarrow |3\rangle$) is coupled to a Rydberg state, $|5\rangle$ via an intermediate state, $|4\rangle$.

used to account for this variation in atomic velocities, υ. Figure 4.7(a) shows the absorption coefficient for the case of no Ω_{54} i.e. no coupling to the Rydberg state in black, while this beam is added for the purple trace. The difference between these cases is shown in 4.7(b). The presence of the Rydberg coupling beam changes the transmission through the medium from the narrow absorption seen in chapter 3, the black trace in 4.7(a), back to transmitting. The Rabi frequency needed to achieve this switching is correspondingly large due to the longer lifetime of the Rydberg state. The laser power needed to achieve this switching is not available in this work. Instead it is neccessary to detect that change in signal, rather than the 'absolute' signal. The difference signal shown in figure 4.7 (b) is a similar shape for weaker couplings. As the final state has a high polarisability the application of an electric field changes the detuning parameter. Thus the Rydberg state would be shifted out of resonance and the resultant absorption returns to the case of no Rydberg coupling field.

4.4.1 Experimental realisation of the Rydberg dark resonance

The experimental setup for the Rydberg $\mathcal{N}$-system is shown in figure 4.8. The Λ-system is coupled to a Rydberg state using a 2-photon excitation scheme, as

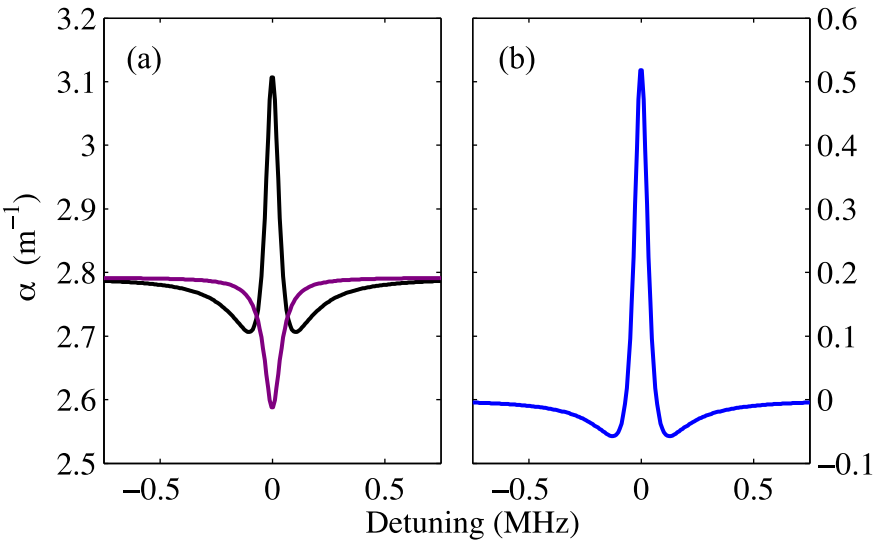

Figure 4.7: Absorption coefficient in the Rydberg N-system as a function of probe field detuning, Δ_{21}. The black trace shows the case of no Rydberg coupling field, while a field of strength Ω_{54}=(2π $\times$) 15 MHz shown by the purple trace. The difference between these signals is shown in (b), which corresponds to the expected experimental signal. Other model parameters, Ω_{21}=(2π $\times$) 10 kHz, Ω_{32} = Ω_{43} =(2π $\times$) 200 kHz. All other beams are on resonance, Δ_{32} = Δ_{43} = Δ_{54} = 0. Γ_2 = Γ_4=(2π $\times$) 6 MHz, Γ_5=(2π $\times$) 100 kHz. Coherence γ_{31}=(2π $\times$) 70 kHz is included to account for transit time broadening of the atoms moving through the laser beams, as in section 2.4.1.

described in section 4.2. The first stage of the ladder system, the control beam, is produced by shifting a portion of the coupling beam using two AOMs, as described in chapter 3. The laser powers incident on the cell are 10 μW, 35 μW and 40 μW for the probe, coupling and control beams respectively. The coupling to the Rydberg state is achieved using the frequency doubled diode laser system resonant described in section 4.2. This provides a driving field on resonance with the $5P_{3/2}(F' = 3) \rightarrow nD_{5/2}(F'')$ transition. The 2-photon resonance is driven by

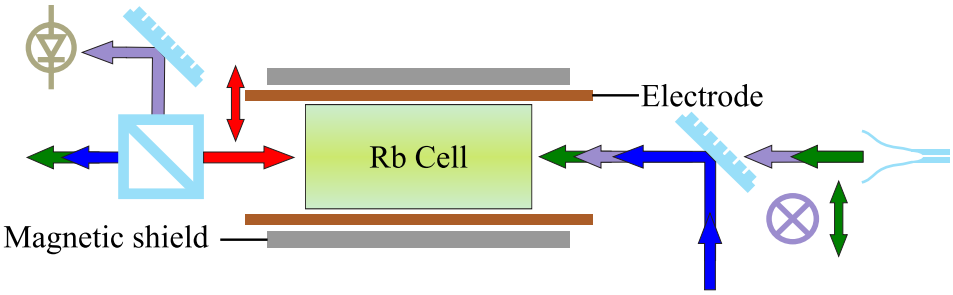

Figure 4.8: Schematic of the experimental set-up used for demonstration of the Rydberg $\mathcal{N}$-system. Three beams co-propagate through the cell, namely the two beams necessary for the Λ-system (purple and blue) and the beam needed for the second stage of the Rydberg excitation (green). Counter-propagating to these is the first step of Rydberg excitation (orange). The probe and coupling beams have a waist of 1.3 mm ($1/e^2$ radius)

counter-propagating beams in the vapor cell with the 2nd step co-propagating with the Λ-system beams as in figure 4.8. The 480 nm beam has a power of 140 mW and a waist of 0.8 mm ($1/e^2$ radius). The waist size is a trade-off between mode-matching with the 780 nm beams and achieving a high Rabi frequency. The Rb vapor cell is placed between two copper bar electrodes and inside a single layer magnetic shield. The 480 nm laser is frequency stabilized using a ladder system Rydberg EIT signal in a second Rb vapour cell.

The Λ-system resonance is shown in figure 4.9(a), and is the same width as in chapter 2. Using a chopper wheel, amplitude modulation is performed on the 480 nm laser beam at a frequency of 35 kHz. This allows a lock-in amplifier to detect the change in probe transmission due to the presence of the Rydberg cou-

pling beam. The lock-in signal corresponding to the change in Λ-system is shown in 4.9(b). As this signal is sensitive to the presence of the 480 nm laser, it is lost when this beam is blocked as is the case for the other three beams. Qualitatively it has the same shape as that predicted in figure 4.7. The size of the switching is only at the 1% level, due to the insufficient Rabi frequency on the Rydberg coupling transition. The Rydberg $\mathcal{N}$-system allows the mapping of high electric

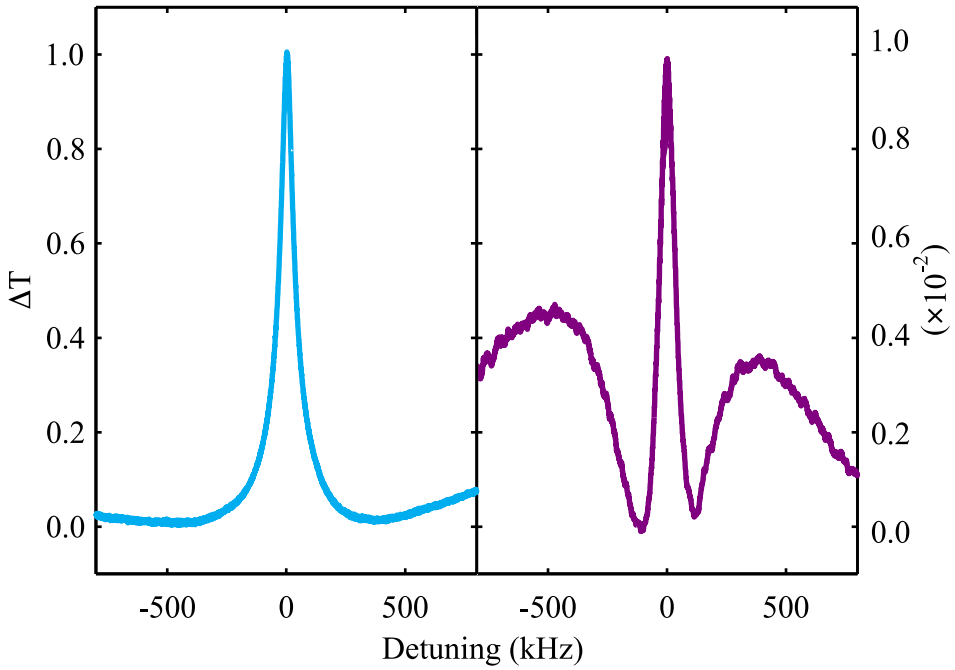

Figure 4.9: In (a) the change in transmission, ΔT for the Λ-system resonance is normalised to one. The Rydberg 5-level system resonance signal is shown in (b). This corresponds to the difference between the Λ-system resonance with Rydberg coupling (n = 26) and without; made using a lock-in amplifier. Beam parameters are 36 μW probe beam power, 380 μW coupling beam power, 230 μW control beam power and 140 mW blue coupling beam power.

field sensitivity to a ground state coherence. To demonstrate this sensitivity, an ac electric field with frequency 20 MHz is applied to the copper bar electrodes as shown in 4.8. It is not possible to use a dc field due to charge screening [50]. Charged electrons and ions generated by photo-desorption due to effect of the 480 nm beam on the Rubidium present on the cell wall. By applying a dc electric field, these charged particles move so as to cancel the applied field in the centre of the cell, thus no effect on the Rydberg spectra is seen. To circumvent this problem,

it is possible to use a rf (radio frequency) field; the field changes faster than the response time of the charges and no screening is seen.

The Rydberg resonance is monitored as a function of rms field; the peak height dependence is shown in figure 4.10. A suppression of the resonance is shown for an electric field of around 1 Vcm^{-1}. As the $44^2D_{5/2}$ state can be de-composed into $|m_J| = 1/2, 3/2$ and $5/2$, the switching of the resonance depends upon each of these components moving out of resonance. The $|m_J| = 5/2$ component shifts out of resonance at lower fields (of order 0.1 Vcm^{-1}) while the other two components have a smaller polarisability and shift out of resonance at 0.9 Vcm^{-1} [53].

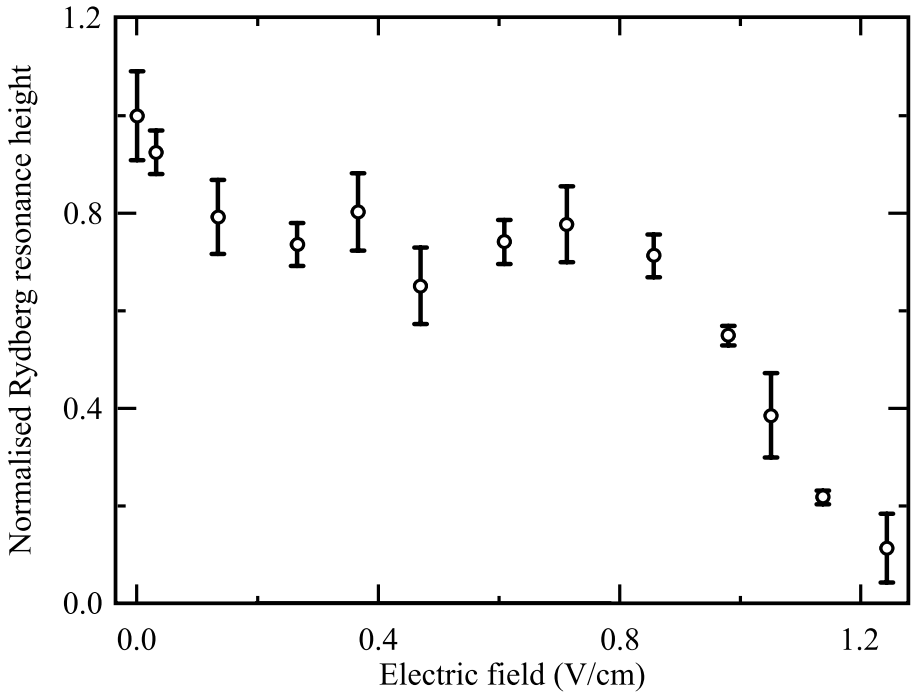

Figure 4.10: Electric field dependence of the 5-level Rydberg absorptive resonance using the state 44D. Probe power 11 μW, Coupling power 34 μW, control beam power 41 μW and blue laser power of 55 mW measured after the chopper wheel. An ac field at 20 MHz and various strengths is applied to suppress the resonance.

4.5 Outlook

The ability to switch an EIT resonance with an external electric field could have applications in electro-optic switching. However as has been shown, the size of the effect needs to be enhanced. As the Rabi frequency for the Rydberg transition is the limiting factor, an increase in the laser power would be beneficial. However this is limited by the availability of narrow-band high power laser sources around 480 nm. By focussing this beam, the intensity could increase, however to maintain beam overlap, the other three beams would also need to be focussed. If this approach was taken, then there would be a range of Rabi frequencies across the 7.5 cm cell.

One way around this problem would be to use much shorter cells. If the length of the cell is comparable to the Rayleigh range of the focus beams, then the Rabi frequency would be roughly constant. If the whole ensemble is restricted to such a small volume, then the dipolar nature of Rydberg atoms start to play a role. Rydberg-Rydberg interactions perturb the energies of neighbouring atoms. The existence of just one Rydberg atom can suppress the excitation of other atoms at a distance of order 5 μm by shifting their states out of resonance, an effect known as dipole blockade. These blockade effects have only been observed in cold atom systems to the present date.

If the thermal ensemble approach is shown to be viable, it may benefit the study of interacting systems due to the shorter preparation time, quasi-continuous measurement process and reduced complexity.

Chapter 5

Thin cells for EIT

Reducing the path length of atoms interacting with the laser beams for EIT has several advantages over vapour cells several centimetres long. By focussing down the laser beams, the light intensity and thus the Rabi frequency is increased. If the interaction region is small compared to the Rayleigh range of the laser beams, the uniformity of intensity across the sample can be maximised. Of course at room temperature the optical depth of such cells will be close to negligible, but by heating the sample, the vapour pressure and thus number density of Rubidium atoms can be increased.

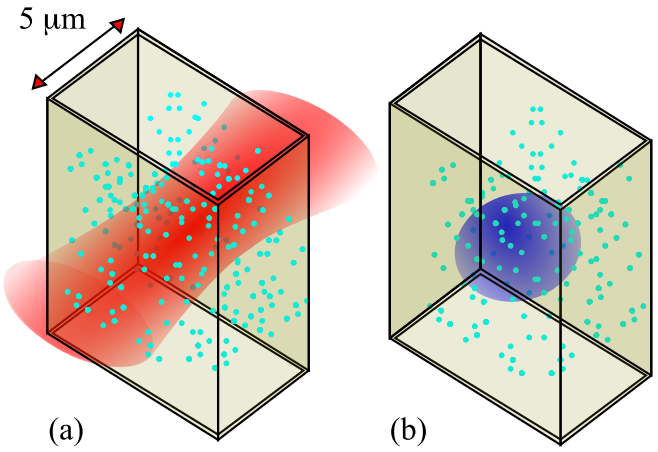

Figure 5.1: A sample of hot atoms is contained in a cell with a narrow depth of around 5 μm. In (a), a laser beam(s) resonant with the $|g\rangle \rightarrow |r\rangle$ transition is incident upon the cell. This laser beam is focussed to around the micron level. Due to dipole interactions, only one atom is excited to the Rydberg state, (b).

At higher densities the mean separation between atoms decreases, meaning that the dipolar nature of Rydberg atoms become important. In certain circumstances, of which more will be discussed later, it is only possible to excite one atom to the Rydberg state. This phenomenon is called 'dipole blockade' and the length scale over which the mechanism works is the 'blockade radius'.

The possibility of creating the atomic equivalent of a semiconductor quantum dot may be possible in thin cells. Quantum dots have been fabricated which are capable of containing just one electron [96]. The excitation of only one atom in a vapour cell to the Rydberg state could provide a controllable source of single photons, emitted as the atom decays from the Rydberg state. By focussing down the Rydberg excitation lasers to around the few micron level, as seen in figure 5.1(a), it is possible to achieve transverse confinement of the target atoms. Using a thin cell would allow longitudinal confinement. The single Rydberg atom is shown in figure 5.1(b).

Thin alkali vapour cells have perviously been used to study Λ-system in submicron cells [97], van der Waals atom-surface interactions [98] and transition self-broadening in thin cells of order 500 nm thickness [99]. To develop a model of such a blockade scheme, an understanding of the long-range interactions between Rydberg atoms is neccessary.

5.1 Dipole interactions

The interaction of two electric dipoles, d_1 and d_2, aligned on axis, separated by a distance, r can be expressed as [100],

$$V_{\text{dipole}} = \frac{d_1 d_2}{r^3}(1 - 3\cos^2\theta), \tag{5.1}$$

where θ is the angle between the dipole axis and r. If one considers an atom in a Rydberg state, due to symmetry, there is no permanent electric dipole moment. By using external electric fields it is however possible to induce a dipole moment by mixing in states of other parity. In this situation it is possible to approach the problem using this classical picture. If however the atom is in a relatively field-free environment, its influence upon other atoms is in a constant state of flux, the dipole moment fluctuates. This effect can be described by the van der Waals

interaction. Instead of the bare atomic states of the atom it is then necessary to use pair states, $|\psi_1\psi_2\rangle$. The usual procedure detailed in references [101, 102], is followed here.

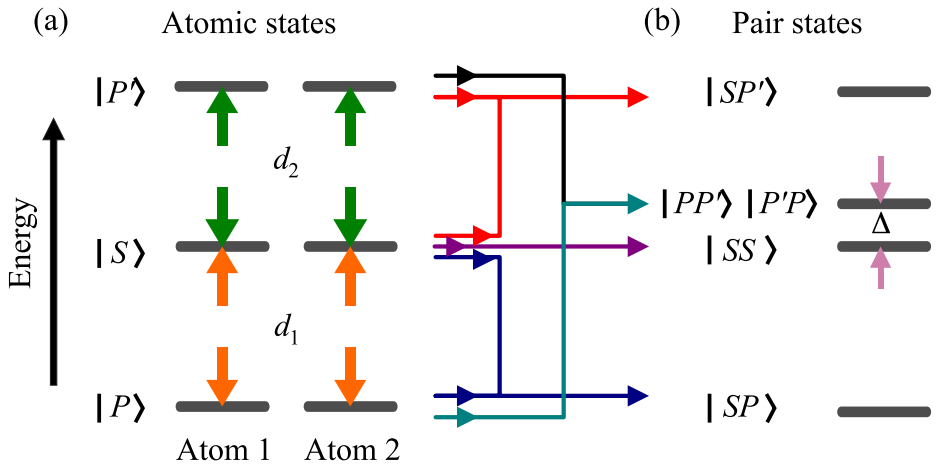

Figure 5.2: Atomic states and selected pair states for a two atom system. Dipole matrix elements d_1 and d_2 couple the $P \rightarrow S$ and $S \rightarrow P'$ states respectively. Δ is the energy difference between the states $|PP'\rangle$ and $|SS\rangle$.

$$V_{\text{dipole}} \sim \sum \langle\psi_1\psi_2| \frac{d_1 d_2}{r^3} |\psi_1'\psi_2'\rangle\,, \tag{5.2}$$

where the dipoles are assumed to lie on axis and the interaction is maximum. In this new basis, the Hamiltonian of the system is written as

$$\mathcal{H}_{\text{dipole}} = \begin{pmatrix} 0 & \frac{d_1 d_2}{r^3} \\ \frac{d_1 d_2}{r^3} & \Delta \end{pmatrix}, \tag{5.3}$$

where $\Delta = E_{PP'} - E_{SS}$ as shown in figure 5.2.

Diagonalising, the new energies of the system are found,

$$E_{\pm} = -\frac{\Delta}{2} \pm \sqrt{\left(\frac{\Delta}{2}\right)^2 + \left(\frac{d_1 d_2}{r^3}\right)^2}. \tag{5.4}$$

Two limits are formulated for the case of small or large values of Δ with respect to the size of the V_{dipole} term. Considering the case of large detunings, the interaction is a van der Waals type. The eigenenergies of which are,

$$E_{\text{vdW}} = -\frac{1}{\Delta}\frac{d_1 d_2}{r^6} = -\frac{C_6}{r^6}, \tag{5.5}$$

where $C_6 = -(d_1 d_2)^2/\Delta$. As detailed in section 4.1, the separation between states, Δ is proportional to n^{-3}, while the dipole moments scale as n^2, thus $C_6 \propto n^{11}$.

For the case of $\Delta \ll d_1 d_2/r^3$, the interaction is a resonant dipole type. In the limit that $\Delta = 0$ this can also be called a Förster resonance. In this case equation reduces to

$$E_{\text{Forster}} = \frac{d_1 d_2}{r^3} \tag{5.6}$$

$$= \frac{C_3}{r^3}. \tag{5.7}$$

As the d scales with n^2, so $C_3 \propto n^4$.

5.2 Dipole blockade

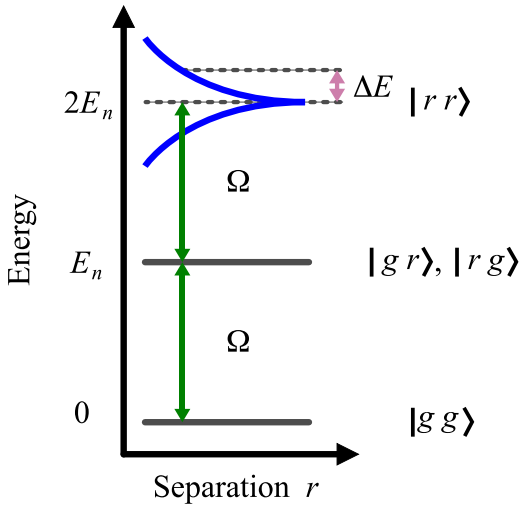

Figure 5.3: Dipole blockade due to dipole interactions. A coupling field drives the transition of an atom between the ground state, $|g\rangle$ and excited state $|r\rangle$. Here a two atom system is considered. The excitation of one atom is allowed, but an exited state containing both atoms is dependent on the dipolar interactions and thus on the separation of the two atoms.

It is possible to use both these classes of interactions to perform dipole blockade. This happens when the presence of one Rydberg atom suppresses the excitation of neighbouring atoms into Rydberg states. This is because the shift in the Rydberg energy level of a second atom moves it out of resonance with a fixed frequency

excitation laser. Figure 5.2 demonstrates this effect. Two atoms form a pair state, each atom can either remain in the ground state or be excited to the Rydberg state by a laser field with fixed frequency E_n/h. Thus there are four possible configurations, $|gg\rangle$, $|gr\rangle$, $|rg\rangle$ and $|rr\rangle$.

Starting in the state with both atoms in their ground state, one atom is promoted to the state $|\mathrm{gr}\rangle$ or $|\mathrm{rg}\rangle$, which are degenerate. There is now one atom in the Rydberg state. The energy required to promote the second atom into a Rydberg state is now different, due to the dipole-dipole interactions. As the frequency of the excitation laser has not changed, the second atom can not be excited, a blockade has occurred.

As both the van der Waals interaction and the dipole interactions are dependent on the separation of the atoms, there is a characteristic length scale corresponding to how far away this suppression occurs. This is the blockade radius and is dependent upon the laser linewidth, decay rate of the Rydberg state and Rabi frequency of the excitation laser. Each of these act to broaden the range of frequencies at which a second atom can be excited. Presuming that the laser linewidth, Γ_{ls}, is the largest of these parameters and that the interaction is a resonant dipole interaction, the condition for successful blockade is,

$$r = \sqrt[3]{\frac{C_3}{\hbar\Gamma_{ls}}}, \tag{5.8}$$

which is found by equating the interaction shift with $\hbar\Gamma_{ls}$. These blockade effects have been investigated in cold atoms [28–32, 103, 104], as well as Bose condenstates [105]. To realise dipole blockade using just two atoms, far off-resonance dipole traps have been used. In these experiments dipole blockade has been demonstrated for atoms separated by distances of 4 μm and 10 μm [39, 40].

5.2.1 Design of the multi-region cell

The multi-region cells used in this work were designed and constructed by the Institute for Physical research in Armenia in the group of Dr D. Sarkisyan. The cell used in this work, shown in figure 5.4, is similar to that described in [106], but with several distinct features. The windows added to the main body are 10 mm wide, 25 mm long and have a thickness of 2 mm. Sapphire is chosen as the window material due to its chemical resistance to hot alkali-metal vapour [107].

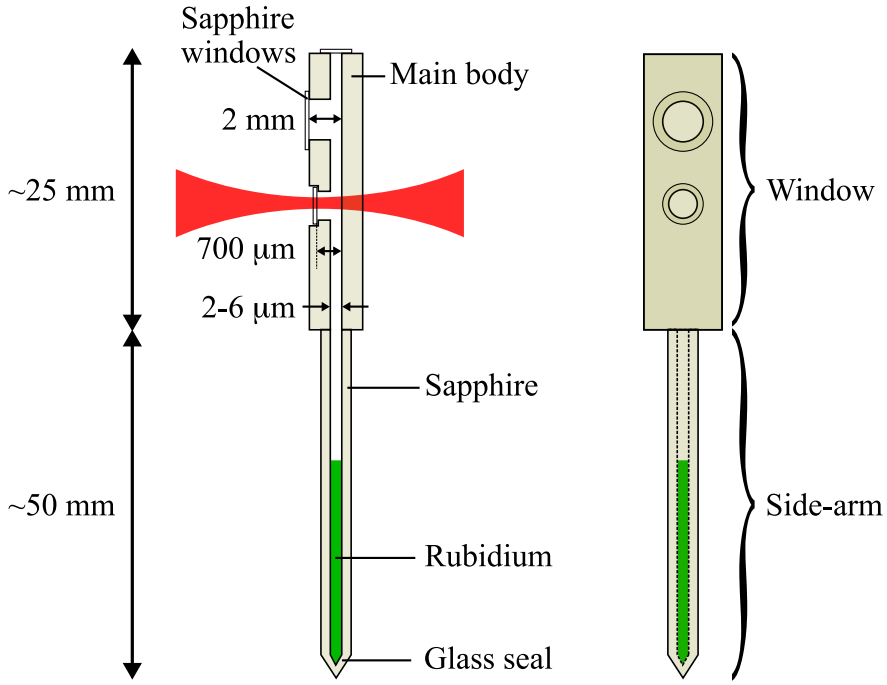

Figure 5.4: The multi-region cell. Side view (left) and front view (right). The cell has three regions of varying thickness, 2 mm, 700 µm and 2–6 µm. Two thermocouples are placed adjacent to the thin cell. The first measures the temperature of the 'window' region and the other the 'side-arm'.

The cell is constructed in such a way that three regions of varying length are created. These three regions are then able to be probed by multiple beams. The largest of these regions has an extension of 2 mm, while the others have thicknesses of 700 μm and a region of varying thickness: 2–6 μm.

To form the 2 mm thick region of the cell, a hole of radius 5 mm is drilled through one of the main body pieces. A thin piece of sapphire is then glued in place over this hole. For the 700 μm region, a slightly smaller radius hole is drilled through the main body piece. Using a larger radius another hole is drilled partly through this piece, see figure 5.4. Both these intrusions have the same centre. Another thin piece of sapphire is then placed inside the larger hole and is glued into place, the window then rests roughly half way into this recess. A Titanium strip of thickness 5 μm is inserted between the main body pieces at the bottom to form a wedged gap with variable thickness in the range 2–6 μm.
To house a Rb reservoir a tube of commercial Sapphire is inserted into a small hole drilled into the end of the main-body plates. The entire construction was assembled and glued in a vacuum furnace [108]. After the gluing, a natural mixture of the ^{85}Rb and ^{87}Rb, was added to the tube and then closed off using a glass seal.

5.2.2 Operation of the multi-region cell

To increase the number density of Rb atoms in the interaction region it is necessary to increase the temperature inside the cell. To this end, the whole assembly is placed inside an oven. To prevent the Rubidium vapour from condensing on the windows, and thus blocking any laser beams, it is necessary to have differential heating of the window region and the tube region. This is done with an oven which has separate heating elements for the volume surrounding each region. Temperature measurements are made using two thermocouples. One is kept close to the cell windows and the other is placed alongside the Sapphire tube. It is necessary to avoid contact of the thermocouple with these regions. For more details of operation, see appendix F.

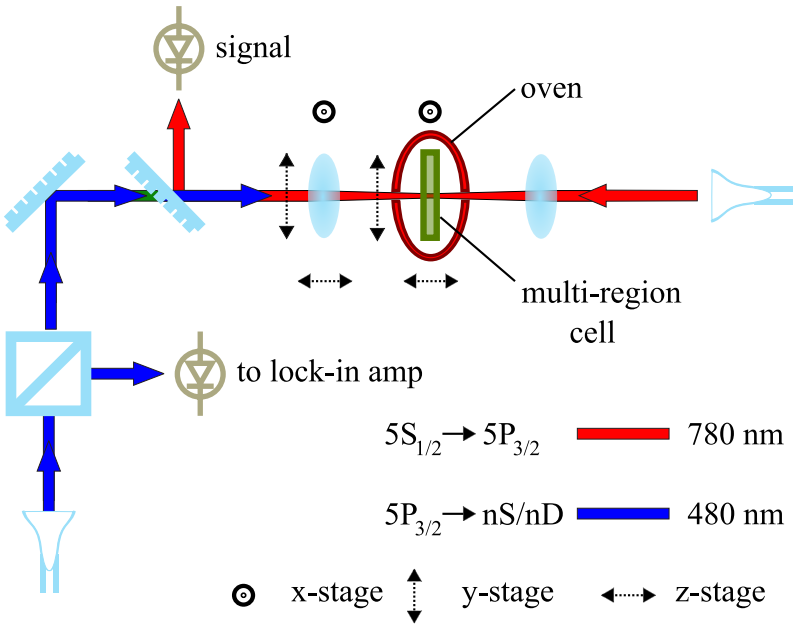

Figure 5.5: Setup for performing EIT using the multi-region cell. A portion of the blue light is split off and monitored on a photodiode. This signal can be used to generate a reference for the lock-in amplifier using amplitude modulation. The rest of the light is focussed into the multi-region cell using a $f = 5$ cm lens which is mounted on an x-y-z translation stage. The probe light counter-propagates with respect to the coupling beam and is focussed with a $f = 10$ cm lens. The multi-region cell is also mounted on an x-y-z translation stage.

5.3 Rydberg EIT in the multi-region cell

The optical set up is shown in figure 5.5. The probe beam is focussed at the centre of the multi-region cell using a $f = 10$ cm lens. The coupling beam counter-propagates through the cell. Figure 5.6(a) shows a typical EIT trace for a coupling beam resonant with the $5P_{3/2} \rightarrow 37D_{5/2}$ and a probe beam, of various powers, scanning across the D_2 line in ^{87}Rb and ^{85}Rb. The detuning is measured relative to the F = 3 $\rightarrow$ F' = 4 transition in ^{85}Rb. The two broad absorption features corresponding to the Doppler broadened spectra for the two isotopes, ^{87}Rb at large, negative detunings and ^{85}Rb around zero detuning. Imposed on this background are multiple Rydberg EIT peaks. At low probe powers, these are similar to those seen in chapter 4, however for probe powers of around 1 μW, the spectrum broadens and some shifting of these features is seen. By increasing the probe power, the number of atoms promoted to the Rydberg state also increases. With more Rydberg atoms in the thermal ensemble, the greater is the effect of the surrounding electric field. If the electric field is uniform, then the shift of each atom will be the same, consequently well defined peaks are seen. However should the electric field be more complicated the corresponding lineshape will be smeared out.

The case for the S states is shown in figure 5.6(b). Here the coupling beam is tuned to be resonant with the $39S_{1/2}$ state. Although some broadening is seen as the probe power is increased, the lineshapes of each scan are similar. To attempt to explain this broadening in more detail, a lock-in amplifier was used to measure the small signals seen in the cell. By modulating the coupling beam, the change in signal corresponding to the presence of the blue beam is isolated. This signal is then free from the Doppler background. Figure 5.7 shows such a signal produced by modulating the blue, coupling laser at 35 kHz. Again a range of probe powers are used. The transmission is normalised to the height of the largest peak and the detuning is shown relative to the F = 3 $\rightarrow$ F' = 4 in ^{85}Rb, however this time the region under investigation is the 700 μm section of the multi-region cell. The spectra show that for low probe powers, in the 200 nW region, many peaks are seen at a range of probe detunings. As the probe power is increased, so these start to merge to form three main peaks.

For clarity, a low power scan reproducing these features is shown in figure 5.8. Here the transmission is normalised so that it can be compared to the signals in

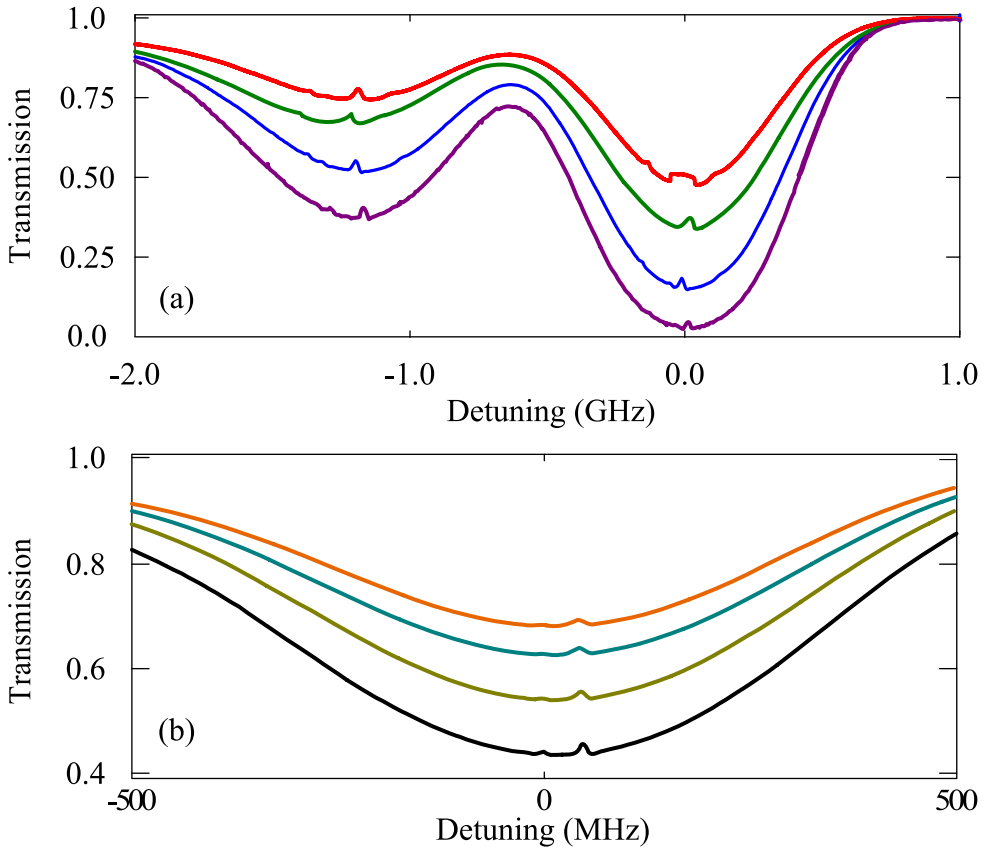

Figure 5.6: Rydberg EIT with a coupling beam resonant with the transition to 37D in the 2 mm region. Various probe beam powers are 70 nW (purple), 780 nW (blue), 2.7 μW (green) and 5.5 μW (red). In (b) the $39S_{1/2}$ state is used instead for probe powers of 100 nW, 660 nW, 1.6 μW and 2.8 μW. Beam sizes, 14 μm vertical 17 μm horizontal blue. 27 μm red vertical, 14 μm red horizontal. Probe detuning in (a) is relative to the $5S_{1/2}(F = 3) \rightarrow 5P_{3/2}(F' = 4)$ transition in ^{85}Rb and $(F = 2) \rightarrow 5P_{3/2}(F' = 2)$ transition in ^{87}Rb in (b) .

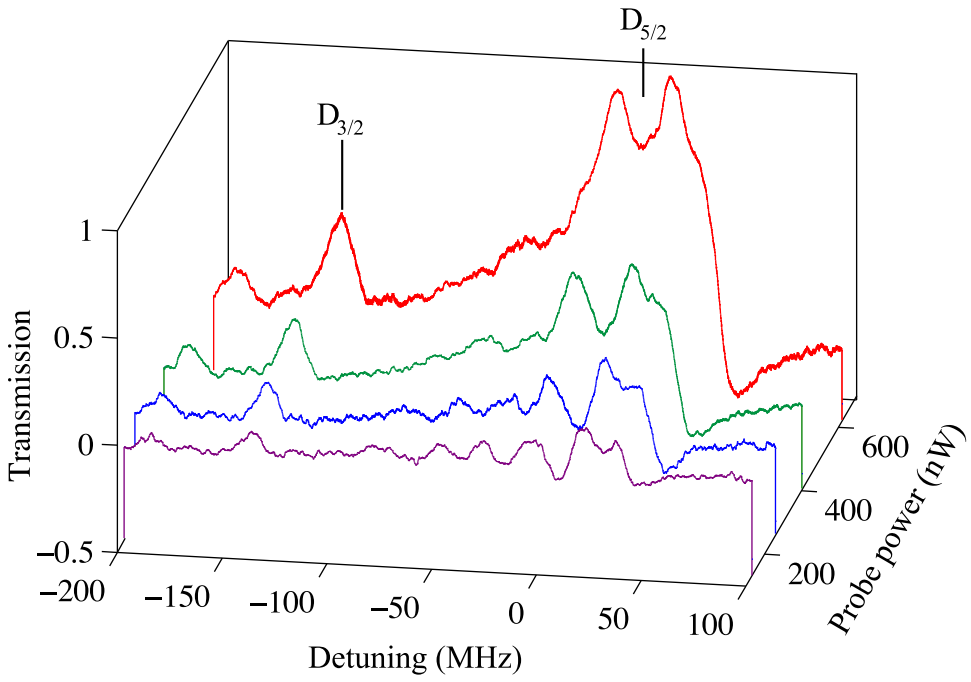

Figure 5.7: Lock-in amplifier signal for Rydberg EIT state in the 700 μm region of the cell using for various cell temperatures. Probe detuning relative to the F = 3 → F' = 4 transision in ^{85}Rb. Coupling to the 37$D_{5/2}$ Rydberg state with 12.5 mW of power after the chopper wheel. Various probe powers of 130 nW, 250 nW, 400 nW and 620 nW, purple, blue, green and red traces respectively. Constant coupling power 12.5 mW after chopper wheel. Window temperature 117 °C and side-arm temperature 52 °C. Laser beam 1/e^2 radii: blue 18 μm horizontal, 15 μm vertical and red 9 μm vertical, 7 μm horizontal.

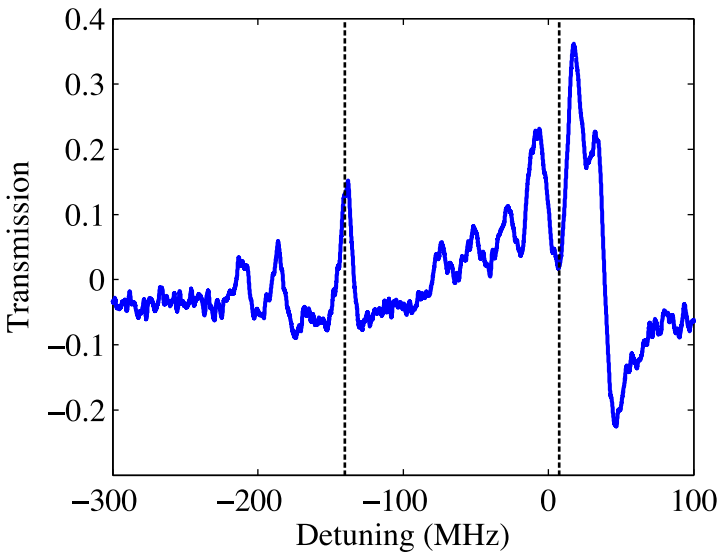

Figure 5.8: Lock-in amplifier signal showing EIT in the 700 μm region of the cell using the $37D_{5/2}$ state. Probe detuning relative to the F = 3 → F' = 4 transition in ^{85}Rb. The dotted lines correspond to the expected locations of the $D_{3/2}$ resonance (left) and the $D_{3/2}$ resonanace (right). Probe power 250 nW and coupling 12.5 mW, same y-axis calibration as figure 5.7. Window temperature 117 °C, side-arm temperature 52 °C.

figure 5.7. The peaks seen in this scan are more easily seen. The presence of multiple resonances separated by many 10s of MHz are unexpected.

Contrasting this, is the case for the 39S $_{1/2}$ state in the same cell region. The probe power dependence was similar to that already seen. Instead a range of temperatures were studied to investigate the effect of number density. This is shown in figure 5.9, with the signal normalised to the largest peak height. The signals show no effect of changing temperature other than an increase in signal size with the optimal conditions being 137 °C for the windows and 89 °C for the side-arm.

The difference in behaviour between the $S_{1/2}$ and $D_{5/2}$ states could be for a number of reasons. Firstly the fine structure seen in the D state, yielding three different m_J states, this has already been seen to complicate the electro-optic switching in section 4.4.1. The polarisability of the D states is also larger, thus for a given electric field, more shifting will be seen. The cause of this electric field is believed to be due to the presence of ions, generated by the blue light inside the cell. As the work function of Rb is 2.16 eV [109], which equates to a wavelength of around 570 nm, it is expected that photo-electrons will be produced by the 480 nm light giving rise to an electric field inside the cell. Part of the problem with studying these effects is that through repeated heating up and cooling down of the cell, different conditions are present. Most notable is that Rubidium condensing on the cell windows can give rise to different behaviour for nominally 'the same' experimental settings.

To attempt to explain the splitting of the 37D state, an electrode cell was set up. This cell, again built by the group of D. Sarkisyan contains two electrodes inside a 11 mm Rb cell. It is then possible to study the effect of a roughly uniform electric field on the Rydberg EIT spectrum. The altered setup is shown in figure 5.10, here it is possible to see lock in signals from both cells. By applying a known voltage the $D_{5/2}$ state splits.

A comparison between these two cells is shown in figure 5.11. In 5.11(a) no electric field is applied and the usual spectrum is seen. The application of a 2.4 Vcm^{-1} electric field in (b) acts to cleanly split the resonance. In figure 5.11, the low probe power signal from the 700 μm cell is reproduced. Comparing these three traces, it seems that there is no uniform electric field distribution which could account for

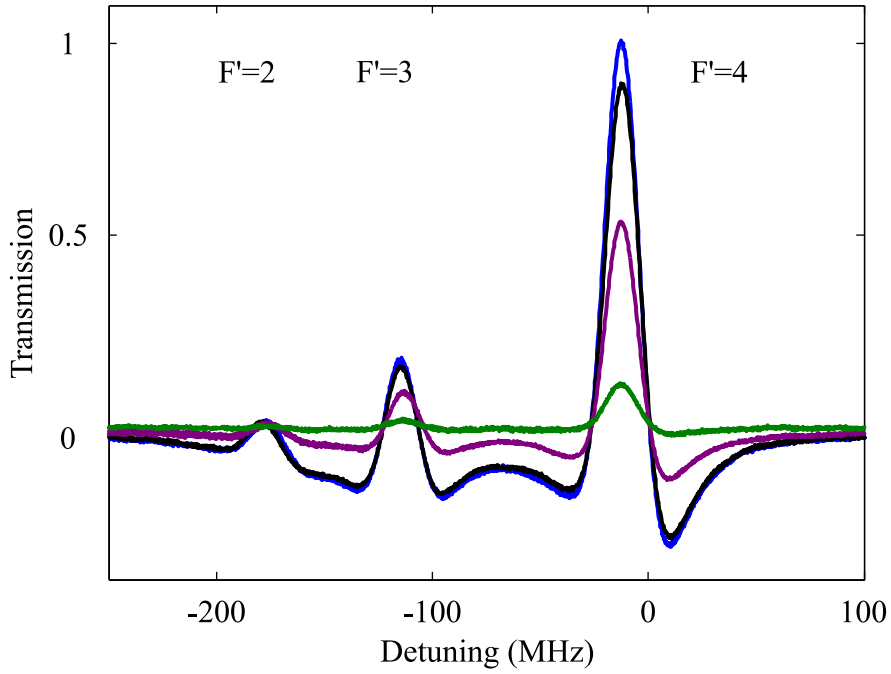

Figure 5.9: Lock-in amplifier signal for Rydberg EIT state in the 700 μm region of the cell using for various cell temperatures. Probe beam detuning relative to F=2 $\rightarrow$ F' = 3 resonance in ^{87}Rb. Coupling beam resonant with the F'=3 $\rightarrow$ $29S_{1/2}$ transition. The three peaks are due to the different intermediate states, F' = 2, 3 and 4 as shown in the diagram. Probe power is 1 μW and the coupling power measured after the chopper wheel is 16 mW . Temperatures of the windows and sidearm respectively, black, 130 °C 80 °C, blue 137 °C 89 °C, purple 141 °C, 98 °C and green 144 °C 108 °C.

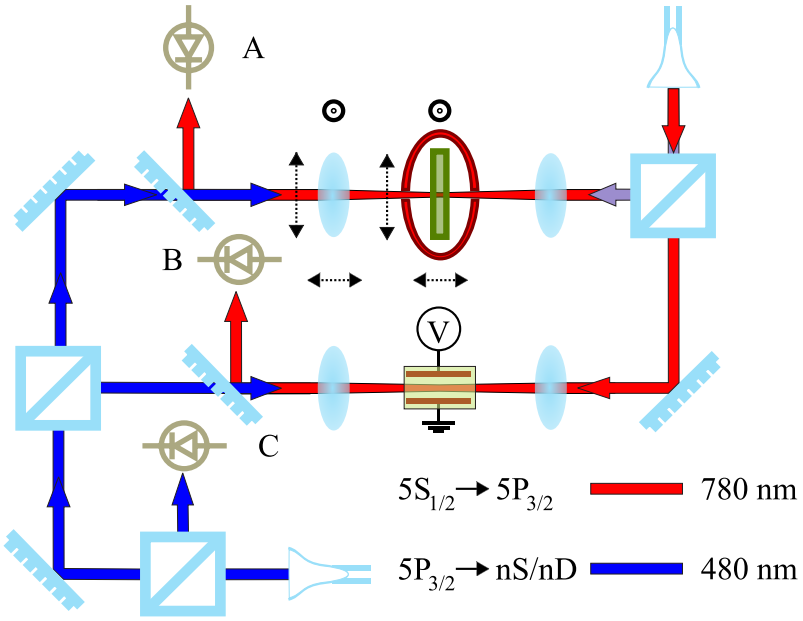

Figure 5.10: Setup for comparing the EIT signal from the multi-region cell with that of the electrode cell. As in figure 5.4 the probe and coupling beams are focussed into the multi-region cell. However in this setup, it it possible to also analyse the signal in the electrode cell; this allows a regulated dc voltage to be applied to the atoms. The light into this electrode cell is focussed into this cell using $f = 10$ cm lenses on both beams.

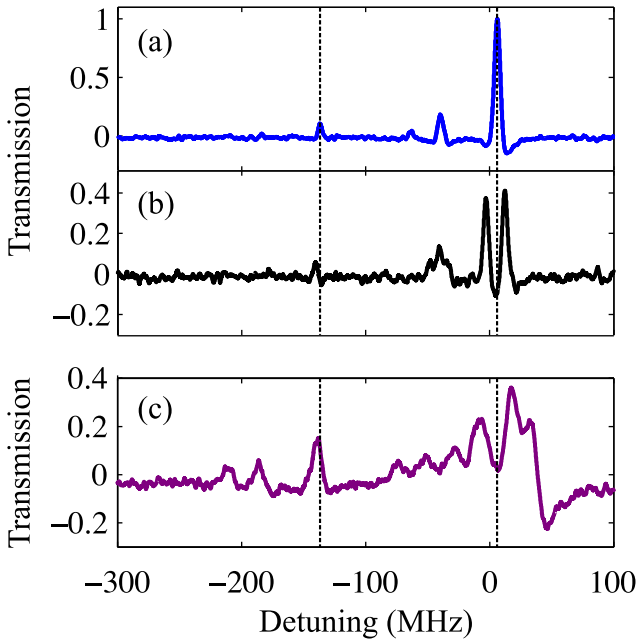

Figure 5.11: Comparison of Rydberg EIT in the electrode cell (a) and (b) and the 700 μm region of the multi-region cell (c) as a function of detuning from the F = 3 → F' = 4 resonance in ^{85}Rb. The Rydberg state used is 37D. In (a) and (b), Electric fields of 0 Vcm^{-1} and 2.4 Vcm^{-1} respectively are applied. The dotted lines correspond to the unshifted positions of the $D_{3/2}$ (left) and $D_{5/2}$ (right) resonances. The beam powers are 1.5 μW in the probe beam and 8 mW in coupling beam after the chopper wheel. While in (c) the probe power is 250 nW and coupling power 12.5 mW, same y-axis calibration as figure 5.9.

the signal in the multi-region cell. Thus the origin of the extra peaks is not clear. There is some suggestion that surface polaritons may be responsible [110]. Polaritons are coupled phonon-photon waves that can arise in crystalline structures, such as quartz [111]. These effects will have to be studied in more detail in the move towards thin cells.

5.4 Ladder EIT using the 5D state.

To confirm that it is possible to observe ladder EIT in the micron region of the multi-region cell, it was necessary to move to a state with lower principal quantum number and thus lower polarisability. The state $5D_{5/2}$ was chosen as there

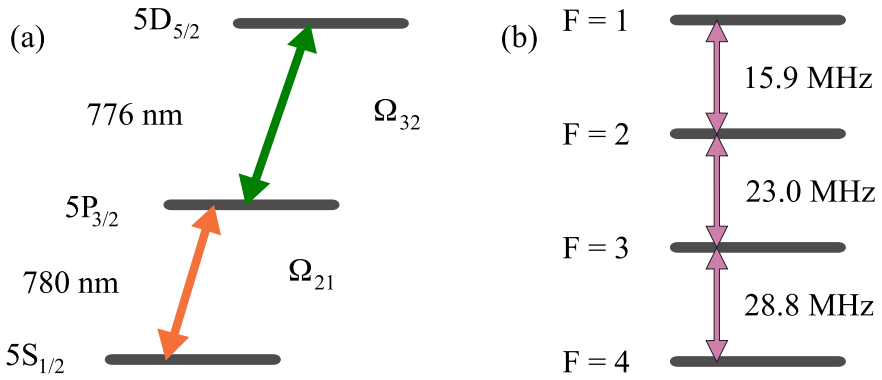

Figure 5.12: In (a) the level scheme for ladder EIT using the $5D_{5/2}$ state is shown. The hyperfine structure of ^{87}Rb is shown in (b). The frequency splittings are taken from reference [114], note that the states are inverted.

was plenty of laser power available, more than 100 mW, around its transition wavelength 776.1 nm using a Toptica DLX amplified diode laser. Much work has been published on this scheme and the hyperfine splittings are well known [112, 113]. Figure 5.12 shows both the level scheme for this work (a), and the hyperfine structure, (b).

The setup for this is very similar to that of figure 5.5, with the 776 nm coupling beam taking the place of the Rydberg coupling beam. Both the 780 nm probe beam and the coupling beam are focussed into the micron region of the multi-region cell using $f = 5$ cm lenses. A typical trace is shown in figure 5.13. The thickness is estimated as 2.5 µm. In (a) the probe beam is scanned across the D_2 resonance in ^{87}Rb and ^{85}Rb, F = 1 → F' and F = 3 → F' respectively. While in (b) the scan is centered around the F = 3 → F' = 4 transition in ^{85}Rb. Large transparency is seen in both cases, but the transparency window is very broad, with a FWHM of around 100 MHz. This is much larger than the decay rate of the state, around 660 kHz [115]. This width is primarily due to transit-time broadening, the atoms passing through the tight laser beam focus incur a broadening of the transition to around 10 MHz. This leads to the hyperfine structure not being resolved, merging the separate EIT features into one.

By detuning both the probe and coupling laser beams by the same frequency in opposite directions, it is possible to move from the EIT regime to one of 2-photon absorption Although this effect has been demonstrated before [116, 117], in figure

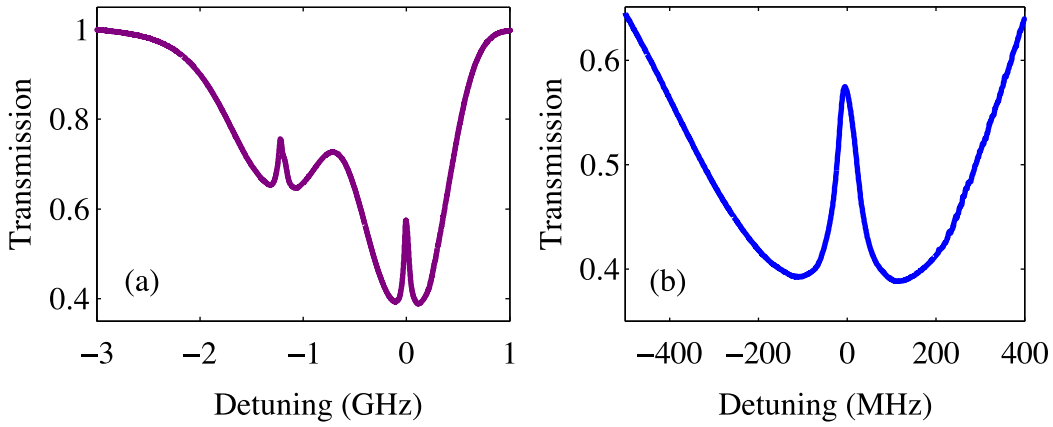

Figure 5.13: Ladder EIT in the micron cell. 56 mW coupling power in the 776 nm laser and a probe power of 1 μW. Window temperature 198 °C and side-arm temperature 135 °C. 5 cm lenses, with input beam sizes of approximately 1 mm ($1/e^2$ radius). Cell length is around 2.5 μm. Probe detuning is relative to the $5S_{1/2}$(F = 3) → $5P_{3/2}$(F' = 4) transition in ^{85}Rb.

5.14 the medium becomes optically thick on a two-photon transition. A weak probe beam detuned close to the $5S_{1/2}$→$5P_{3/2}$ resonance can be absorbed and the atoms promoted to the $5D_{5/2}$ state. Figure 5.4 shows another example of a two-photon resonance. In this case the probe beam is tuned below the $5S_{1/2}$→$5P_{3/2}$ resonance and the coupling beam above the $5P_{3/2}$→$5D_{5/2}$ resonance. At these detunings it is possible to resolve all four F states of the $5D_{5/2}$ line; a change of F=±2 is allowed. These large absorption features may be useful in optical filtering of certain probe laser frequencies. The narrow resonances would allow precise control over the wavelength of filtered light and thus fine control over the wavelength of filtered light.

5.5 On-going work

5.5.1 3 stage excitation scheme

If it is the case that the photo-electric effect is responsible for the broadenings and splittings seen in these thin cells, then one possible solution would be to use a three-stage excitation scheme. If each of these stages has a transition energy lower

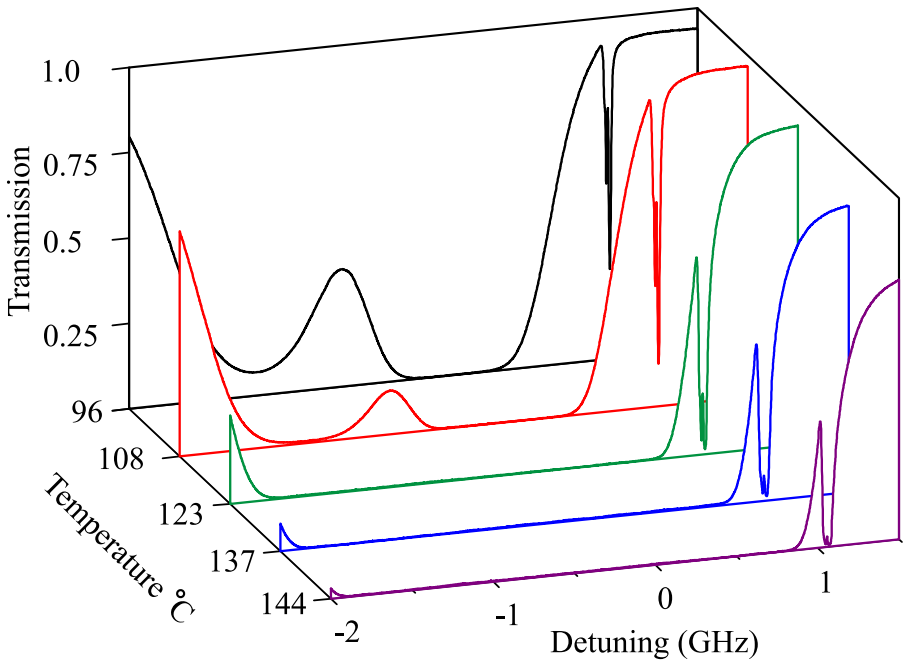

Figure 5.14: The probe absorption spectra for different temperatures in the vicinity of the $5S_{1/2}$(F = 2) $\rightarrow$ $5P_{3/2}$(F') and $5S^2S_{1/2}$(F = 3) $\rightarrow$ $5P_{3/2}$(F′) in in ^{87}Rb and ^{85}Rb, respectively. A counter-propagating coupling beam is detuned of order 1 GHz to the red of the $5S_{1/2}$(F = 3) $\rightarrow$ $5P_{3/2}$(F') resonance giving rise to a 2–photon absorption resonance at a detuning of 1 GHz. For the highest temperatures the cell becomes optically thick on the 5S-5P-5D transition. Temperatures of the side-arm. 5 cm lenses, probe power of 5 μW and coupling power 53 mW. Both beams are focussed using f = 5 cm lenses with beam waists of around 1 mm before the lenses.

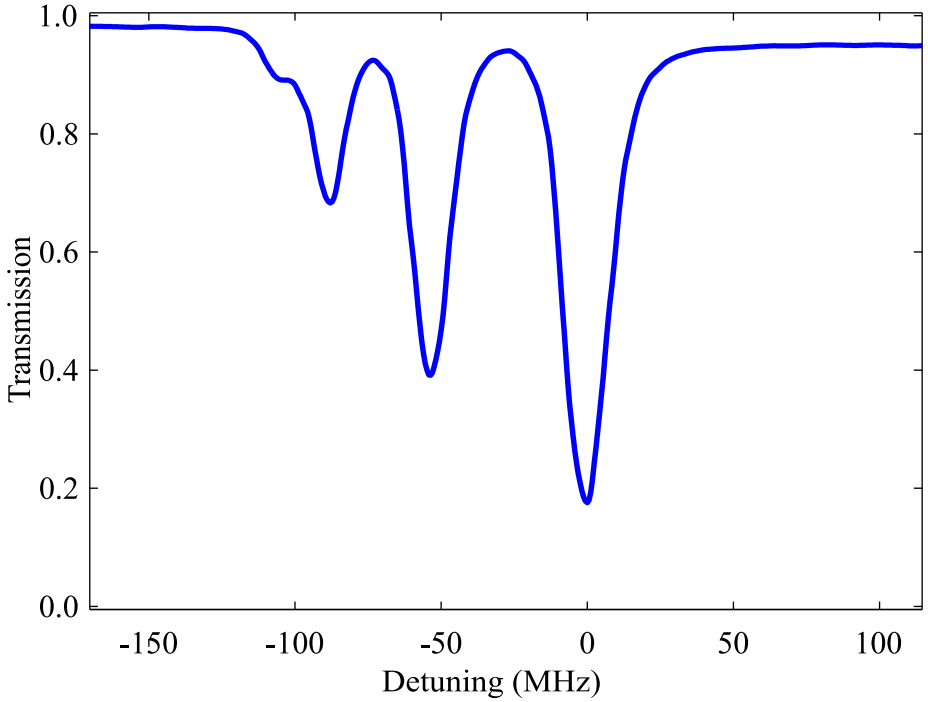

Figure 5.15: A 2-photon absorptive resonance shows that the hyperfine structure of the 5d $^2D_{5/2}$ in ^{85}Rb is clearly resolved. All four F states are present, as a change in F of ±2 is allowed for a two-photon transition. The relative depths are due to optical pumping.

than the work function of Rubidium, then no photo-electrons would be generated. As detailed in section 5.3 this means that longer wavelengths than 570 nm must be used. A possible 'route' to the Rydberg state is shown in figure 5.16. The shortest

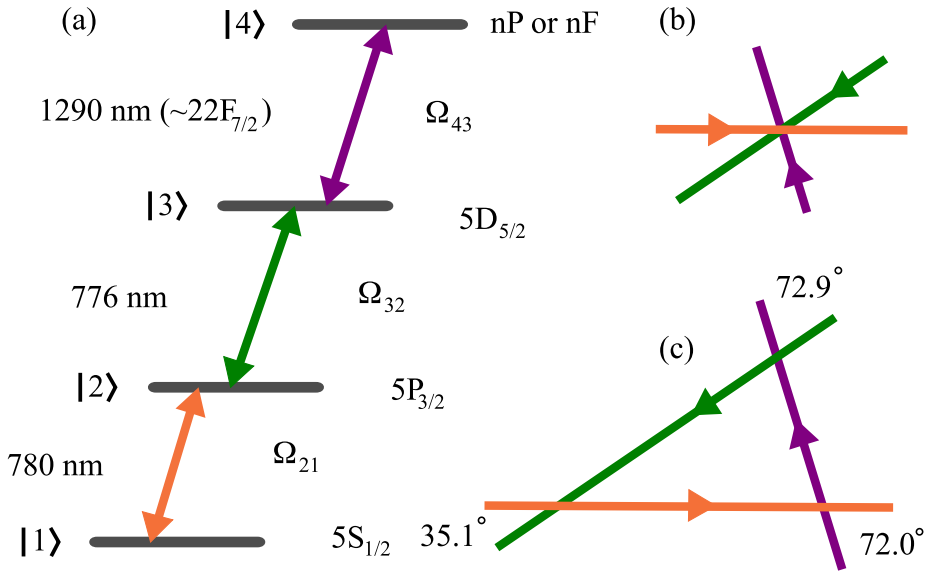

Figure 5.16: The level scheme for 3-stage excitation to the Rydberg state is shown in (a). With judicious choice of beam propagation directions, (b), it is possible to achieve a Doppler free resonance. These angles are shown in (c), where the wavevectors of each beam sum to zero.

wavelength is 776 nm, thus any photo-electron generation would be a two photon process and thus unlikely. In this configuration, it would be possible to access $P_{1/2}$, $P_{3/2}$, $F_{5/2}$ and $F_{7/2}$ states.

One added bonus of this scheme would be the possibility of a Doppler-free configuration of beams. This is depicted in figure 5.16(b) and (c). The angles at which the beams are incident up on the cell are set so that the wavevectors sum to zero, so that the Doppler shift experienced by an atom in one beam is compensated for by the other two beams. With beam radii of around 1 mm the resulting 'interaction zone' formed by the beam overlap will be small, this prohibits the study in conventional $\sim$ 10 cm cells. Thin cells do not suffer from this problem.

Using a design based on that detailed in reference [118], an extended cavity diode laser at 1290 nm has been built. This design uses a diode (QLD-1300-20S) pro-

duced by QPhotonics and diffraction grating with 750 grooves/mm (Photonics and Analytical Marketing, 33025FL01-175H). This should be capable of exciting the 21 and 22 F state in Rubidium. Rydberg excitation to $P_{3/2}$ states via the $5D_{5/2}$ state has recently been demonstrated using a diode laser at 1256 nm [59, 119].

5.5.2 Rydberg detection via ground state depletion

Figure 5.17 shows the effect of pumping atoms to the Rydberg state by using a strong probe beam. In 5.17(a) the coupling beam counter-propagates to the probe beam, while a small fraction of this coupling beam is reflected from the the cell window and thus co-propagates with the probe beam. Because of this an extra peak is seen in the spectrum, which is circled in (a). By retro-reflecting the coupling beam with a dichroic mirror it is possible to recreate this setup in the 2 mm region of the multi-region cell. Figure 5.17(b) shows the relative height of this feature as a function of probe power in the 2 mm cell. The larger width belies the fact that the peak is not generated by an EIT process. Using the Faraday effect may help probe this feature. Thus it is possible to use ground-state depletion to detect Rydberg states. A similar scheme is used in references [58, 59], where it is called 'shelving'.

5.6 Outlook

One way of analysing this depletion could be to exploit the Faraday effect. This effect describes the rotation of the polarisation of light through a medium subject to an external magnetic field and has been studied extensively in atomic systems [120]. The combination of this effect and that of slow light has potential for probing the thermal atoms in these vapour cells [121, 122]. Unlike the EIT systems considered so far, which involve three levels, the slow light Faraday effect, demonstrated in reference [121], relies upon detuning the a probe laser field far from a Doppler-broadened absorptive resonance. At large detunings, greater than the Doppler width, the bandwidth of rotation is around 1 GHz; for a large range of detunings, the phase variation is small. Due to these large detunings, the absorption is low, typically around the few percent level.

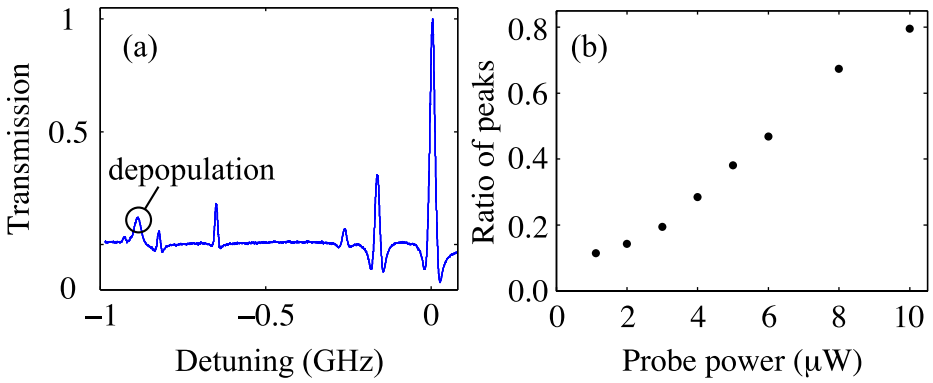

Figure 5.17: In (a) a typical EIT spectrum is supplemented by an extra absorptive resonance due to the population being promoted into the Rydberg state, circled in the figure. In (b) the ratio of the depopulation peak to that of the height of the largest $D_{5/2}$ peak is plotted. This is for the 2 mm cell, window temperature, 83 °C 35 °C side-arm temperature. The coupling beam is tuned to the 27D state and has a power of 100 mW power.

By measuring the polarisation using a balanced polarimeter, the fast dynamics of Rydberg states could be probed. As this technique has high bandwidth, this could possibly allow the use of pulsed lasers, with greater powers and thus higher Rabi frequencies possible. As seen in figure 5.13, with enough laser power, it is possible to observe large EIT in the micron cell region.

Even though rapid dynamics may best be studied using the Faraday effect, Rydberg EIT still has a role to play in enabling control of a medium's dispersive properties. As shall be shown in the next chapter, the interplay between thermal ensembles, Rydberg EIT and electric fields offer a novel way to manipulate light.

Chapter 6

Giant Electro-Optic Effect

In chapter 4 it was shown that the polarisable nature of Rydberg states can be mapped onto a ground state coherence. This chapter will again focus on the effect of electric fields on the dynamics of Rydberg EIT; in particular the extent to which the refractive index of the atomic vapour medium is sensitive to external electric fields.

A convenient measure of the propensity of a medium to change its refractive index, Δn_r, under the influence of an electric field is the Kerr coefficient [123] as defined in

$$\Delta n_r = \lambda B_0 \mathcal{E}_0^2 \,, \tag{6.1}$$

where λ is the wavelength of the probe laser field, $\mathcal{E}_0$ is the applied electric field and B_0 is the electro-optic Kerr coefficient.

The Kerr effect has been used in optics: namely in electro-optic modulators as seen in chapter 2. Its application to short pulse production using ultra-fast lasers extends to Kerr lens mode-locking [124], which uses the ac Kerr effect. The practicality of applying this effect to other problems is often limited by its relatively weak nature. To enhance the effect, the laser frequency must be tuned closer to resonance and thus this increases the dispersion. This increase has the drawback of increasing the amount of absorption. EIT offers a way around this, in that absorption can be low while the change in refractive index can be substantial. Enhanced ac Kerr non-linearities in EIT systems have been predicted [43, 125], as well as observed in experiments on Bose-Einstein condensates [14] and cold atoms [126].

Ideally the non-linearity would be large enough so that even on the single-photon level a large phase change could occur. If this phase change could be made as large as π, then this would allow the implementation of a photonic phase gate, one possible choice candidate for quantum computing [127]. Unfortunately, the non-linearity neccessary for such a task has been shown to be larger than that possible using EIT [42]. This, combined with problems of pulse distortion effects [44], means an alternative to the ac Kerr procedure is needed.

A possible solution to this problem may come from using Rydberg EIT. Instead of using the ac Kerr effect, i.e. relying upon the electric field of a control photon to perturb the phase of a signal photon, a highly excited Rydberg state could be used instead. The exact procedure has yet to be laid down, but in order to stimulate such work, the first step is to quantify the size of the Kerr coefficient in the thermal vapour cell using Rydberg EIT.

6.1 Comparison of Kerr coefficients

To estimate the size of the expected Kerr coefficient, the change in refractive index of a medium for a signal laser frequency (ω_s) is considered.

$$\Delta n_r = (\partial n_r/\partial\omega_s)\Delta\omega_s \,, \tag{6.2}$$

where $\partial n_r/\partial\omega_s = (n_g - 1)/\omega_s$ and n_g is the group refractive index. The Rydberg energy level is shifted in energy by application of an electric field, $\mathcal{E}$, via the stark shift $\Delta E = 1/2\alpha\mathcal{E}^2$, where α is the polarisability of the Rydberg state. Thus the change in refractive index of the medium is

$$\Delta n_r = \frac{(n_g - 1)\lambda}{hc}\frac{\alpha\mathcal{E}^2}{2} \,, \tag{6.3}$$

which leads to an expression for the Kerr coefficient,

$$B_0 = \frac{(n_g - 1)\alpha}{2hc} \,. \tag{6.4}$$

Using $\Delta n_r = \chi^{(3)}\mathcal{E}^2$, where $\chi^{(3)}$ is the third order susceptibility [61], gives

$$\chi^{(3)} = B_0\lambda \,. \tag{6.5}$$

For these experiments the group refractive index is of order 1–10, leading to a Kerr coefficient of order 10^{-6} m/V^2, a million times larger than standard materials, (see table 6.1).

Medium	B_0 ($\times 10^{-18}$ m/V^2)
Gas (CO_2, 1 atm.) [128]	10^0
Water [129]	10^2
Glass [129]	10^4
Nitrobenzene [129]	10^6
Rydberg dark states (this experiment)	$> 10^{12}$

Table 6.1: Kerr coefficient, B_0, for various media.

6.2 Kerr coefficient measurement

As each Rydberg state has a different sensitivity to electric fields, the Kerr constant will be dependent on the principal quantum number, n. To evaluate the Kerr coefficient in the thermal cell, the change in phase is measured for different applied voltages and various Rydberg states. A Jamin interferometer is used for this purpose and is shown in figure 6.1. The probe beam, resonant with the $5S_{1/2} \rightarrow 5P_{3/2}$

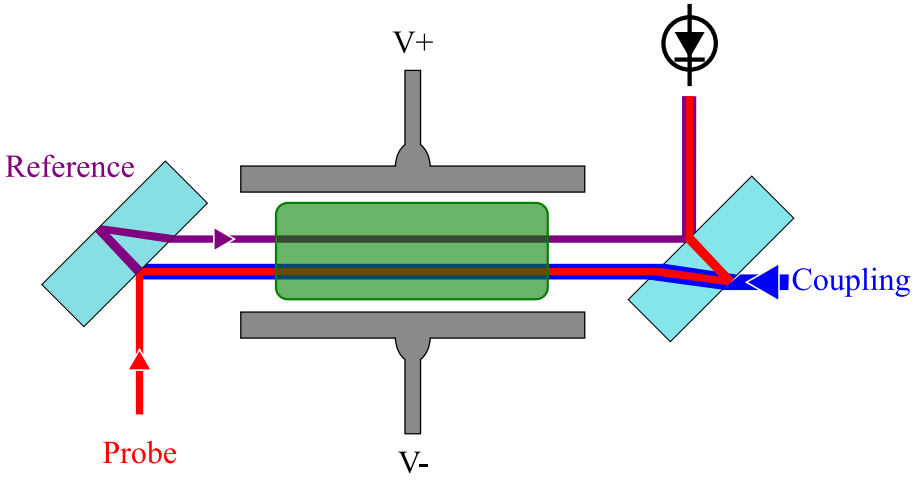

Figure 6.1: Schematic setup used to measure the Kerr coefficient of the Rydberg ensemble. A probe beam is split into two using a glass plate, and both beams propagate through the Rb cell. A coupling beam is overlapped with one of these probe beams. The two probe beams are then focussed onto a photodiode.

transition, is split using a glass plate. The two beams then propagate through the cell. Overlapping with one of these probe beams is a coupling beam resonant with the $5P_{3/2} \rightarrow nS_{1/2}$ transition, with n varying from 28–48. The two probe beams are

then combined and focussed onto a photodiode.

Using this setup, two types of experiment can be performed. The first involves monitoring the transmission through the medium when both beams are on resonance; just as in many sections of this thesis. To do this the reference beam must be blocked. The added feature of this experiment is the application of an ac voltage to the electrodes outside the cell. As the Rydberg state is highly sensitive to the electric field, this has the effect of varying the energy of the $nS_{1/2}$ state, and thus the detuning of the coupling beam. The second experiment makes use of the interference of the two probe beams, producing a signal sensitive to the change in phase caused by Rydberg EIT around resonances.

As it is not possible to apply a dc electric field because of charge screening in the cell, to illustrate this point, the coupling laser is scanned around resonance with the $28S_{1/2}$ state. This is akin to what would be seen if the Rydberg state could be 'scanned' using the dc stark shift and the control beam kept locked. The resulting change in transmission and refractive index are shown in figure 6.2. To calibrate the change in transmission it is first necessary to measure the phase difference between the probe and reference beams. By altering the path of the reference beam, the resulting interference can be monitored on the photodiode. Moving from constructive to destructive interference, the maximum and minimum voltages are recorded. The change in phase, $\Delta\Phi$ induced by Rydberg EIT can then be calibrated. This phase change to a change in refractive index, Δn_r using equation 6.6.

$$\Delta\Phi = \frac{2\pi\ell\Delta n_r}{\lambda} \,. \tag{6.6}$$

The changes in refractive index and transmission are concomitant; the existence of one necessarily means that the other is also present. The transmission of the probe beam is around 50% while the change in transmission, ΔT. is about 2%.

Now, considering the effect of an ac electric field with frequency ω_m, figure 6.3 shows how the response manifests itself in both the transmission and phase observables. In this figure, the coupling laser is fixed in frequency and the associated lineshapes are Stark shifted. Note that, as the Stark shift is proportional to $\mathcal{E}^2$, the shift can only be in one direction. Due to the EIT absorption spectrum, modulation at the 4^{th} harmonic of the driving field is expected. In the case of the phase, the modulation is at the 2^{nd} harmonic. Both these results assume that the electric

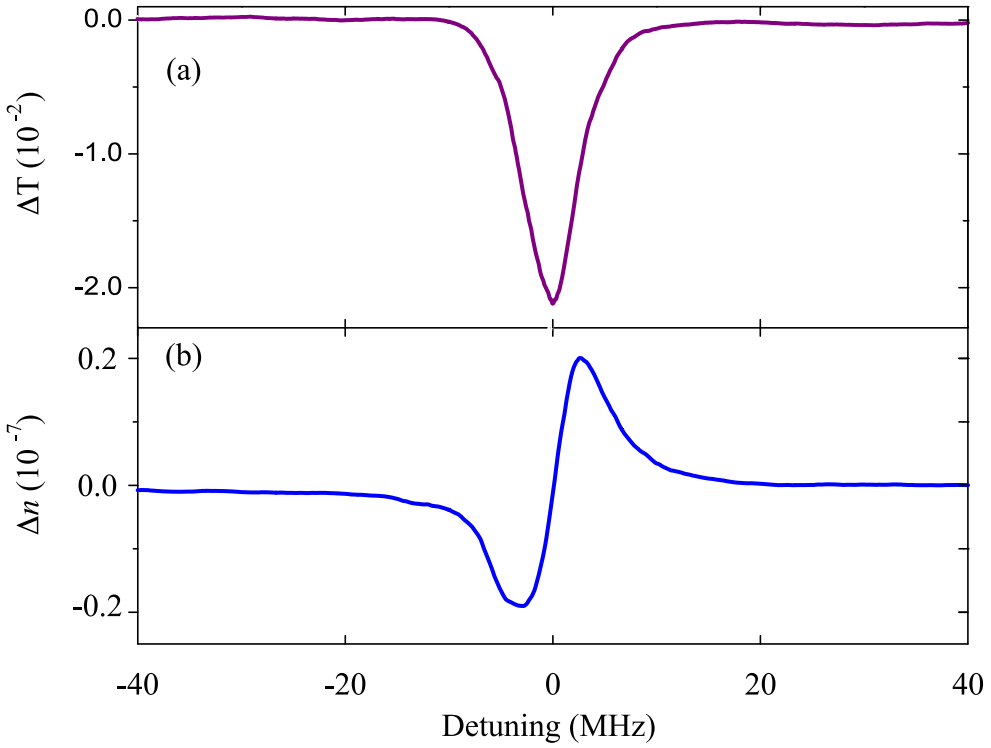

Figure 6.2: Change in transmission and phase through the vapour cell. In (a) the transmission through a cell is monitored as a function of coupling beam detuning from the $28S_{1/2}$ state in Rubidium. In (b) the change in refractive index is shown, as measured using the Jamin interferometer shown in figure 6.1.

field is weak enough that the Rydberg state is shifted by less than the width of the resonance. This dependence is experimentally verified in figure 6.4; in this case an ac electric field of 10 kHz is applied to the ensemble. This results in a change in transmission and phase, shown in (b) and (c) respectively. Power spectra of these two traces are shown in (d) and (e), indicating that the amplitude modulation is predominantly at the 4^{th} harmonic, and phase modulation is around the 2^{nd} harmonic. The presence of other harmonics in the spectrum is due to the slightly non-linear response in the phase modulation case, and the departure from a quadratic form in the transmission case.

This phase shift is both dependent on the applied electric field and the Rydberg state used. Therefore, to find the maximum phase shift possible using each Rydberg state, the shift was measured as a function of the applied electric field $\mathcal{E}_0$. To find a fit for this dependence, it is assumed that the EIT resonance has a Lorentzian lineshape, and therefore that the phase shift has the form, $\Delta\Phi = A\mathcal{E}_0^2/(1 + B\mathcal{E}_0^4)$. The maximum phase shift is calculated using the free parameters A and B which are determined from the fit. These data and the associated fit are shown in figure 6.5. Note that the largest phase shift is achieved using the lowest energy Rydberg state, $n = 28$. This is because there is limited coupling laser power available: the highest Rabi frequency thus corresponds to the lowest state. To see this more clearly it is necessary to make use of the scaling relationships associated with different Rydberg states.

6.2.1 Kerr coefficient dependence on n

As a simple model of this system, only the contributions from stationary atoms are considered. Thus, ignoring the Doppler effect, the complex susceptibility, χ, of the medium is given by:

$$\chi = \frac{2N|\mathbf{d_{21}}|^2}{\hbar\epsilon_0} \frac{1/2}{\gamma_{21} - i\Delta_p + \dfrac{\Omega_c^2/4}{\gamma_{31} - i(\Delta_p + \Delta_c)}}, \tag{6.7}$$

where $\mathbf{d_{21}}$ is the dipole matrix element and N the number density of atoms. This is just the solution of the optical Bloch equations, as discussed in section 4.1. As these experiments are done using a probe laser locked onto its respective transi-

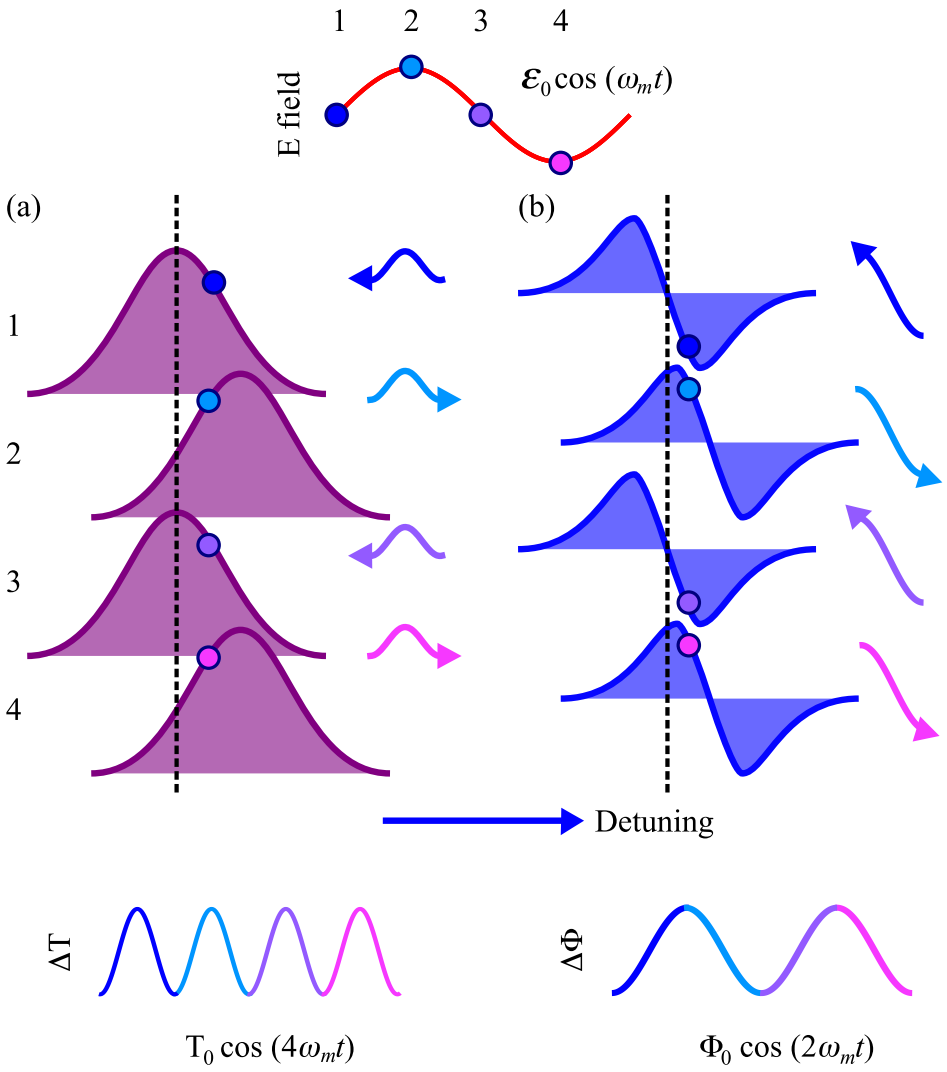

Figure 6.3: In this experiment two different types of measurements were made. The first, shown in (a), corresponds to the change in transmission through the medium. The electric field oscillates at a frequency ω_m, and the resulting transmission is at the 4^{th} harmonic of the driving field. The second measurement, of the phase, is shown in (b); in this case the change is seen at the 2^{nd} of the driving field.

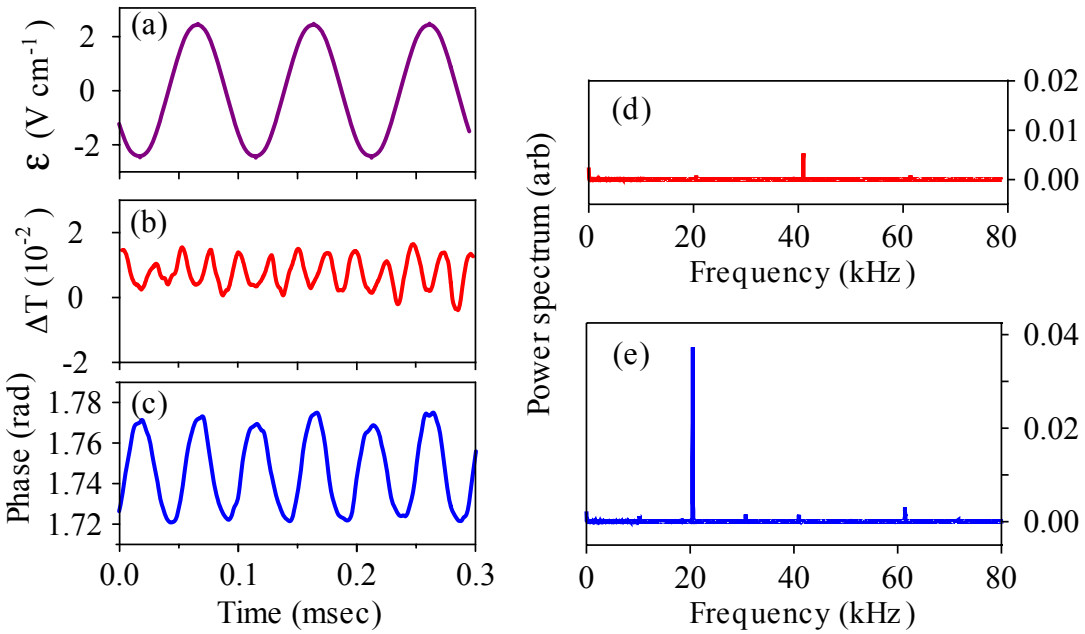

Figure 6.4: The ac electric field modulation is shown in (a). This results in modulations with transmission and phase, shown in (b) and (c) respectively. The power spectrum of these two signals is displayed in (d) and (e). The transmission modulation is seen at the 4^{th} harmonic of the driving field, while the phase modulation is at the 2^{nd} harmonic. These data was taken by A. K. Mohapatra and B. Bütscher and the plot is adapted from C. S. Adams.

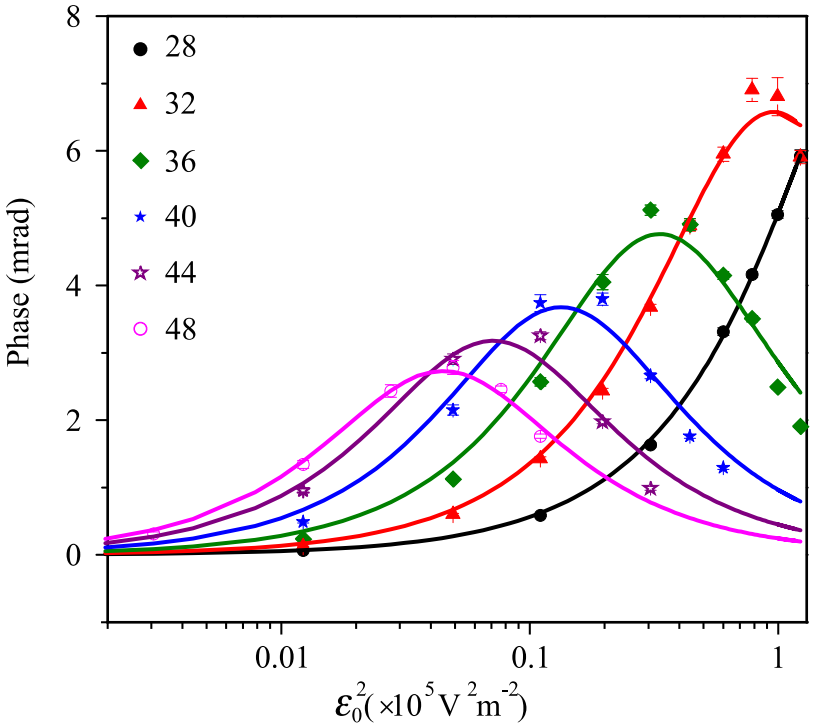

Figure 6.5: Kerr coefficient measurement. Phase shift as a function of applied electric field. Each data point corresponds to the mean value of 50 measurements, with the error bars showing the standard deviation of those measurements. The solid lines are a fit, used to find the maximum phase change possible in the medium. The 6 different $S_{1/2}$ states, n=28–48 are plotted are shown in the legend.

tion, $\Delta_p = 0$, thus

$$\chi = \frac{N|\mathbf{d_{21}}|^2}{\hbar\epsilon_0} \frac{1}{\gamma_{21} + \dfrac{\Omega_c^2/4}{\gamma_{31} - i\Delta_c}} . \tag{6.8}$$

Differentiating χ, the gradient of the slope at $\Delta_c = 0$ is

$$\left.\frac{\partial\chi}{\partial\Delta_c}\right|_{\Delta_c=0} = \frac{N|\mathbf{d_{21}}|^2}{\hbar\epsilon_0} \frac{4\Omega^2}{16\gamma_{21}^2\gamma_{31}^2 + 8\gamma_{21}\gamma_{31}\Omega_c^2 + \Omega_c^4} . \tag{6.9}$$

Using the Einstein A coefficient relation

$$\gamma_{12} = \frac{|\mathbf{d_{21}}|^2}{3\pi\epsilon_0\hbar\lambda^3} , \tag{6.10}$$

where λ is the wavelength of the probe laser beam, this can be rewritten as,

$$\left.\frac{\partial\chi}{\partial\Delta_c}\right|_{\Delta_c=0} = 3\pi\lambda^3\gamma_{21}N \frac{4\Omega^2}{16\gamma_{21}^2\gamma_{31}^2 + 8\gamma_{21}\gamma_{31}\Omega_c^2 + \Omega_c^4} . \tag{6.11}$$

This slope is then multiplied by the stark shift due to the electric field,

$$\Delta\omega_c = -\frac{1}{2\hbar}\alpha\mathcal{E}^2 , \tag{6.12}$$

to give the change in refractive index,

$$\Delta n_r = -\frac{3\pi N\lambda^3\gamma_{21}}{2\hbar} \frac{4\Omega_c^2\alpha}{16\bar{\gamma}^4 + 8\bar{\gamma}^2\Omega_c^2 + \Omega_c^4}\mathcal{E}^2 , \tag{6.13}$$

where $\bar{\gamma}^2 = \gamma_{21}\gamma_{31}$. This function peaks at $\Omega_c^2 = 4\bar{\gamma}$; for this experiment the coupling Rabi frequency is less than 1 MHz; thus with greater laser powers, an increase in phase modulation would be seen.

For a thermal ensemble, the residual Doppler averaging due to wavelength mismatch of the signal and coupling laser leads to an EIT peak of order 3 MHz [50]. This broadening can be included in the decoherence term $\bar{\gamma}$. As $\Omega_c \ll \bar{\gamma}$ the Ω_c^4 term can be neglected and the Kerr constant written as

$$B_0 = \frac{3\pi N\lambda_0^2\gamma_s}{16\hbar\bar{\gamma}^4} \frac{\alpha\Omega_c^2}{(1 + \Omega_c^2/2\bar{\gamma}^2)} . \tag{6.14}$$

As discussed in section 4.1, the polarizability, α, is proportional to n^{*7} and Ω_c scales as $n^{*-3/2}$ for constant laser power. Thus, the n^*-dependence of the Kerr coefficient is given by a function of the form

$$B_0 = \frac{c_1 n^{*4}}{(1 + c_2 n^{*-3})} , \tag{6.15}$$

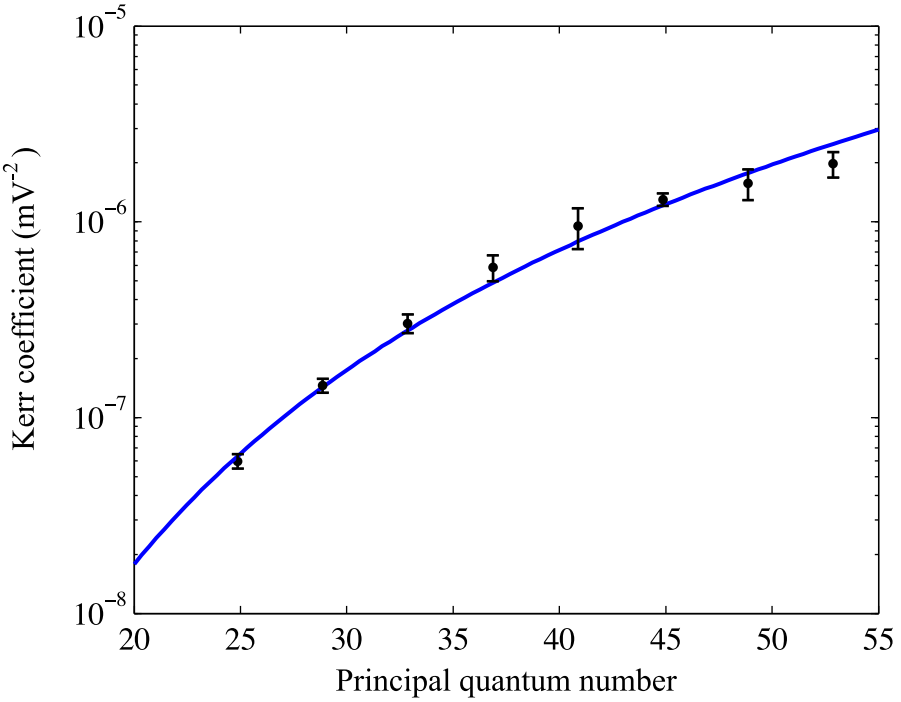

Figure 6.6: Kerr coefficient measurement for Rydberg states with different reduced principal quantum numbers. The blue line is obtained by fitting equation 6.15 using two free parameters and reflects the fact that the data was taken at constant coupling power.

where c_1 determines the absolute magnitude and c_2 determines the n^* dependent scaling. These constants are used as free parameters for fitting the experimental data in figure 6.6. The measured Kerr coefficient for different principal quantum numbers, n, between 28 and 48, based on the fit from figure 6.5, are presented in figure 6.6. Here the phase shift is converted into a value for the Kerr constant using equations 6.1 and 6.6.

$$\Delta\Phi = 2\pi B_0 l |\mathcal{E}_{max}|^2 \,, \tag{6.16}$$

where $l = 7.5$ cm is the length of the cell and $\mathcal{E}_{max}$ is the electric field at which the maximum phase shift is measured. The fit in figure 6.6 reproduces the expected dependence upon principal quantum number. Beyond this agreement, it is difficult to use this model as a way of predicting Kerr coefficients based on the experimental parameters. One problem is that the model neglects the contributions from off-resonant velocity classes, while the electric field inside the cell is not precisely known, due to charge screening by the ions created by the 480 nm laser. These problems may also account for the fact that the measured Kerr constant for $28S_{1/2}$ is roughly an order of magnitude less than that predicted by equation 6.4: 6×10^{-7} m/V^2. This is motivation to move towards a 'cleaner' solution, such as the three-stage excitation scheme in section 5.5.

6.3 Electro-optic modulation

It has already been shown that phase modulation can be used to generate light at different frequencies. This was the basis of the Raman beam production outlined in chapter 2, and formally shown in appendix C. By applying an ac electric field to the ensemble of atoms, using this electro optic effect, probe light develops sidebands at harmonics of the modulation frequency. A convenient way of measuring this effect is by performing a heterodyne measurement on the probe beam [130]. A schematic of this is shown in figure 6.7. This method has an advantage over measuring the spectrum in a Fabry Perot etalon, in that an intense reference beam can be used to achieve an output with good signal to noise ratio. To be able to dectect the presence of sidebands in the probe beam frequency spectrum, it was neccessary to heat the vapour cell up to 60 °C. At this temperature the atomic number density, N, is larger and greater phase modulation is possible;

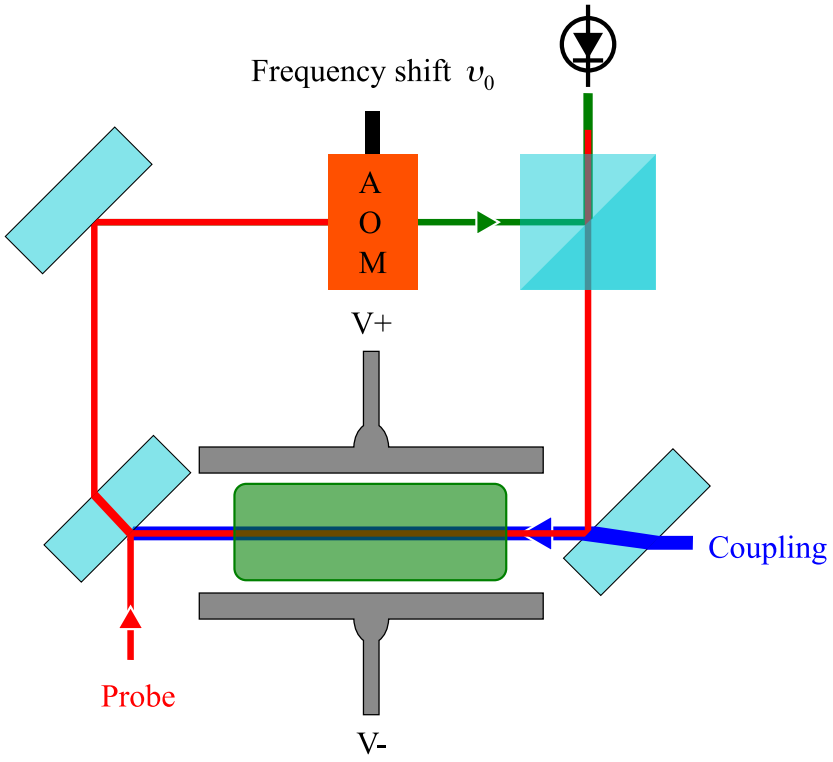

Figure 6.7: Experimental setup used to study sideband generation. A probe laser is split into two parts using a non-polarising beam splitter (NPBS); one part propagates through the Rubidium cell, overlapping with a counter-propagating pump beam. The second probe beam is frequency shifted using an acousto-optic modulator (AOM). These beams are then combined and focussed onto a fast photodiode, which is fed into a spectrum analyser.

this is seen in equation 6.13. The resulting phase modulation is roughly 60 times larger than at room temperature. There is also some increase in peak height, so an increase in amplitude modulation may be expected; however this is only a factor of two greater, thus phase modulation is the dominant mechanism. To achieve this higher temperature, a cell incorporating two copper bars either side of the cell is placed inside a magnetic shield. This cell was built by Richard Abel.

The probe beam, resonant with the $5^2S_{1/2}(F = 3) \rightarrow 5^2P_{3/2}(F' = 4)$ transition in ^{85}Rb, is split into two using a non-polarising beam splitter (NPBS). One part of this beam propagates through the vapour cell. Counter-propagating to the probe beam is the 480 nm coupling beam locked to the $5P_{3/2}(F' = 4) \rightarrow n^2S_{1/2}(F'')$ transition using an EIT signal in another cell. The probe beams have a power of 15 μW and a waist of 1 mm ($1/e^2$ radius), while the coupling beam has a power of 140 mW with a waist of 0.8 mm ($1/e^2$ radius) . The second portion acts as a reference, its frequency shifted by $\nu_0 = 400$ MHz using an acousto-optic modulator (AOM). This beam has a waist of 1 mm ($1/e^2$ radius) and power of 1 mW. After combining these two beams in the NPBS, the beams are focussed onto a fast photodiode, EOT ET-2030A. The total electric field incident on the photodiode is,

$$\mathcal{E}_{\text{total}} = \mathcal{E}(\nu + \nu_0) + \mathcal{E}(\nu) \exp\left(\frac{i2\pi n_r(\nu)\nu t}{c}\right), \tag{6.17}$$

with the light intensity being $\mathcal{E}^2_{\text{total}}$. The output signal of the photodiode is analysed using a Stanford SR 830 DSP spectrum analyser. The presence of the frequency dependent refractive index, $n_r(\nu)$, in equation 6.17, demonstrates that the phase of the probe beam passing through the cell is dependent on its frequency.

The beating of the probe and reference laser gives rise to a single beat note when no coupling beam is present, as seen in figure 6.8. In the presence of the coupling laser, sidebands appear at twice the modulation frequency. In agreement with figure 6.4, the 2$^{\text{nd}}$ order has the largest sideband. The sidebands are largest at lowest modulation frequency, with an intensity of $\sim 1\%$ of the carrier for an applied voltage of 2.4 V/cm. The roll-off of these sidebands, i.e. the sideband amplitude as a function of modulation frequency, is shown in figure 6.9.

This roll-off gives the modulation bandwidth, its width set by the transient response of the EIT resonance. As the coupling Rabi frequency is less than the decay

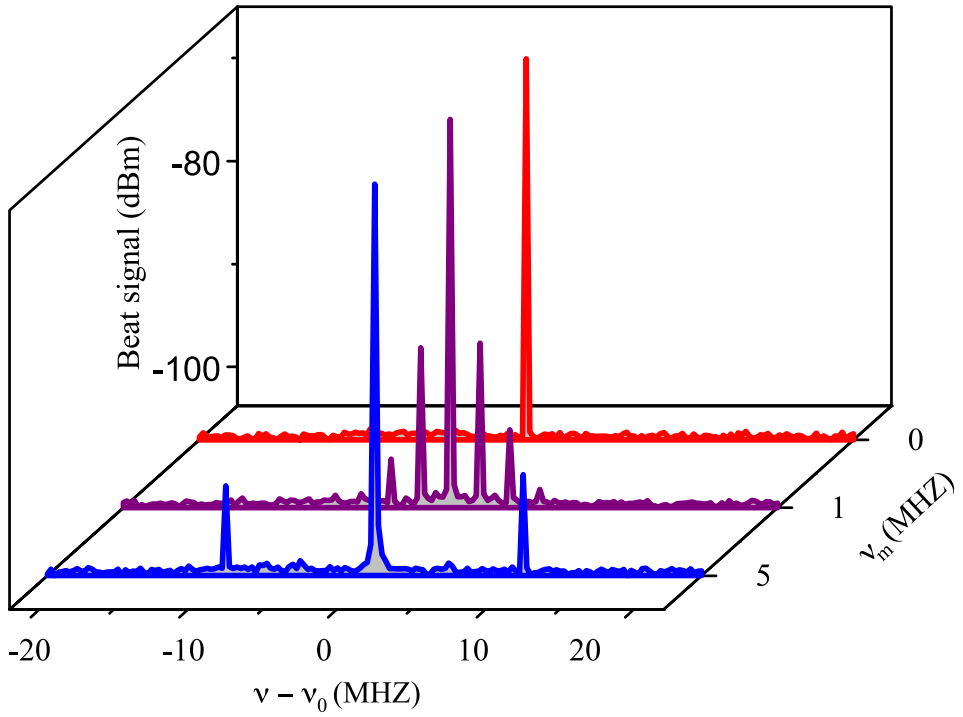

Figure 6.8: Power spectrum of the probe beam transmitted through the vapour cell. The red trace shows the beat note of the probe and reference laser in the presence of no coupling laser. In purple and blue are the traces corresponding to an applied ac electric field of 2.4 Vcm^{-1} at frequencies, ν_0, of 1 MHz and 5 MHz respectively. This voltage was chosen as it is the optimum for phase modulation using the state $n = 32\mathrm{S}$.

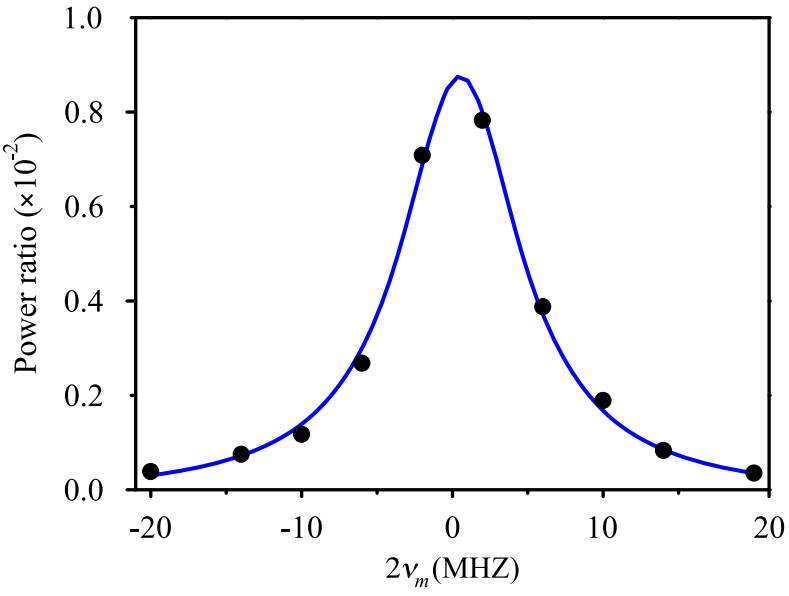

Figure 6.9: Ratio of the height of the second order peaks to the carrier peak for various modulation frequencies, ν_m. The blue line is a Lorenztian fit to the points with FWHM of around 10 MHz.

rate of the intermediate state, γ_s, the response time is set at $\tau \sim 1/(2\pi \times 6\ \mathrm{M}Hz)$, the natural linewidth of the $5P_{3/2}$ state [131, 132]. The Lorentzian fit to the experimental data, shown in figure 6.9, has a full width half maximum of 10 MHz, larger than the 6 MHz expected. This is attributed to the pressure broadening from the background gas, as seen using Doppler-free spectroscopy.

6.3.1 Dependence on coupling laser lock

This technique of phase modulation using Rydberg states is reliant upon the ability to create coherence between the ground state and Rydberg state. Central to this is the relative linewidth of the probe and coupling lasers. The blue laser lock benefits from feedback to the current control and this helps narrow the laser linewidth. When turning this feature off, broadening is expected in the frequency spectrum. The beating of the probe and reference laser should mean a δ-function is measured. If frequency fluctuations create a significant phase shift, this gives rise to amplitude noise, as expressed in equation 6.17. Such noise can be seen in figure 6.10, when increasing the linewidth of the coupling laser. This effect is most prevalent at lower frequencies, around the 0^{th} order peak. This may prove a useful

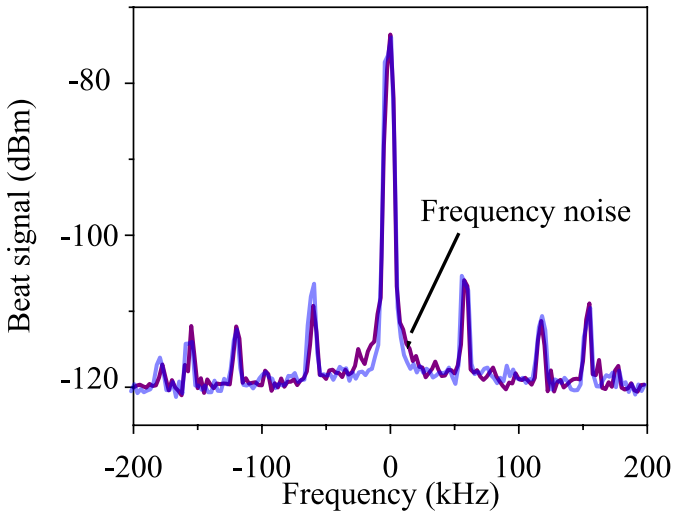

Figure 6.10: Power spectrum showing broader frequency features in the presence of no current feedback, purple, and with feedback, translucent blue. The sidebands at harmonics of 62 kHz are suspected to be due to electric field noise.

tool in future phase modulation experiments, acting as a quick way of diagnosing laser lock performance due to the quasi-continuous measurement process.

6.4 Future work

Although generation of light at different frequencies is a useful tool, the limited bandwidth and experimental overheads are drawbacks for creating a practical device. Instead it might be possible to perform electrometry with such a device. Measuring electric fields in free space is a subject of significant research, with the highest performing devices being solid state [133, 134]. A vapour cell electrometer would benefit from the continuous nature of the EIT measurement as well as the non-destructive element of the process. The device would function by reading out the change in phase of a probe beam due to charges in the cell, or even other Rydberg atoms. The latter may be adapted to quantum information studies; entangling single photons by detecting other Rydberg atoms [45].

To increase the depth of phase modulation, and hence the sensitivity a number of steps could be taken, the most obvious being to increase the Rabi frequency of the coupling laser. Another way would be to increase the group refractive index, using narrower resonances. Much larger group refractive indices are possible in lambda

systems [14] but not presently in ladder systems. Work towards this is ongoing; Rydberg EIT in cold atoms has been shown to produce sub-MHz linewidths [56]. Of course, using states with higher polarisability is also a possibility, as long as enough laser power is available. The scaling of polarisability with n^{*7} means that this approach could prove to be the most productive.

Detecting phase modulation due to electric fields is just one possible route to electrometry. Combining knowledge of the response of Rydberg states to an electric field and the dynamics of EIT could allow electrometry to be performed using only the change in transmission of the medium; this is the subject of the next chapter.

Chapter 7

Phase modulated Rydberg states

Phase modulation has been a recurrent theme throughout this work, but this chapter takes a slightly different approach. Instead of considering the effect of phase modulation on a probe beam, the perturbation to the Rydberg state by phase modulation is considered. In studies involving Rydberg states, microwave fields have been used to dress the Rydberg states [135]. This gives rise to sidebands at harmonics of the modulation frequency. As these fields are usually greater than 1 GHz in frequency the resulting sidebands are well separated from the state.

Radio frequency (rf) dressing of Rydberg states has also been studied [136] with the purpose of measuring the scalar and tensor polarisability of the $65p^2P$ state in Sodium. Field ionisation was used as the detection mechanism in this experiment.

At rf frequencies of around 10 MHz, it is possible to observe sidebands in the EIT spectra. The observation of these sidebands and their dependence on the electric field are the subject of this chapter.

7.1 Effect of dc fields on the Rydberg EIT spectrum

Before discussing the effect of ac fields on the Rydberg spectrum, it is useful to first investigate the dc effects. Using the electrode cell mentioned in section 5.3, it is possible to apply ac and dc electric fields in the same direction. By placing the electrodes inside the vapour cell, it is possible to circumvent the problem of charge screening. The electrons and ions inside the cell are lost at the electrodes.

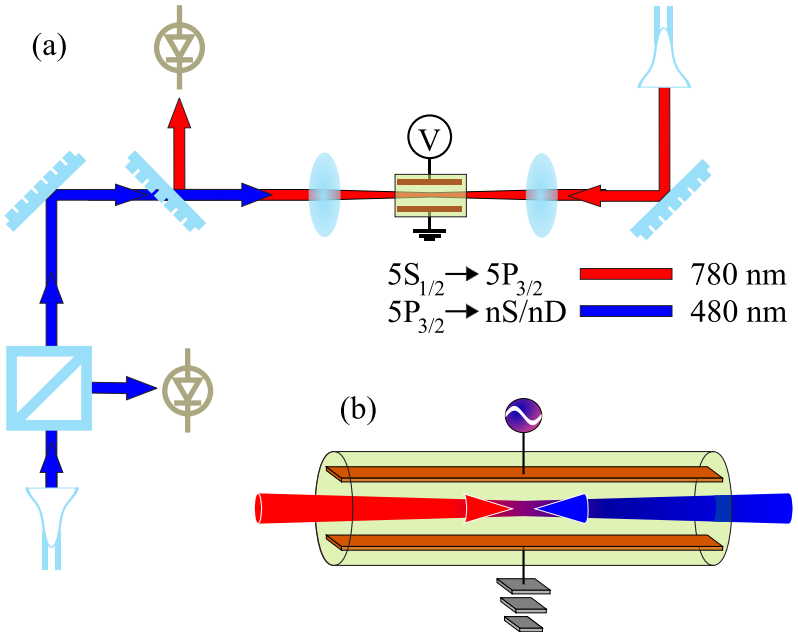

Figure 7.1: In (a) a schematic of the experimental setup is shown. The probe and coupling beam counter-propagate through the electrode cell containing parallel plane electrodes with a separation of around 5 mm. The length of the Rb vapour cell is 1.1 cm. An ac voltage with variable dc offset, or dc voltage, can be applied to the plates to produce the electric field.

Thus it is possible to apply dc fields and observe the resultant Stark shift.

The setup for performing Stark spectroscopy is shown in figure 7.1. The coupling beam is split using a polarising beam splitter cube. One of these beams is collected on a photodiode and used as a reference signal for the lock-in amplifier. The other coupling beam propagates through the 1.1 cm electrode cell, where it is overlapped with the co-axial probe beam propagating in the opposite direction. To achieve higher Rabi frequencies both of these beams are focussed using $f = 10$ cm lenses with input radii ($1/e^2$) of 1.7 mm for the probe beam and 1.0 mm for the coupling beam.

As an example of this, the Stark spitting around the D state is studied. Such splitting is usually represented using a Stark map, in figure 7.2 this splitting is seen as a function of probe laser detuning. The 37D state splits into three different peaks, corresponding to the $|m_J|$=5/2, 3/2 and 1/2 projections. The effect is most easily seen in the largest peak on the right of the figure. The $|m_J|$=5/2 peak moves rapidly to negative detunings as it has the largest polarisability, while $|m_J|$=3/2| also shifts to lower frequencies. However the $|m_J|$=1/2 projection moves to higher detunings as seen on the right of figure 7.2.

A similar measurement can be made using the $32S_{1/2}$ state. This state is simpler to use and, although it has a smaller polarisability, there is no splitting with electric field, only shifting. Figure 7.3 shows the electric field dependence on the peak of the EIT feature. The shift follows the dc stark shift: equation 4.11. The polarisablity of this state was taken from reference [137], which gives an empirical equation for S state polarisabilities in rubidium:

$$\alpha = \alpha_a n^{*6} + \alpha_b n^{*7} \tag{7.1}$$

where $\alpha_a = 2.202(28)\times10^{-9}$ MHz/(V/cm)^2 and $\alpha_b = 5.53(13)\times10^{-11}$ MHz/(V/cm)^2 are fitting parameters. For the $32S_{1/2}$ state this gives $\alpha = 2.198(38)$. Using the separation of the plates as a free parameter, the measurement gives a distance of 0.511 ± 0.002 cm, which compares favourably with the separation of 5 mm specified when the cell was supplied.

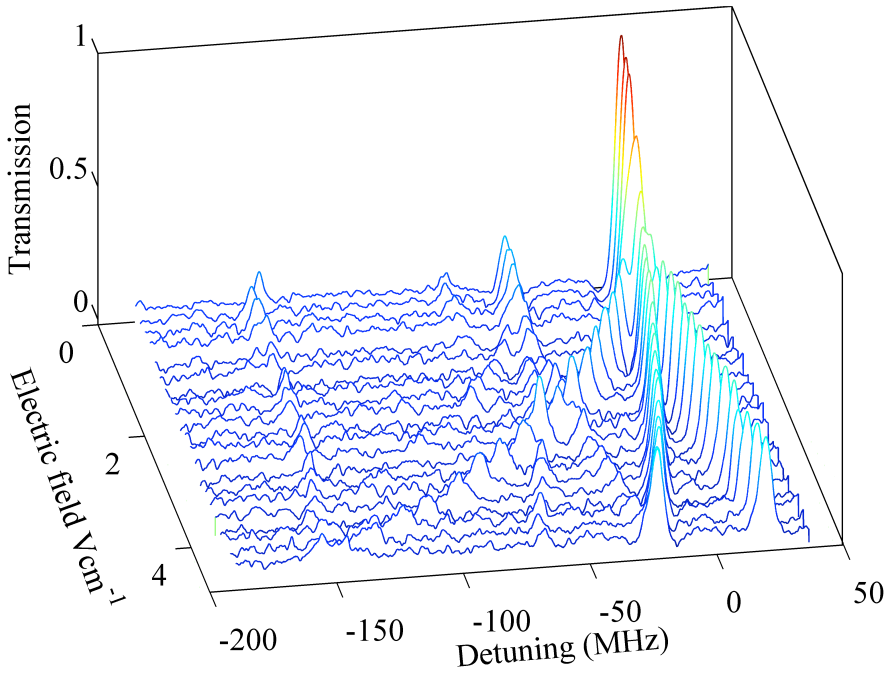

Figure 7.2: Measured electric field dependence of the $37D_{5/2}$ state. Various electric field strengths are applied, and the dc Stark effect splits the EIT resonances into different m_J components. The different peaks are due to the contributions from the separate intermediate states as seen in chapter 5.

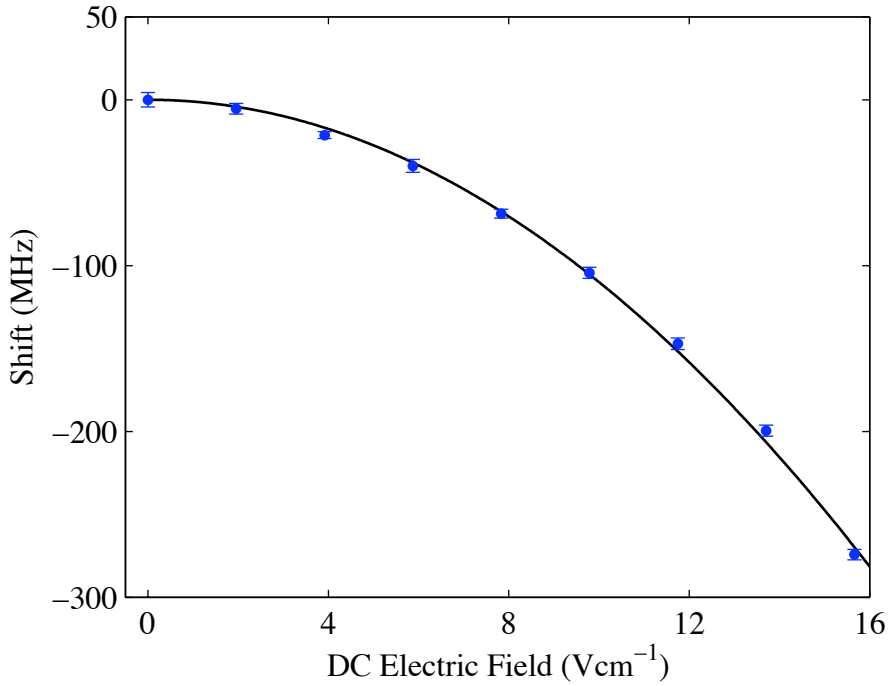

Figure 7.3: Stark shift of the $32S_{1/2}$ state as a function of applied dc electric field. The solid line gives the theoretical fit using the plate separation as a free parameter.

7.2 Effect of ac fields on the Rydberg EIT spectrum

The case of the ac Stark shift is also of interest, and provides another way of measuring the plate separation. Usually the ac Stark shift is encountered when dealing with optical dipole traps [138]. An intense laser, usually red-detuned from an atomic transition, is used to provide a conservative potential, within which laser cooled atoms are trapped. In this case the frequency of the ac field is that of the laser light.

Instead it is possible to apply a voltage directly and observe the ac Stark shift. This shift is shown in figure 7.4; here a voltage at 15 MHz with various electric field strengths is used to shift the Rydberg EIT feature. This frequency is much less than all the relevant optical frequencies of the system. The corresponding peak locations are plotted, with the solid line being the least squares fit, again using the plate separation, d as a free parameter. By fitting to the equation

$$\Delta E = \frac{\alpha}{4}\left(\frac{V_0}{d}\right)^2 , \tag{7.2}$$

a separation of $d = 0.513 \pm 0.003$ cm is achieved. The factor of 4 in the denominator comes from the ac Stark shift. This is in good agreement with the dc measurement.

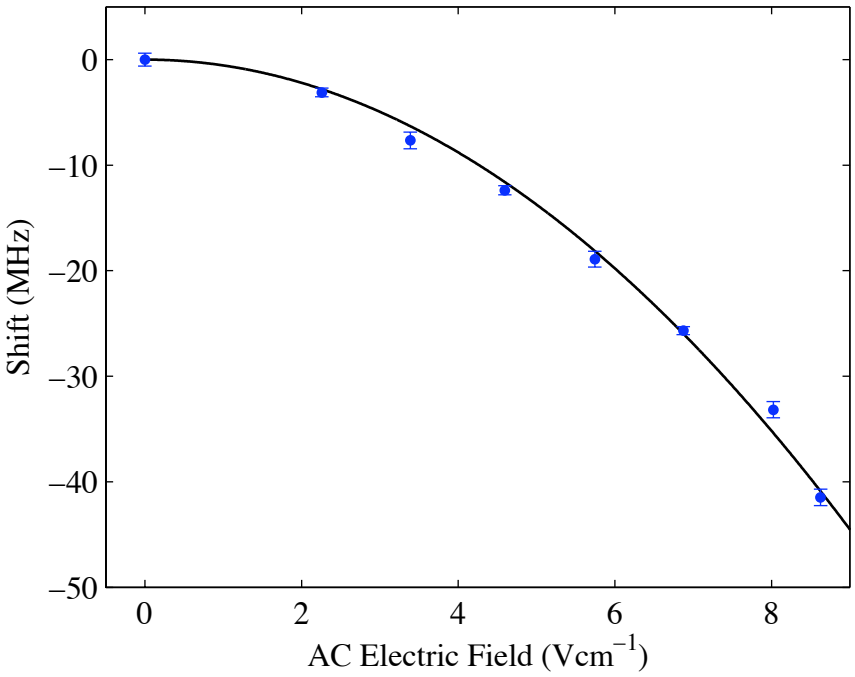

Figure 7.4: Stark shift of the $32S_{1/2}$ state as a function of applied ac electric field. The solid line gives the theoretical fit using the plate separation as a free parameter.

Interestingly, the shift in the spectrum is accompanied by sidebands in the EIT transmission spectrum. The presence of these peaks motivates a close look at the electric field modulation of Rydberg states.

7.3 Phase modulated Rydberg states

The treatment of phase modulation using the stark effect is simply treated in reference [139]. For a more rigourous explanation, including the addition of the dc field, reference [136] is more useful. Both these approaches neglect the perturbation to the state vector; for the purpose of describing this experiment such an approximation is permissible.

In general the electric field applied to the atoms can be written as,

$$\mathcal{E}(t) = \mathcal{E}_{\rm dc} + \mathcal{E}_{\rm ac} \sin \omega_m t \ , \tag{7.3}$$

where $\mathcal{E}_{\rm dc}$ and $\mathcal{E}_{\rm ac}$ are the applied dc and ac electric fields, with ω_m being the frequency of the applied electric field. The instantaneous state energy, E, is the sum of the unperturbed energy $E^{(0)}$ and the shift in energy due to the Stark shift,

$$E(t) = E^{(0)} - \frac{1}{2}\alpha\mathcal{E}(t)^2 \ . \tag{7.4}$$

Hence, using equation 7.3,

$$\begin{aligned} \mathcal{E}^2(t) &= \mathcal{E}_{\rm dc}^2 + 2\mathcal{E}_{\rm dc}\mathcal{E}_{\rm ac} \sin \omega_m t + \mathcal{E}_{\rm ac}^2 \sin^2 \omega_m t & (7.5)\\ &= \mathcal{E}_{\rm dc}^2 + \frac{1}{2}\mathcal{E}_{ac}^2 + 2\mathcal{E}_{\rm dc}\mathcal{E}_{\rm ac} \sin \omega_m t - \frac{1}{2}\mathcal{E}_{\rm ac}^2 \cos 2\omega_m t \ . & (7.6) \end{aligned}$$

Under application of this electric field, the state vector is

$$|\psi(t)\rangle = \exp\left(-\frac{\rm i}{\hbar}\int^t E(t')\,{\rm d}t'\right)|\psi(t=0)\rangle \ . \tag{7.7}$$

For the moment, the exponential concerning the energy is evaluated.

$$\begin{aligned} \int^t E(t'){\rm d}t' &= \left(E^0 - \frac{\alpha}{2}\mathcal{E}_{\rm dc}^2 - \frac{\alpha}{4}\mathcal{E}_{\rm ac}^2\right)t + \frac{\alpha\mathcal{E}_{\rm dc}\mathcal{E}_{\rm dc}}{\omega_m}\cos\omega_m t \\ &\quad + \frac{\alpha\mathcal{E}_{\rm ac}^2}{8\omega_m}\sin 2\omega_m t \ , & (7.8)\\ &= \left(E^0 - \frac{\alpha}{2}\mathcal{E}_{\rm dc}^2 - \frac{\alpha}{4}\mathcal{E}_{\rm ac}^2\right)t + s_1\cos\omega_m t + s_2 \sin 2\omega_m t \ . & (7.9) \end{aligned}$$

Therefore the state vector can be written in terms of the frequency dependent part and purely electric field dependent part:

$$|\psi(t)\rangle = \exp\left(-\frac{\rm i}{\hbar}(\mathcal{A}+\mathcal{B})\right)|\psi(t=0)]\rangle \ , \tag{7.10}$$

where

$$\begin{aligned} \mathcal{A} &= \left(E^0 - \frac{\alpha}{2}\mathcal{E}_{\rm dc}^2 - \frac{\alpha}{4}\mathcal{E}_{\rm ac}^2\right)t & (7.11)\\ \mathcal{B} &= s_1\cos\omega_m t + s_2\sin 2\omega_m t \ . & (7.12) \end{aligned}$$

The $\mathcal{A}$ term gives the quasi-energy, a dc-like shifting of the Rydberg state, dependent on the dc field and amplitude of the ac field. However $\mathcal{B}$ shows that

something more interesting is going on. There are two sets of sidebands; the first, at frequency ω_m, is dependent on the product of the dc and ac fields,

$$s_1 = \frac{\alpha \mathcal{E}_{\rm ac}\mathcal{E}_{\rm dc}}{\omega_m} , \tag{7.13}$$

$$s_2 = \frac{\alpha \mathcal{E}_{\rm ac}^2}{8\omega_m} . \tag{7.14}$$

The second sidebands are at twice the modulation frequency, ω_m, and are dependent on the magnitude of the ac field, but not the dc field. Addressing this modulation frequency dependence, the exponential term,

$$\exp\left(-\frac{\mathrm{i}\mathcal{B}}{\hbar}\right) = \exp\left\{-(\mathrm{i}\kappa_1 \cos\omega_m t + \mathrm{i}\kappa_2 \sin 2\omega_m t)\right\} , \tag{7.15}$$

is dependent on ω_m and $2\omega_m$. The coefficients $\kappa_1 = s_1/\hbar$ and $\kappa_2 = s_2/\hbar$ have been made dimensionless. Using the properties of Bessel functions,

$$\mathrm{e}^{-\mathrm{i}x\cos\omega t} = \sum_{n=-\infty}^{\infty} \mathrm{i}^n J_{-n}(x)\mathrm{e}^{-\mathrm{i}n\omega t} , \tag{7.16}$$

$$\mathrm{e}^{-\mathrm{i}y\sin\omega t} = \sum_{n=-\infty}^{\infty} J_n(y)\mathrm{e}^{-\mathrm{i}n\omega t} , \tag{7.17}$$

Thus it follows that

$$\exp\left(-\frac{\mathrm{i}\mathcal{B}}{\hbar}\right) = \sum_{n=-\infty}^{\infty} \mathrm{i}^n J_{-n}(\kappa_1)\mathrm{e}^{-in\omega_m t} \sum_{k=-\infty}^{\infty} J_k(\kappa_2)\mathrm{e}^{-i2k\omega_m t} , \tag{7.18}$$

$$= \sum_{n=-\infty}^{\infty}\sum_{k=-\infty}^{\infty} \mathrm{i}^n J_{-n}(\kappa_1)J_k(\kappa_2)\mathrm{e}^{-\mathrm{i}(2k+n)\omega_m t} . \tag{7.19}$$

Substituting $p = n + 2k$,

$$\exp\left(-\frac{\mathrm{i}\mathcal{B}}{\hbar}\right) = \sum_{p=-\infty}^{\infty}\sum_{k=-\infty}^{\infty} \mathrm{i}^{p-2k} J_{2k-p}(\kappa_1)J_k(\kappa_2)\mathrm{e}^{-\mathrm{i}p\omega_m t} . \tag{7.20}$$

Thus combining,

$$|\psi(t)\rangle = \exp\left(-\frac{\mathrm{i}\mathcal{A}}{\hbar}\right)\exp\left(-\frac{\mathrm{i}\mathcal{B}}{\hbar}\right)|\psi(t)\rangle , \tag{7.21}$$

$$= \exp\left(-\frac{\mathrm{i}\left(E^0 - \frac{\alpha}{2}\mathcal{E}_{\rm dc}^2 - \frac{\alpha}{4}\mathcal{E}_{\rm ac}^2\right)t}{\hbar}\right) \times \sum_{p=-\infty}^{\infty}\sum_{k=-\infty}^{\infty} \mathrm{i}^{p-2k} J_{2k-p}(\kappa_1)J_k(\kappa_2)\mathrm{e}^{-\mathrm{i}p\omega_m t}|\psi(t=0)\rangle . \tag{7.22}$$

The perturbation to the wavefunction, $|\psi\rangle$, should also be considered: thus, expanding,

$$|\psi\rangle = |\psi^{(0)}\rangle + \mathcal{E}\,|\psi^{(1)}\rangle + \ldots \tag{7.23}$$

In this experiment, the overlap between the $5P_{3/2}$ state and the Rydberg state is of interest. This overlap is non-zero for the first order term and, due to parity, zero for the $\mathcal{E}\,|\psi^{(1)}\rangle$ term.

This means that the probability to excite to the Rydberg state, and the manifold of sidebands, is given by

$$|\mathcal{B}_p|^2 = \left| \sum_{k=-\infty}^{\infty} \mathrm{i}^{p-2k} J_{2k-p}(\kappa_1) J_k(\kappa_2) \right|^2 , \tag{7.24}$$

where p is the sideband order.

There are a few things to note about this result. The first is that in the presence of no dc field, there are only even order sidebands, due to κ_1 being zero. The ac field generates sidebands only at the 2^{nd} harmonic. With the presence of a dc field, these 2^{nd} harmonics due to the ac field remain and are joined by sidebands at the 1^{st} harmonic.

This result can also be understood in terms of rf photons being absorbed; the coupling to the Rydberg state acts via the absorption of rf photons and one laser photon, with the relative coupling strengths being given by equation 7.24. In the case of no dc field, the number of rf photons absorbed must be even.

7.4 Experimental demonstration

The setup shown in figure 7.5 was used to demonstrate this phase modulation of the Rydberg state; it differs from those shown in previous chapters due to using a 'cancellation' cell. After passing through a beam splitter, the probe beam propagates through two Rb vapour cells: one 1.1 cm cell containing the electrodes, and another 7.5 cm cell. The probe beams are then focussed onto two photodiodes set up in parallel. Subject to the same power, the resulting voltages should cancel each other out. The diagram for this circuit is shown in appendix E. The advantages of this technique are two-fold. Firstly there is common mode noise rejection; any increase in intensity of the laser is cancelled out by the differencing

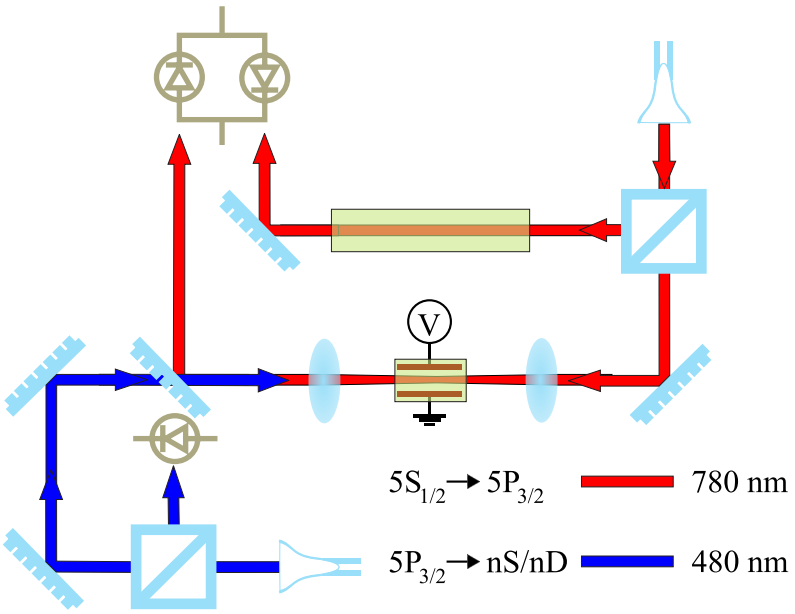

Figure 7.5: Rydberg state phase modulation setup. A 780 nm probe beam is split in two. One beam propagates through an electrode cell, while the other through a 7.5 cm vapour cell. These two beams are then incident on a differencing photodiode. The 480 nm coupling laser passes through the electrode cell in the opposite direction to the probe beam.

performed by the photodiodes. Secondly, with appropriate cell temperatures, it is possible to partly cancel the Doppler background. To this end, the electrode cell is heated to around 40 °C while the other cell is at room temperature.

Counter-propagating through the electrode cell is the coupling beam. The coupling beam is locked to the $5P_{3/2}(F' = 4) \rightarrow 32S_{1/2}$ transition in ^{87}Rb using another cell [55]. The beam sizes and lenses used are the same as in section 7.1. To apply the ac and dc field a Keithley arbitrary function generator is used. To monitor the voltage on the plates, a passive scope probe is used; this has 10 MΩ resistance and a very low capacitance, so that it doesn't change the impedance seen by the function generator.

Four EIT traces are shown in figure 7.6, corresponding to different electric field combinations. In each, the difference in transmission between the two Rb cells is shown as a function of detuning on the $5S_{1/2}(F' = 2) \rightarrow 5P_{3/2}(F' = 3)$ transition in ^{87}Rb. In 7.6(a) no electric field is present in the electrode cell and the usual EIT

feature is recovered. In (b) the only electric field applied is a 7.7 Vcm^{-1} ac field at 26 MHz, thus second order sidebands are seen at twice the modulation frequency. Note that due to the Doppler mismatch, these are seen around $2\omega_m \times 480/780 =$ 32 MHz. In (c) and (d), the effect of the dc field is shown. The generation of first order sidebands is seen. Note the sensitivity of the +1 order sideband to the dc field. As the κ_1 term, which gives rise to the first order sideband, contains an ac and a dc term, a moderate dc field can still produce sizeable sidebands given a large ac field.

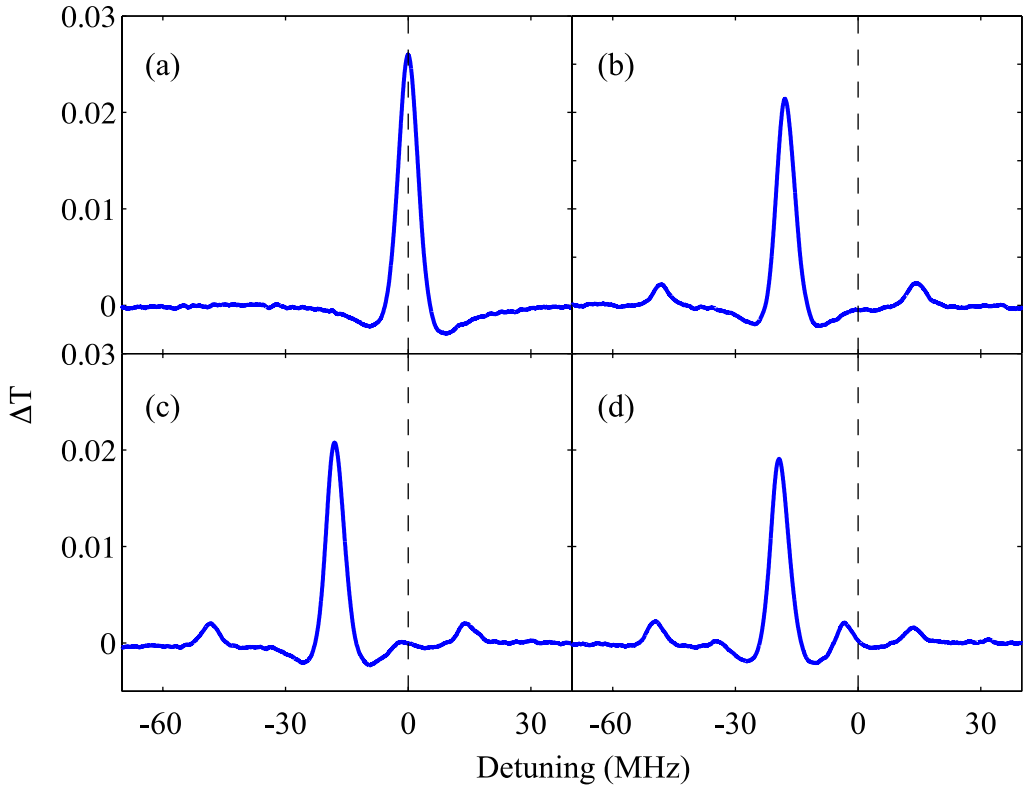

Figure 7.6: Dependence of the Rydberg EIT spectrum on the ac and dc fields. In (a) no electric field is applied, while in (b) an ac field of 7.7 Vcm^{-1} is applied. Added to this is a dc field of 0.4 Vcm^{-1} in (c), while in (d) this is increased to 0.8 Vcm^{-1}.

To study the sensitivity to dc electric fields in more detail, a lock-in amplifier was used to isolate just the effect of the dc field. This is done by programming the waveform seen in figure 7.7 into the arbitrary function generator. The dc voltage is turned on and off at a frequency of 50 kHz, while the ac field is kept constant. This frequency is much less than the modulation, which is greater than 10 MHz.

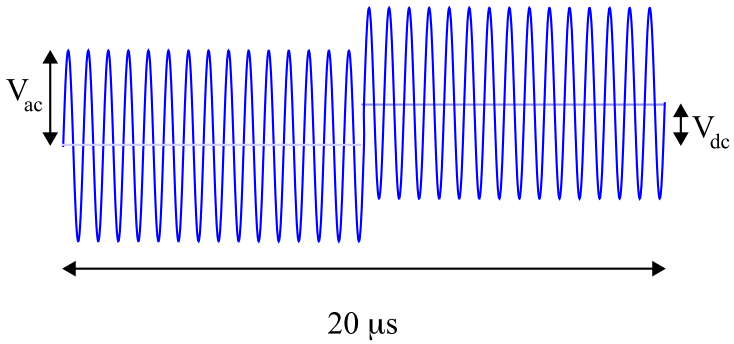

Figure 7.7: Programmed voltage waveform applied to the electrodes. Note that in reality there are many more cycles of the ac field in each half of the waveform.

The resulting spectra can be seen in figure 7.8. In these spectra the dc field is kept constant and the ac field increases. In 7.8(a) there is no ac field and a derivative lineshape is seen. By increasing the ac field, the waveform evolves into a quite complicated shape. The largest change is in the 1^{st} order sideband.

It is interesting to compare the height of these ac dependent signals with the purely dc case. This is shown in figure 7.9. In this case the dc field signal is normalised to one, thus anything greater than this value would be an enhancement. This shows that an ac field can be used to increase the dc electric field sensitivity, by a factor of around 3 for figure 7.9.

Another interesting application of these waveforms may be the determination of unknown dc electric fields. This is addressed in detail in [54], making use of the theoretical fitting work of M. Tanasittikosol. This approach uses equation 7.24 to calculate the altered Rabi frequency to the manifold of states formed in the presence of an ac electric field.

Just using a dispersion signal such as that in figure 7.8(a) to measure dc fields is problematic; laser frequency fluctuations manifest themselves as variations in the signal position on the frequency axis. However this position is the only means with which to calibrate the electric field. By applying an ac electric field, the signal is both larger and more complex, as can be seen in figure 7.8(b)–(d). Crucially the position of the feature on the frequency axis is not the only parameter that can be used to fit the electric field; the shape yields extra information. For these reasons, the use of ac fields reduces the uncertainty in calculating the electric field by an order of magnitude [54].

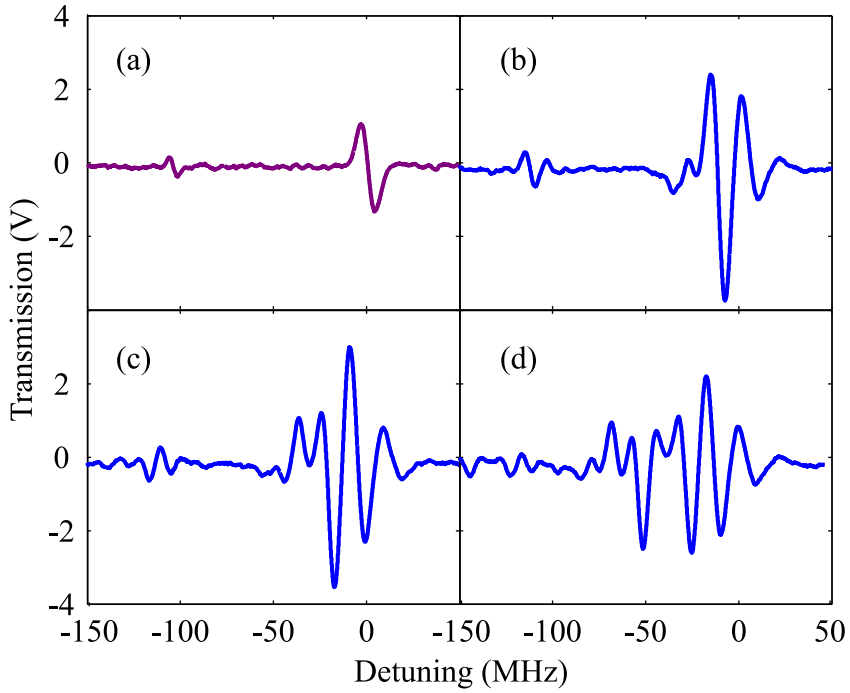

Figure 7.8: Lock-in amplifier signal for various electric field configurations. In (a) the dc electric field is 1.37 Vcm^{-1} and there is no ac field. The same dc field is applied in traces (b)–(d), while ac fields of 5.52, 8.65 and 11.1 Vcm^{-1} respectively are also applied.

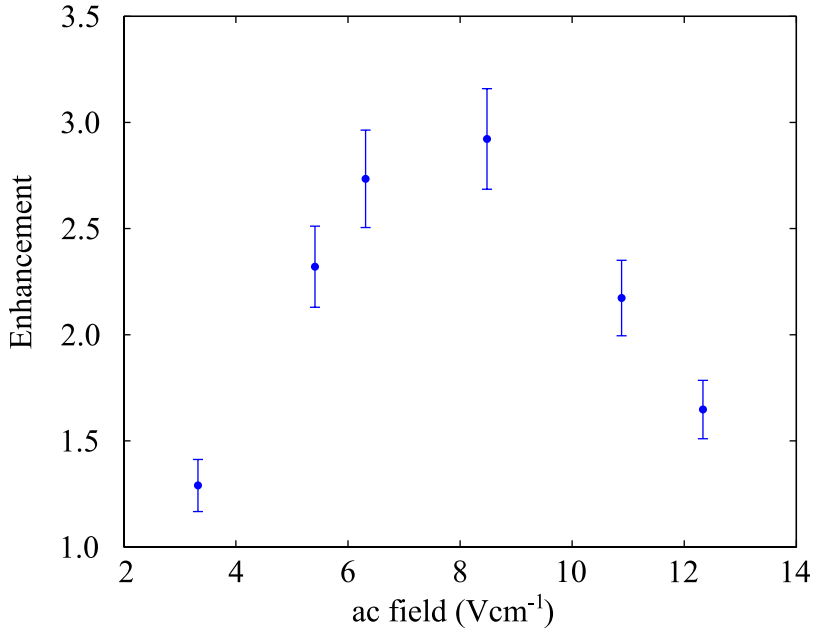

Figure 7.9: Enhancement factor as a function of ac electric field. The dc field is 1.37 Vcm^{-1}. Error bars correspond to the standard deviation of 10 different scans.

7.5 Outlook

This approach depends upon being able to modulate the dc electric field under question. While this may be reasonable in many circumstances, this is not necesarily universal. One could imagine that there could be ways to use lock-in amplification, depending on the application.

The most reliable measure of the quality of an electrometer is the sensitivity, measured in $\mathrm{Vm}^{-1}\mathrm{Hz}^{-1/2}$. This number relates the precision to which an electric field can be measured to the time taken measuring it. However there is a problem in quoting such a number for this experiment; there is still the problem of free charges in the cell. The electric field inside the cell may differ slightly from that resulting from the applied voltage. By moving to the Doppler-free, three-stage excitation scheme in section 5.5, the free charges in the cell should be reduced and the small intersection volume would be in a more uniform electric field.

Chapter 8

Conclusions

The work in this this thesis has looked at the various ways in which EIT can be applied to manipulate the absorption and dispersion of light in multi-level systems. Starting with the relatively simple Λ-system in chapter 2, the concept of EIT was introduced and demonstrated. The production of these narrow EIT features was dependent on the production of Raman laser beams using a double-injection technique.

By adding another laser beam to couple in an extra state to the three level atom, the EIT feature was turned into a narrow absorptive resonance, as discussed in chapter 3. This $\mathcal{N}$-system offers switching from sub-luminal to super-luminal light pulse propagation, as well as the possibility of enhancing weak absorption lines.

Recognising that Rydberg states opened up new possibilities for controlling EIT using electric fields, chapter 4 introduced the concept of Rydberg EIT in the ladder system. The Λ-system and ladder system were then combined to form the Rydberg $\mathcal{N}$-system. It was shown how the switching of narrow absorptive resonances was possible using an external electric field.

Chapter 5 focussed on trying to increase the Rabi frequency available on the coupling transition by focussing into thin vapour cells. Although it was not possible to see Rydberg EIT in the thinnest, micron region of the ultra-thin cell, progress was made in the 700 μm region. Despite this setback it was possible to observe some EIT in the micron region of the cell by coupling to the $5D_{5/2}$ state.

By combining the sensitivity of Rydberg states to electric fields and the highly dispersive nature of EIT the giant-electro optic effect was demonstrated in chap-

ter 6. The phase sensitivity of the Rydberg ladder system to electric fields was used to measure the Kerr coefficient of the thermal ensemble. Furthermore phase modulation of a probe beam was achieved by applying an ac electric field to the vapour, resulting in the production of frequency sidebands on the light.

The possibility of performing electrometry in the vapour cell was addressed in chapter 7. By exploiting the change in transmission associated with EIT, a technique for determining dc electric fields was presented. An enhancement of the transmission signals were then shown to occur by applying an rf electric field.

8.1 Future work

As has been alluded to through the course of thesis, there are a number of ways in which this work might progress. Reflecting the diverse uses of EIT already presented in this work, each 'strand' of investigation could justifiably be studied by itself. However one of the recurring problems throughout these investigations has been the presence of stray charges in the vapour cell.

The development of a Doppler-free three-stage excitation scheme proposed in chapter 5 would thus seem to be a priority. Not only would the production of ions and electrons be curtailed, but the Rydberg EIT resonance width would be narrower. With a narrower resonance, greater phase modulation would be possible and the measurement of electric fields would become more sensitive. Although it would no longer be possible to couple to an $S_{1/2}$ state, due to parity, a $P_{1/2}$ state could be used instead. This way the splitting of m_J components could be avoided.

As the overlap of three laser beams in the Doppler-free configuration would be small, continued research into thin cells would be worthwhile. Although Rydberg EIT has proved to be a useful technique in this thesis, the probing of ground state depletion and subsequent detection using the Faraday effect is an attractive approach for Rydberg studies in thin cells. The basis for such measurements is outlined in chapter 5. By exploiting the high densities made possible by heating thin vapour cells, dipole blockade in the thermal cell could also be demonstrated. The atomic quantum dot that may result would then have applications in single photon generation.

The future for EIT in cold atoms also looks promising. Performing a photonic

phase-gate using cold atoms could also have an impact on quantum information applications. Such an advance would draw on the measurement of the Kerr coefficient detailed in this thesis; the narrow resonances and high densities possible in cold atoms used to increase a large phase shift. The mesoscopic quantum gate outlined in reference [60], combined with the recent advances in observing dipole blockade in atoms suggests that Rydberg EIT may play a large part in the activities of the atomic physics community,

Appendix A

Time evolution of the density matrix

From the definition of the density matrix.

$$\rho = \sum_i p_i \left|\psi_i\right\rangle \left\langle\psi_i\right| \ , \tag{A.1}$$

It follows that,

$$\frac{\partial \rho}{\partial t} = \sum_i p_i \frac{\partial \left|\psi_i\right\rangle}{\partial t} \left\langle\psi_i\right| + \sum_i p_i \left|\psi_i\right\rangle \frac{\partial \left\langle\psi_i\right|}{\partial t} \ . \tag{A.2}$$

Using Schrödinger's equation:

$$\mathrm{i}\hbar \frac{\partial \left|\Psi\right\rangle}{\partial \mathrm{t}} = \mathcal{H}|\Psi\rangle, \tag{A.3}$$

gives:

$$\frac{\partial \left\langle\psi_i\right|}{\partial t} = \left\langle\psi_i\right| \frac{\mathcal{H}}{-\mathrm{i}\hbar} \ . \tag{A.4}$$

Thus using equation A.2

$$\frac{\partial \rho}{\partial t} = \frac{\mathcal{H}}{\mathrm{i}\hbar} \sum_i p_i \left|\psi_i\right\rangle \left\langle\psi_i\right| - \sum_i p_i \left|\psi_i\right\rangle \left\langle\psi_i\right| \frac{\mathcal{H}}{\mathrm{i}\hbar} \ . \tag{A.5}$$

Or more conveniently,

$$\frac{\partial \rho}{\partial t} = \frac{1}{\mathrm{i}\hbar} \left[\mathcal{H}, \rho\right] \ . \tag{A.6}$$

Appendix B

Forming the transformed Hamiltonian

This idea of this section is to reformulate the atom-light Hamiltonian to include the detuning term, Δ_{21}. A laser field with frequency, ω_p acts on a two level atom, whose energy levels separated by $\hbar\omega_1$. The Rabi frequency of this coupling field is Ω_{21} and ρ_{ij} are elements of the density matrix.

$$\mathcal{H} = \begin{pmatrix} \langle 1|\mathcal{H}_{\rm i}|1\rangle & \langle 1|\mathcal{H}_{\rm i}|2\rangle \\ \langle 2|\mathcal{H}_{\rm i}|1\rangle & \langle 2|\mathcal{H}_a|2\rangle \end{pmatrix}. \tag{B.1}$$

$$\mathcal{H} = \begin{pmatrix} 0 & \frac{\hbar\Omega_{21}}{2}\left(e^{-i\omega_p t} + e^{i\omega_p t}\right) \\ \frac{\hbar\Omega_{21}}{2}\left(e^{-i\omega_p t} + e^{i\omega_p t}\right) & \hbar\omega_p \end{pmatrix}. \tag{B.2}$$

$$\dot{\rho}_{11} = -\frac{i}{\hbar}[\mathcal{H}_{11}\rho_{11} - \rho_{11}\mathcal{H}_{11} + \mathcal{H}_{12}\rho_{21} - \rho_{12}\mathcal{H}_{21}] \tag{B.3}$$

$$= -\frac{i\Omega_{21}}{2}\left(e^{-i\omega_p t} + e^{i\omega_p t}\right)(\rho_{21} - \rho_{12}) \tag{B.4}$$

$$\dot{\rho}_{12} = -\frac{i}{\hbar}[\mathcal{H}_{11}\rho_{21} - \rho_{11}\mathcal{H}_{12} + \mathcal{H}_{12}\rho_{11} - \rho_{12}\mathcal{H}_{22}] \tag{B.5}$$

$$= -\frac{i\Omega_{21}}{2}\left(e^{-i\omega_p t} + e^{i\omega_p t}\right)(\rho_{22} - \rho_{11}) + i\omega_p\rho_{12} \tag{B.6}$$

$$\dot{\rho}_{21} = -\frac{\mathrm{i}}{\hbar}[\mathcal{H}_{21}\rho_{11} - \rho_{21}\mathcal{H}_{11} + \mathcal{H}_{22}\rho_{21} - \rho_{22}\mathcal{H}_{21}] \tag{B.7}$$

$$= +\frac{\mathrm{i}\Omega_{21}}{2}\left(\mathrm{e}^{-i\omega_p t} + \mathrm{e}^{\mathrm{i}\omega_p t}\right)(\rho_{22} - \rho_{11}) - \mathrm{i}\omega_p\rho_{12} \tag{B.8}$$

$$\dot{\rho}_{22} = -\frac{\mathrm{i}}{\hbar}[\mathcal{H}_{21}\rho_{21} - \rho_{21}\mathcal{H}_{21} + \mathcal{H}_{22}\rho_{22} - \rho_{22}\mathcal{H}_{22}] \tag{B.9}$$

$$= +\frac{\mathrm{i}\Omega_{21}}{2}\left(\mathrm{e}^{-i\omega_p t} + \mathrm{e}^{i\omega_p t}\right)(\rho_{21} - \rho_{12}) \tag{B.10}$$

Transform:

$$\sigma_{11} = \rho_{11} \tag{B.11}$$

$$\sigma_{12} = \rho_{12}\mathrm{e}^{-\mathrm{i}\omega_p t} \Rightarrow \rho_{12} = \sigma_{12}\mathrm{e}^{\mathrm{i}\omega_p t} \tag{B.12}$$

$$\sigma_{21} = \rho_{21}\mathrm{e}^{\mathrm{i}\omega_p t} \Rightarrow \rho_{21} = \sigma_{21}\mathrm{e}^{-\mathrm{i}\omega_p t} \tag{B.13}$$

$$\sigma_{22} = \rho_{22} \tag{B.14}$$

Thus.

$$\dot{\sigma}_{11} = -\frac{\mathrm{i}\Omega_{21}}{2}\left(\mathrm{e}^{-\mathrm{i}\omega_p t} + \mathrm{e}^{\mathrm{i}\omega_p t}\right)\left(\sigma_{21}\mathrm{e}^{-\mathrm{i}\omega_p t} - \sigma_{12}\mathrm{e}^{\mathrm{i}\omega_p t}\right) \tag{B.15}$$

$$= -\frac{\mathrm{i}\Omega_{21}}{2}\left(\sigma_{21}\mathrm{e}^{-2\mathrm{i}\omega_p t} + \sigma_{21} - \sigma_{12} + \sigma_{12}\mathrm{e}^{2\mathrm{i}\omega_p t}\right) \tag{B.16}$$

$$= -\frac{\mathrm{i}\Omega_{21}}{2}(\sigma_{21} - \sigma_{12}) \tag{B.17}$$

$$\dot{\sigma}_{12}\mathrm{e}^{i\omega_p t} + \mathrm{i}\omega_p\sigma_{12}\mathrm{e}^{\mathrm{i}\omega_p t} = -\frac{\mathrm{i}\Omega_{21}}{2}\left(\mathrm{e}^{-\mathrm{i}\omega_p t} + \mathrm{e}^{\mathrm{i}\omega_p t}\right)(\sigma_{22} - \sigma_{11}) + \mathrm{i}\omega_p\sigma_{12}\mathrm{e}^{\mathrm{i}\omega_p t} \tag{B.18}$$

$$\dot{\sigma}_{12} = -\frac{\mathrm{i}\Omega_{21}}{2}(\sigma_{22} - \sigma_{11}) - \mathrm{i}\Delta_{21}\sigma_{12} \tag{B.19}$$

$$\dot{\sigma}_{21}\mathrm{e}^{i\omega_p t} - \mathrm{i}\omega_p\sigma_{21}\mathrm{e}^{\mathrm{i}\omega_p t} = \frac{\mathrm{i}\Omega_{21}}{2}\left(\mathrm{e}^{-\mathrm{i}\omega_p t} + \mathrm{e}^{\mathrm{i}\omega_p t}\right)(\sigma_{22} - \sigma_{11}) + \mathrm{i}\omega_p\sigma_{21}\mathrm{e}^{-\mathrm{i}\omega_p t} \tag{B.20}$$

$$\dot{\sigma}_{21} = \frac{\mathrm{i}\Omega_{21}}{2}(\sigma_{22} - \sigma_{11}) + \mathrm{i}\Delta_{21}\sigma_{21} \tag{B.21}$$

$$\dot{\sigma}_{22} = \frac{\mathrm{i}\Omega_{21}}{2}(\sigma_{21} - \sigma_{12}) \tag{B.22}$$

$$\mathcal{H} = \begin{pmatrix} \mathcal{H}_{11} & \mathcal{H}_{12} \\ \mathcal{H}_{21} & \mathcal{H}_{22} \end{pmatrix}. \tag{B.23}$$

$$\mathcal{H} = \begin{pmatrix} \sigma_{11} & \sigma_{12} \\ \sigma_{21} & \sigma_{22} \end{pmatrix}. \tag{B.24}$$

$$\mathcal{H}\sigma = \begin{pmatrix} \mathcal{H}_{11}\sigma_{11} + \mathcal{H}_{12}\sigma_{21} & \mathcal{H}_{11}\sigma_{12} + \mathcal{H}_{12}\sigma_{22} \\ \mathcal{H}_{21}\sigma_{11} + \mathcal{H}_{22}\sigma_{21} & \mathcal{H}_{21}\sigma_{12} + \mathcal{H}_{22}\sigma_{22} \end{pmatrix}. \tag{B.25}$$

$$\sigma\mathcal{H} = \begin{pmatrix} \sigma_{11}\mathcal{H}_{11} + \sigma_{21}\mathcal{H}_{12} & \sigma_{12}\mathcal{H}_{11} + \sigma_{22}\mathcal{H}_{12} \\ \sigma_{11}\mathcal{H}_{21} + \sigma_{21}\mathcal{H}_{22} & \sigma_{12}\mathcal{H}_{21} + \sigma_{22}\mathcal{H}_{22} \end{pmatrix}. \tag{B.26}$$

$$\dot{\sigma} = -\frac{i}{\hbar}\begin{pmatrix} \mathcal{H}_{12}\sigma_{21} - \mathcal{H}_{21}\sigma_{12} & \mathcal{H}_{12}(\sigma_{22} - \sigma 11) - (\mathcal{H}_{22} - \mathcal{H}_{11})\sigma_{12} \\ -\mathcal{H}_{21}(\sigma_{22} - \sigma 11) + (\mathcal{H}_{22} - \mathcal{H}_{11})\sigma_{21} & \mathcal{H}_{21}\sigma_{12} - \mathcal{H}_{12}\sigma_{21} \end{pmatrix}. \tag{B.27}$$

Compare to:

$$\dot{\sigma} = -\frac{i}{\hbar}\begin{pmatrix} \frac{\hbar\Omega_{21}}{2}(\sigma_{21} - \sigma_{12}) & \frac{\hbar\Omega_{21}}{2}(\sigma_{22} - \sigma_{11}) + \hbar\Delta_{21}\sigma_{12} \\ -\frac{\hbar\Omega_{21}}{2}(\sigma_{22} - \sigma_{11}) - \hbar\Delta_{21}\sigma_{12} & -\frac{\hbar\Omega_{21}}{2}(\sigma_{21} - \sigma_{12}) \end{pmatrix}. \tag{B.28}$$

Now we analyse the elements of each expression. (1,1)

$$\mathcal{H}_{12} = \tfrac{\hbar\Omega_{21}}{2} \quad \mathcal{H}_{12} = \tfrac{\hbar\Omega_{21}}{2} \tag{B.29}$$

(1,2)

$$\mathcal{H}_{12} = \tfrac{\hbar\Omega_{21}}{2} \quad -(\mathcal{H}_{22} - \mathcal{H}_{11}) = \hbar\Delta_{21} \tag{B.30}$$

(2,1)

$$\mathcal{H}_{21} = \tfrac{\hbar\Omega_{21}}{2} \quad (\mathcal{H}_{22} - \mathcal{H}_{11}) = -\hbar\Delta_{21} \tag{B.31}$$

(2,2)

$$\mathcal{H}_{12} = \tfrac{\hbar\Omega_{21}}{2} \quad \mathcal{H}_{12} = \tfrac{\hbar\Omega_{21}}{2} \tag{B.32}$$

But $\mathcal{H}_{11} = 0$ and so we have,

$$\mathcal{H} = \hbar \begin{pmatrix} 0 & \frac{\Omega_{21}}{2} \\ \frac{\Omega_{21}}{2} & -\Delta_{21} \end{pmatrix}. \tag{B.33}$$

Appendix C

Phase Modulation

Considering a medium of length L where the refractive index is time dependent, $n_r(t)$, the propagation of a light beam with wavelength λ results in a phase ϕ

$$\phi(t) = \frac{2\pi L}{\lambda} n_r(t) \,, \tag{C.1}$$

The electric field, $\mathcal{E}(t)$, emerging from the medium includes this phase modulation

$$\mathcal{E}(t) = \mathcal{E}_0 \cos(\omega t + \phi(t)) \quad , \tag{C.2}$$

If the refractive index is modulated at a frequency ω_m

$$n_r(t) = n_{r0}(\sin \omega_m t) \,, \tag{C.3}$$

where n_{r0} is the unshifted refractive index, the electric field now becomes

$$\mathcal{E}(t) = \mathcal{E}_0[\cos \omega t \cos (m \sin \omega_m t) - \sin \omega t (m \sin \omega_m t)] \,, \tag{C.4}$$

where

$$m = \frac{2\pi L}{\lambda} n_{r0} \tag{C.5}$$

is referred to as the depth of modulation. Exploiting the properties of Bessel functions we can then write equation (C.4) as [140],

$$\begin{aligned} \mathcal{E}(t) \quad = \quad & \mathcal{E}_0[J_0(m) \cos \omega t + J_1(m) \cos(\omega + \omega_m) \\ & -J_1(m) \cos(\omega - \omega_m)t + J_2(m) \cos(\omega + 2\omega_m)t \\ & +J_2(m) \cos(\omega - 2\omega_m)t + J_3(m) \cos(\omega + 3\omega_m)t \\ & -J_3(m) \cos(\omega - 3\omega_m t) + ...] \quad . \end{aligned} \tag{C.6}$$

Where the following identities have been used:

$$\cos(m \sin \omega_m t) = J_0(m) + 2 \sum_{k=1}^{\infty} J_{2k}(m) \cos(2k\omega_m t) \tag{C.7}$$

$$\sin(m \sin \omega_m t) = 2 \sum_{k=0}^{\infty} J_{2k+1}(m) \sin((2k+1)\omega_m t) \tag{C.8}$$

$$2 \sin A \sin B = \cos(A - B) - \cos(A + B) \tag{C.9}$$

$$2 \cos A \cos B = \cos(A - B) + \cos(A + B) \tag{C.10}$$

Thus there are frequency components equally spaced and separated by ω_m.

Appendix D

List of symbols

Parameter	symbol	Parameter	symbol
Total detuning	δ	Detuning	Δ_{ij}
Magnetic field	B	Velocity	υ
Mass	m	Electric field	$\mathcal{E}$
Electron charge	e	Hamiltonian	$\mathcal{H}$
Rydberg constant	R	Permittivity of free space	ϵ_0
Bohr radius	a_0	Energy	E
Orbital angular momentum	ℓ	Speed of light	c
Electric potential	V	Susceptibility	χ
Dipole matrix element	d_{ik}	Total atomic angular momentum	F
Probe wave vector	k_p	Planck's constant/2π	$\hbar$
Principal quantum number	n	Wavelength	λ
Refractive index	n_r	Magnetic quantum number	m_F
Rabi frequency	Ω_{ij}	Wavefunction	ψ

Appendix E

Differencing circuit

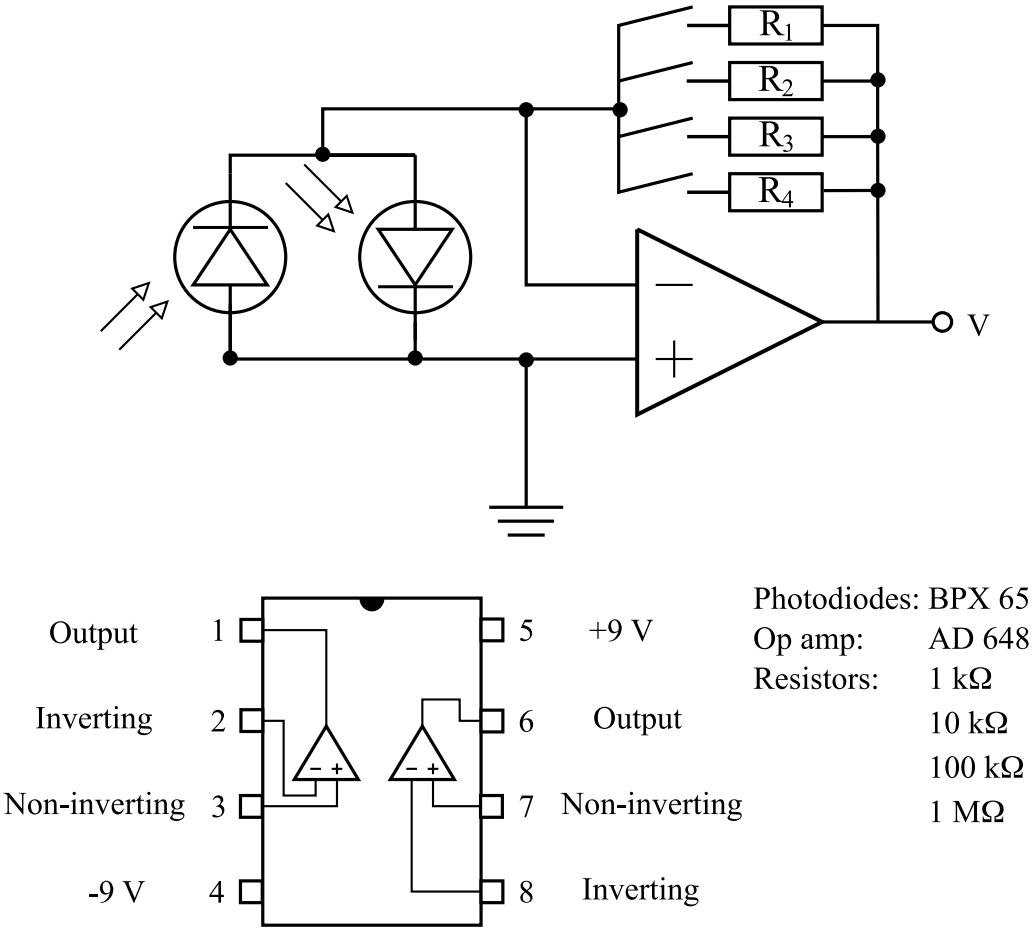

Figure E.1: Circuit diagram used for building a differencing photodiode.

Appendix F

Operation of the multi-region cell

The multi-region cell has been made to high precision and needs to be treated with care to avoid damage. To prolong its life a number of precautions must be followed:

1. To prevent condensation of Rubidum vapour on the windows, it is necessary to maintain a temperature gradient across the cell. To this end, the window temperature must be kept 30 °C higher than the side-arm. This equates to a thermocouple reading of greater than 2 mV.

2. The temperature limit of the windows is 430 °C and of the side arm 380 °C. This temperature limit on the side-arm is set by the reaction of glass and Rubidium.

3. To measure both temperature two thermocouples are used. When aligning the cell at room temperature, these thermocouples should be placed just above the window of the region under investigation and at the same height as the Rubidum column a few millimetres away from touching.

4. When the cell has been heated up, avoid causing abrupt temperature changes. This means letting the whole assembly, including the oven cool down to room temperature before any repositioning is carried out. Also do not touch the hot cell with a cold thermocouple. It is safer to perform the alignment of at room temperature and then heat the cell up.

5. Usually in the 2 mm and 700 μm regions, it is not necessary to turn on both heaters to achieve good optical thickness.

F.1 Alignment

When aligning the beams into one region of the cell, care must be taken not to look directly into the beam. Instead an infra red viewer card should be used. If the cell is aligned perpendicular to the beam propagation direction, it is possible that the probe beam may be reflected back on itself by the cell window. This can results in the observation of Doppler-free resonances, which may or may not be desirable.

F.2 Turning on

For the 700 μm region, it is safe to turn the current to the window heater on at 1.2→1.4 A. If the micron cell is going to be used, turn on at around this current, then wait around 10 minutes to allow the window to heat up before turning on the side-arm heater. Note that even in this cell, it is often sufficient to run just the window heater at a high enough current.

Typical operational currents are 0.8→1.1 A for the 2 mm cell, 1.2→1.4 A for the 700 μm region and 2 A for the 2→6 μm region.

F.3 Turning off

As a rough guide when the thermocouple by the window reads 4.0 mV (118 °C) and the sidearm thermocouple reads around 1.9 mV (67 °C) it is safe to turn the heater off. If not then turn the current down in two steps.

Bibliography

[1] Arimondo, E. *Coherent population trapping in laser spectroscopy*, volume 35 of *Progress in Optics*. Elsevier Science Publ. B V, Amsterdam, (1996).

[2] Aspect, A., Arimondo, E., Kaiser, R., Vansteenkiste, N. & Cohen-Tannoudji, C. *Phys. Rev. Lett.* **61**, 826 (1988).

[3] Wynands, R. & Nagel, A. *Appl. Phys. B* **68**, 1 (1999).

[4] Kuklinski, J. R., Gaubatz, U., Hioe, F. T. & Bergmann, K. *Phys. Rev. A* **40**, 6741 (1989).

[5] Gaubatz, U., Rudecki, P., Schiemann, S. & Bergmann, K. *J. Chem. Phys* **92**, 5363 (1990).

[6] Danzl, J. G. *et al. Science* , 1062 (2008).

[7] Harris, S. E. *Phys. Rev. Lett.* **62**, 1033 (1989).

[8] Scully, M. O. & Fleischhauer, M. *Science* **263**, 337 (1994).

[9] Akulshin, A. M., Barreiro, S. & Lezama, A. *Phys. Rev. A* **57**, 2996 (1998).

[10] Lezama, A., Barreiro, S. & Akulshin, A. M. *Phys. Rev. A* **59**, 4732 (1999).

[11] Akulshin, A. M., Cimmino, A., Sidorov, A. I., Hannaford, P. & Opat, G. I. *Phys. Rev. A* **67**, 011801 (2003).

[12] Kim, K., Moon, H. S., Lee, C., Kim, S. K. & Kim, J. B. *Phys. Rev. A* **68**, 013810 (2003).

[13] Petroni, N. C. & Vigier, J. P. *Found. Phys. Lett.* **14**, 395 (2001).

[14] Hau, L. V., Harris, S. E., Dutton, Z. & Behroozi, C. H. *Nature* **397**, 594 (1999).

[15] Alam, S. *Lasers without Inversion and Electromagnetically Induced Transparency*. SPIE Publications, (1999).

[16] Fulton, D. J., Shepherd, S., Moseley, R. R., Sinclair, B. D. & Dunn, M. H. *Phys. Rev. A* **52**, 2302 (1995).

[17] Slusher, R. E. & Gibbs, H. M. *Phys. Rev. A* **5**, 1634 (1972).

[18] Tanaka, H. *et al. Phys. Rev. A* **68**, 053801 (2003).

[19] Budker, D., Kimball, D. F., Rochester, S. M. & Yashchuk, V. V. *Phys. Rev. Lett.* **83**, 1767 (1999).

[20] Lie, C., Dutton, Z., Behroozi, C. H. & Hau, L. V. *Nature* **409**, 490 (2000).

[21] Phillips, D. F., Fleischhauer, A., Mair, A. & Walsworth, R. L. *Phys. Rev. Lett.* **86**, 783 (2001).

[22] Schnorrberger, U. *et al.* arXiv:0903.0135, (2009).

[23] Zimmer, G. & Fleischhauer, M. *Phys. Rev. Lett.* **92**, 253201 (2004).

[24] Scully, M. O. & Fleischhauer, M. *Phys. Rev. Lett.* **69**, 1360 (1992).

[25] Gallgher, T. F. *Rydberg Atoms*. Cambridge University Press, Cambridge, (1994).

[26] Harvey, K. C. & Stoicheff, B. P. *Phys. Rev. Lett.* **38**, 537 (1977).

[27] Raimond, J. M., Vitrant, G. & Haroche, S. *J. Phys. B* **14**, L655 (1981).

[28] Heidemann, R. *et al. Phys. Rev. Lett.* **99**, 163601 (2007).

[29] Singer, K., Reetz-Lamour, M., Amthor, T., Marcassa, L. G. & Weidemüller, M. *Phys. Rev. Lett.* **93**, 163001 (2004).

[30] Tong, D. *et al. Phys. Rev. Lett.* **93**, 063001 (2004).

[31] Liebisch, T. C., Reinhard, A., Berman, P. R. & Raithel, G. *Phys. Rev. Lett.* **95**, 253002 (2005).

[32] Vogt, T. *et al. Phys. Rev. Lett.* **97**, 083003 (2006).

[33] Tuaschinsky, A., van Ditzhuijzen, C. S. E., Noordam, L. D. & van Linden van den Heuvell, H. B. *Phys. Rev. A* **78**, 063409 (2008).

[34] Jaksch, D. *et al. Phys. Rev. Lett.* **85**, 2208 (2000).

[35] Bloch, I. *Nature* **453**, 1016 (2008).

[36] Lukin, M. D. *et al. Phys. Rev. Lett.* **87**, 037901 (2001).

[37] Nelson, K. D., Li, X. & Weiss, D. S. *Nat Physics* **3**, 556 (2007).

[38] DiVincenzo, D. P. *Fortschr. Phys,* **48**, 771 (2000).

[39] Urban, E. *et al. Nat Physics* **5**, 110 (2009).

[40] Gaetan, A. *et al. Nat Physics* **5**, 115 (2009).

[41] Weber, B. *et al. Physical Review Letters* **102**, 030501 (2009).

[42] Fleischhauer, M., Imamoğlu, A. & Marangos, J. P. *Rev. Mod. Phys.* **77**, 633 (2005).

[43] Schmidt, H. & Imamoğlu, A. *Opt. Lett.* **21**, 1936 (1996).

[44] Shapiro, J. H. *Phys. Rev. A* **73**, 062305 (2006).

[45] Friedler, I., Petrosyan, D., Fleischhauer, M. & Kurizki, G. *Phys. Rev. A* **72**, 043803 (2005).

[46] Fleischhauer, M. & Lukin, M. D. *Phys. Rev. Lett.* **84**, 5094 (2000).

[47] Fleischhauer, M. & Lukin, M. D. *Phys. Rev. A* **65**, 022314 (2002).

[48] Clarke, J., Chen, H. & van Wijngaarde, William, A. *Appl. Opt.* **40**, 2047 (2001).

[49] Löw, R. *et al.* arXiv:0706.2639, (2007).

[50] Mohapatra, A. K., Jackson, T. R. & Adams, C. S. *Phys. Rev. Lett.* **72**, 113003 (2007).

[51] Mauger, S., Millen, J. & Jones, M. P. A. *J. Phys. B* **40**, F319 (2007).

[52] Mohapatra, A. K., Bason, M. G., Butscher, B., Weatherill, K. J. & Adams, C. S. *Nat Physics* **4**, 890 (2008).

[53] Bason, M. G., Mohapatra, A. K., Weatherill, K. J. & Adams, C. S. *Phys. Rev. A* **77**, 032305 (2008).

[54] Bason, M. G. *et al.* arXiv:0906.4367v1, (2009).

[55] Abel, R. P. *et al. Appl. Phys. Lett.* **94**, 071107 (2009).

[56] Weatherill, K. J. *et al. J. Phys. B* **41**, 201002 (2008).

[57] Raitzsch, U. *et al. New J. Phys.* **11**, 055014 (2009).

[58] Thoumany, P., Hänsch, T., Stania, G., Urbonas, L. & Becker, T. *Opt. Lett.* **34**, 1621 (2009).

[59] Thoumany, P. *et al. J. Mod. Opt.* , preprint (2009).

[60] Müller, M., Lesanovsky, I., Weimer, H., Büchler, H. P. & Zoller, P. *Phys. Rev. Lett.* **102**, 170502 (2009).

[61] Boyd, R. W. *Non-Linear Optics*. Academic Press, (2003).

[62] Boller, K.-J., Imamoğlu, A. & Harris, S. E. *Phys. Rev. Lett.* **66**, 2593 (1991).

[63] Bloch, F. *Phys. Rev.* **70**, 460 (1946).

[64] Gea-Banacloche, J., Li, Y., Jin, S. & Xiao, M. *Phys. Rev. A* **51**, 576 (1995).

[65] Bernath, P. F. *Spectra of atoms and molecules*. Oxford University Press, (2005).

[66] Kasevich, M. & Chu, S. *Phys. Rev. Lett.* **67**, 181 (1991).

[67] Steck, D. *Rb 87 D Line Data*. http://steck.us/alkalidata.

[68] Bouyer, P., Gustavson, T. L., Haritos, K. G. & Kasevich, M. A. *Opt. Lett.* **21**, 1502 (1996).

[69] Jones, M. *et al.* in *Proceedings of the 17th Conference on Laser Spectroscopy*, 413 (World Scientific, Singapore, 2005).

[70] Dotsenko, I. *et al. Appl. Phys. B* **78**, 711 (2004).

[71] Bason, M. G., Mohapatra, A. K., Weatherill, K. J. & Adams, C. S. *J. Phys. B* **42**, 075503 (2009).

[72] Pearman, C. P. *et al. J. Phys. B* **35**, 5141 (2002).

[73] Szymaniec, K., Ghezali, S., Cognet, L. & Clairon, A. *Opt. Comm.* **144**, 50 (1997).

[74] Clarke, R. B. M. *et al. Opt. Comm.* **158**, 36 (1998).

[75] Agarwal, G. S., Dey, T. N. & Menon, S. *Phys. Rev. A.* **64**, 053809 (2001).

[76] Sun, H. *et al. Phys. Lett. A* **335**, 68 (2005).

[77] Niu, Y., Gong, S., Li, R., Xu, Z. & Liang, X. *Opt. Lett.* **30**, 3371 (2005).

[78] Yelin, S. F., Sautenkov, V. A., Kash, M. M., Welch, G. R. & Lukin, M. D. *Phys. Rev. A.* **68**, 063801 (2003).

[79] Ye, C. Y. & Zibrov, A. S. *Phys. Rev. A* **65**, 023806 (2002).

[80] Goren, C., Wilson-Gordon, A. D., Rosenbluh, M. & Friedmann, H. *Phys. Rev. A.* **69**, 053818 (2004).

[81] Kong, L. B., Tu, X. H., Wang, J., Zhu, Y. & Zhan, M. S. *Opt. Comm.* **269**, 362 (2007).

[82] Ye, C. Y., Zibrov, A. S., Rostovtsev, Y. V. & Scully, M. O. *Phys. Rev. A* **65**, 043805 (2002).

[83] Cohen-Tannoudji, C. *Atom-Photon Interactions*. Wiley Science, (1998).

[84] Tanasittikosol, M. private communication.

[85] Rostovtsev, Y., Protsenko, I., Lee, H. & Javan, A. *J. Mod. Opt.* **49**, 2501 (2002).

[86] Pack, M. V., Camacho, R. M. & Howell, J. C. *Phys. Rev. A.* **76**, 013801 (2007).

[87] Iftiquar, S. M., Karve, G. R. & Natarajan, V. *Phys. Rev. A.* **77**, 063807 (2008).

[88] Wei, X.-G. *et al. EPL* **78**, 4402 (2007).

[89] Yang, L. *et al. Phys. Rev. A.* **72**, 053801 (2005).

[90] Kash, M. M. *et al. Phys. Rev. Lett.* **82**, 5229 (1999).

[91] Li, W., Mourachko, I., Noel, M. W. & Gallagher, T. F. *Phys. Rev. A* **67**, 052502 (2003).

[92] Han, J., Jamil, Y., Norum, D. V. L., Tanner, P. J. & Gallagher, T. F. *Phys. Rev. A.* **74**, 054502 (2006).

[93] Sansonetti, J. E. *J. Phys. Chem. Ref. Data* **35**, 301 (2006).

[94] Krishna, A., Pandey, K., Wasan, A. & Natarajan, V. *EPL* **72**, 221 (2005).

[95] Gounand, F. *J. Phys. (Paris)* **40**, 457 (1979).

[96] Ashoori, R. C. *Nature* **379**, 413 (1996).

[97] Sargsyan, A., Sarkisyan, D. & Papoyan, A. *Phys. Rev. A* **73**, 033803 (2006).

[98] Fichet, M. *et al. EPL* **77**, 54001 (2007).

[99] Varzhapetyan, T. *et al. J. Phys. B* **41**, 185004 (2008).

[100] Jackson, J. D. *Classical Electrodynamics*. Wiley, (1998).

[101] Amthor, T. *Interaction-induced dynamics in ultracold Rydberg gases - Mechanical effects and coherent processes*. PhD thesis, University of Freiburg, (2008).

[102] Raitzsch, U. *Universal scaling and coherence properties of an ultracold Rydberg gas*. PhD thesis, University of Stuttgart, Munich, (2008).

[103] Afrousheh, K. *et al. Phys. Rev. Lett.* **93**, 233001 (2004).

[104] van Ditzhuijzen, C. S. E. *et al. Phys. Rev. Lett.* **100** (2008).

[105] Heidemann, R. *et al. Phys. Rev. Lett.* **100** (2008).

[106] Sarkisyan, D., Bloch, D., Papoyan, A. & Ducloy, M. *Opt. Comm.* **200**, 201 (2001).

[107] Sarkisyan, D., Sarkisyan, A. & Yalanusyan, A. *Appl. Phys. B* **66**, 241 (1998).

[108] Sarkisyan, D. & Melkonyan, A. *Prib. Eksp.* **2**, 202 (1989).

[109] Kiejna, A. & Wojciechowski, K. F. *Metal surface electron physics*. Pergamon, (1996).

[110] Kübler, H., Shaffer, J. P., Baluktsian, T., Löw, R. & Pfau, T. arxiv:0908.0275v1, (2009).

[111] Spitzer, W. G. & Kleinman, D. A. *Phys. Rev.* **121**, 1324 (1961).

[112] Grive, T. T., Sanchez-Villicana, V., Duncan, B. C., Maleki, S. & Gould, P. L. *Phys. Scr.* **52**, 271 (1995).

[113] Badger, S. D., Hughes, I. G. & Adams, C. S. *J. Phys. B* **34**, L749 (2001).

[114] Olson, A. J., Carlson, E. J. & Mayer, S. K. *Am. J. Phys.* **74**, 218 (2006).

[115] Hamid, R., Centina, M. & Celik, M. *Opt. Comm.* **224**, 247 (2003).

[116] Xiao, M., Li, Y.-Q., Jin, S.-Z. & Gea-Banacloche, J. *Phys. Rev. Lett.* **74**, 666 (1995).

[117] Moseley, R. R., Shepherd, S., Fulton, D. J., Sinclair, B. D. & Dunn, M. H. *Opt. Comm.* **119**, 61 (1995).

[118] Weatherill, K. J. *A CO_2 Laser Lattice Experiment for Cold Atoms*. PhD thesis, University of Durham, (2007).

[119] Sanguinetti, B., Majeed, H. O., Jones, M. L. & Vacoe, B. T. H. arXiv:0905.0571v1, (2009).

[120] Budker, D. *et al. Rev. Mod. Phys.* **74**, 1153 (2002).

[121] Siddons, P., Bell, N. C., Cai, Y., Adams, C. S. & Hughes, I. G. *Nat Photon* **3**, 225 (2009).

[122] Löw, R. & Pfau, T. *Nat Photon* **3**, 197 (2009).

[123] Kerr, J. *Phil. Mag.* **50**, 337 (1875).

[124] Spence, D. E., Kean, P. N. & Sibbett, W. *Opt. Lett.* **16**, 42 (1991).

[125] Harris, S. E., Field, J. E. & Imamoğlu, A. *Phys. Rev. Lett.* **64**, 1107 (1990).

[126] Kang, H. & Zhu, Y. *Phys. Rev. Lett.* **91**, 093601 (2003).

[127] Chuang, I. L. & Yamamoto, Y. *Phys. Rev. A* **52**, 3489 (1995).

[128] Inbar, E. & Arie, A. *Appl. Phys. B* **70**, 849 (2000).

[129] Webber, M. J. *Handbook of Optical Materials*. CRC Press, (2003).

[130] Chen, Y. F., Liu, Y. C., Tsai, Z. H., Wang, S. H. & Yu, I. A. *Phys. Rev. A* **72** (2005).

[131] Li, Y. & Xiao, M. *Opt. Lett.* **20**, 1489 (1995).

[132] Chen, H. X., Durrant, A. V., Marangos, J. P. & Vaccaro, J. A. *Phys. Rev. A* **58**, 1545 (1998).

[133] Pashkin, Y. A., Nakamura, Y. & Tsai, J. S. *Appl. Phys. Lett.* **76**, 2256 (2000).

[134] Knobel, R. G. & Cleland, A. N. *Nature* **424**, 291 (2003).

[135] Bayfield, J. E., Gardner, L. D., Gulkok, Y. Z. & Sharma, S. D. *Phys. Rev. A* **24**, 138 (1981).

[136] Zhang, Y., Ciocca, M., Burkhardt, C. E. & Leventhal, J. J. *Phys. Rev. A* **50**, 1101 (1994).

[137] O'Sullivan, M. S. & Stoicheff, B. P. *Phys. Rev. A* **31**, 2718 (1985).

[138] Chu, S., Bjorkholm, J. E., Ashkin, A. & Cable, A. *Phys. Rev. Lett.* **57**, 314 (1986).

[139] Budker, D., Kimball, D. F. & DeMille, D. D. *Atomic physics: An exploration through problems and solutions*. Oxford University Press, (2004).

[140] Davis, C. C. *Lasers and Electro-optics: Fundamentals and Engineering*. Cambridge University Press, (1996).